High-resolution vibrational spectroscopy of cold molecular hydrogen ions

Inaugural-Dissertation

zur Erlangung des Doktorgrades
der Mathematisch-Naturwissenschaftlichen Fakultät
der Heinrich-Heine-Universität Düsseldorf

vorgelegt von

Ulf Bressel

aus Düsseldorf

Düsseldorf, Dezember 2011

Aus dem Institut für Experimentalphysik
der Heinrich-Heine Universität Düsseldorf

Gedruckt mit der Genehmigung der
Mathematisch-Naturwissenschaftlichen Fakultät der
Heinrich-Heine-Universität Düsseldorf

Referent: Prof. S. Schiller, Ph. D.
Korreferent: Prof. Dr. K. Schierbaum

Tag der mündlichen Prüfung: 25.01.2012

High-resolution vibrational spectroscopy of cold molecular hydrogen ions

This work presents various new results and applications in the field of cold trapped molecular ions (10-15 mK). Within the framework of the thesis, research has been concentrated on the molecular hydrogen ion HD^+. This molecular ion, containing only two nuclei and one electron, represents the most simple, stable molecule with an electric dipole-allowed ro-vibronic spectrum, making it an important benchmark system.

The development of a novel, and in its way unique, continuous-wave 5 μm spectrometer laser source, and its application in high-resolution spectroscopy of the ro-vibrational fundamental transitions in the molecular hydrogen ion HD^+, are the focus of this thesis.

In order to address the $(\upsilon = 0, L = 0) \rightarrow (\upsilon' = 1, L' = 1)$ fundamental transition in cold trapped HD^+ ions, a 5.115 μm spectrometer source had to be developed. It is based on difference-frequency generation of two mid-IR laser sources at 1064 nm and 1344 nm, respectively, in a periodically poled lithium niobate crystal (MgO:PPLN). Although strong absorption of the 5 μm radiation occurs in the crystal, a maximum output power of 105 μW could still be achieved. The longest generated wavelength was 5.48 μm, substantially longer than the previous limit of 4.57 μm achieved elsewhere.

The 1344 nm laser source is a home-built quantum dot external cavity diode laser (QD-ECDL) in Littrow configuration with a free-running line width of 5 MHz. It is frequency-stabilized to a GPS-referenced femtosecond Ti:sapphire frequency comb, whereas the 1064 nm laser is stabilized to a Doppler-free resonance in molecular iodine, yielding a narrow linewidth (about 720 kHz) laser wave at 5.1 μm. Being much smaller than the Doppler-width of about 3 MHz of a typical (hyperfine-) transition in cold HD^+, the source is well suitable for high resolution spectroscopy. Both laser frequencies are simultaneously measured with the frequency comb and the difference frequency at 5.1 μm is calculated with a computer.

With the help of an intensity modulator at 1344 nm, the spectrometer is in addition relatively fast frequency-tunable to any desired frequency within a range of 460 MHz around a set centre frequency. This feature enables to precisely change the laser frequency at 5.1 μm with a rate of about 35 MHz/s, representing a crucial ability for the successful demonstration of hyperfine pumping into a goal state.

Tuning the spectrometer to the unperturbed transition frequency of the fundamental transition $(\upsilon = 0, L = 0) \rightarrow (1,1)$, it was possible to demonstrate for the first time, the addressing of single quantum levels (with still magnetic sub-state degeneracy) in a molecular ion. Moreover, even single quantum states (using nondegenerate states) could be addressed.

Furthermore, we resolved, for the first time, the hyperfine structure of two low-lying ro-vibrational states in HD^+. Precise measurements of the level spacings, as well as the absolute frequency of the vibrational transitions were performed. The achieved frequency resolution is, to our knowledge, better than any previous measurement on any molecular ion.

The technique demonstrated here shows that spectroscopy on sympathetically cooled molecular ions can lead to higher resolution than established techniques, e.g. the ion beam method. On the molecular physics side, the main result of this work is the most precise test of *ab initio* theory of any molecule so far.

Hochauflösende Schwingungsspektroskopie kalter Wasserstoff-Molekülionen

In dieser Arbeit werden verschiedene neuartige Ergebnisse und Anwendungen aus dem Gebiet der kalten gefangenen Molekülionen (10-15 mK) vorgestellt. Die Forschung konzentrierte sich dabei auf das Wasserstoff-Molekülion HD^+. Dieses besteht nur aus zwei Kernen und einem Elektron und repräsentiert das einfachste stabile Molekül mit einem elektrisch dipol-erlaubten Rotations-Schwingungsspektrum, welches es zu einem wichtigen Modellsystem macht.

Die Entwicklung einer neuartigen, in ihrer Art einzigartigen, 5 µm Dauerstrich-Laserspektroskopie-Quelle und ihre Anwendung in hochauflösenden Spektroskopie-Messungen der fundamentalen Rotations- und Schwingungs-Übergänge im Wasserstoff-Molekülion HD^+, stellen den Schwerpunkt dieser Arbeit dar.

Zur Anregung des fundamentalen Übergangs $(\upsilon = 0, L = 0) \rightarrow (\upsilon' = 1, L' = 1)$ im kalten gefangenen Molekülion HD^+ war die Entwicklung einer 5,115 µm Spektroskopie-Quelle notwendig. Sie basiert auf der Differenzfrequenz-Erzeugung aus zwei Laserquellen im mittleren IR-Bereich bei 1064 nm und 1344 nm in einem periodisch gepolten Lithium-Niobat-Kristall (MgO:PPLN), in dem die Strahlung entsteht. Obwohl Absorption der 5 µm Strahlung im Kristall auftritt, konnte eine maximale Ausgangsleistung von 105 µW erzielt werden.

Im Vergleich zu der bisher veröffentlichten oberen Grenze bei 4,57 µm stellt unser Ergebnis von 5,48 µm eine deutliche Erweiterung der oberen Wellenlängenbegrenzung in den Spektralbereich starker Absorption dar.

Die 1344 nm Laserquelle ist ein Eigenbau eines „quantum dot external cavity“ Diodenlasers (QD-ECDL) in Littrow-Anordnung mit einer freien Linienbreite von 5 MHz. Diese Quelle ist in seiner Frequenz auf einen GPS referenzierten femto-Sekunden Ti:Saphir Frequenzkamm stabilisiert. Hingegen ist der 1064 nm Laser auf eine Doppler-freie Resonanz in molekularem Iod stabilisiert. Durch diese Maßnahmen wird eine schmale Linienbreite (ca. 720 kHz) der 5,1 µm Laserstrahlung erzielt. Aufgrund der deutlich geringeren Linienbreite dieser Quelle gegenüber der Dopplerbreite eines typischen (Hyperfein-) Übergangs in kaltem HD^+ von ungefähr 3 MHz, ist die Quelle gut geeignet für die Anwendung in der hochauflösenden Spektroskopie. Beide Laserfrequenzen werden gleichzeitig mit dem Frequenzkamm gemessen, die resultierende Differenzfrequenz bei 5,1 µm wird mit einem Computer errechnet.

Durch den Einbau eines Intensitätsmodulators bei 1344 nm kann das Spektrometer zusätzlich relativ schnell zu jeder Zielfrequenz innerhalb eines Bereichs von 460 MHz um eine vorgegebene Referenzfrequenz verfahren werden. Diese Eigenschaft ermöglicht eine präzise Frequenzänderung bei 5,1 µm mit einer Rate von ca. 35 MHz/s, eine entscheidende Eigenschaft für die erfolgreiche Demonstration des „Hyperfein-Pumpens“ in einen Zielzustand.

Durch die Verstimmung des Spektrometers auf die ungestörte Übergangsfrequenz des fundamentalen Übergangs $(\upsilon = 0, L = 0) \rightarrow (1,1)$ konnte zum ersten Mal die Anregung eines einzelnen Quantenzustands (noch mit magnetischer Entartung der Unterzustände)

demonstriert werden. Zudem konnten Quantenzustände (durch Verwendung nicht entarteter Zustände) adressiert werden.

Darüber hinaus haben wir die Anwendung dieser neu erreichten „Auflösung eines Quantenzustands“ durch die erstmalige Auflösung der Hyperfeinstruktur von zwei der energetisch niedrigsten Zustände in HD^+ darstellen können. Präzise Vermessungen der Abstände zwischen den Zuständen sowie der Absolutfrequenz der Schwingungsübergänge konnten erstmalig demonstriert werden. Die erreichte Frequenzauflösung ist unserer Kenntnis nach bisher besser als die Auflösung vorangegangener Messungen an allen anderen Molekülionen zuvor. Diese neue Technik verdeutlicht, dass sympathisch gekühlte Molekülionen zu höheren Auflösungen in der Spektroskopie gegenüber bisher etablierten Techniken, z. B. der eleganten Ionenstrahl-Methode, führen können.

Das wichtigste Resultat dieser Arbeit im Bereich der Molekülphysik ist der, unserer Kenntnis nach, genaueste Test der *ab initio*-Theorie eines Moleküls überhaupt.

1 Introduction

Today's high resolution spectroscopic experiments strongly benefit from the successes in the field of trapping and cooling of particles achieved during the last few decades. The significance of the fundamental work in this field is evinced by the Nobel prizes for *Dehmelt and Paul* (1989) and *Chu, Phillips and Cohen-Tannoudji* (1997). Improvements in laser cooling of neutral and charged atoms and the ability to reach the cold temperature regime ($T < 1$ mK) strongly promoted the rapidly growing field of ultracold quantum physics within the last years. Therefore, new insights followed in the physics of many-body systems and the observation of a variety of quantum mechanical effects [1], as well as significant advances in frequency metrology [2].
However, the techniques of laser cooling were mainly restricted to atoms and could not be directly applied to molecules, due to the lack of closed optical transitions or the lack of suitable laser sources. In order to transfer to molecules the knowledge gained on trapping and cooling of atoms, new methods for production of cold molecules were required. Most desirably, these methods should be universal and independent of the internal structure of the particles, such as magnetic or electric moments or their energy level structure, making them applicable to a large variety of molecular species, ranging from the most simple of all molecules, e.g. the hydrogen molecules and their isotopomers, to massive and complex molecules, like proteins and polymers.

Cold trapped molecules represent an intense field of activity which has been strongly expanding since the year 2000. Today's sophisticated methods of molecule production, translational and internal cooling, spectroscopy and sensitive detection are opening interesting research grounds for fundamental physics. In particular, cold molecules offer the possibility of studying light-molecule and molecule-molecule interactions in a new temperature regime, previously not accessible.
In atomic physics, modern technology enabled an enormous increase in the spectral resolution, leading e. g. to the most precise measurement of a fundamental constant in nature, the Rydberg constant [3][4][5], as well as to precise microwave and optical clocks [20]. Expectations see a comparable increase of the spectral resolution for molecular systems at low temperatures. Here, the line broadening effects resulting, e. g. from the Doppler effect, high thermal velocities or finite transit times, are expected to be strongly reduced or even eliminated. In particular for molecules, due to the relatively long lifetime of vibrational levels (~ ms to s), the potential line resolution can be huge, with Q-factors $> 10^{14}$. Due to the low translational temperature, the absorption rate can significantly increase, thus enabling efficient excitation even on weak overtone transitions.

High resolution spectroscopic measurements of transition frequencies in molecules, especially in light hydrogen molecules and their isotopomers, are especially interesting for tests of fundamental physics. Within the framework of this thesis, the research has been concentrated on the molecular hydrogen ion HD^+. This molecular ion, containing only two nuclei and one

electron, represents the most simple, stable molecule with an electric dipole-allowed ro-vibronic spectrum, making it an important benchmark system.

A number of novel applications for the molecular hydrogen ion are of interest [6]:

- test of advanced *ab initio* calculations (in particular, QED contributions)
- test concepts for the manipulation of molecules (state preparation, alignment)
- measure certain fundamental constants
- sense fields (blackbody radiation thermometry [7])
- probe fundamental physics laws (e. g. Lorentz invariance, time invariance of fundamental constants)

In the area of probing fundamental constants, Sommerfeld's fine structure constant α, which describes the strength of the electromagnetic interaction in the low energy limit, is presently one of the most important test cases to search for a time- or space-dependence. This development is due to theories which, in attempting to unify the fundamental interactions, allow or even imply variations of the coupling constants [8].
As a dimensionless quantity, $\alpha \simeq 1/137$ offers the possibility of determination without reference to a specific system of units. This is of importance, since the units themselves may also be affected by variations of the constants.

The question whether the value of the fine structure constant α is in fact constant or its value differs by location and over time is subject to ambitious discussions for many years.
First experimental tests of this question examined the spectral lines of distant astronomical objects as well as the products of radioactive decay in the Oklo natural nuclear fission reactor. All experiments were consistent with no change of α [9][10].
The only indication for a possible variation of α so far is found in observations of specific absorption lines produced by interstellar clouds in the light from distant quasars. An apparent shift of wavelengths of specific absorption lines could be reported in Keck telescope and Very Large Telescope (VLT) data, probing a different direction in the universe [11]. According to these observations, the value of α was 10^{10} years ago $\langle \Delta\alpha/\alpha \rangle_{z>1.8} = (+0.61 \pm 0.20) \cdot 10^{-5}$ larger than today.

Several different and independent approaches for the determination of the fine structure constant have been realized.

According to *Jeffery et al.* [12] precise values of α can be obtained from measurements using the quantum Hall effect (QHE). Since $\alpha = e^2/(4\pi\varepsilon_0\hbar c)$ is proportional to e^2, it can be understood as the square of an effective charge "screened by vacuum polarization and seen from an infinite distance." The QHE is characteristic of a completely quantized two-dimensional electron gas. According to measurements performed at NIST, such a gas may be realized in a high-mobility semiconductor device like a silicon metal-oxide-semiconductor field-effect transistor (MOSFET). From very accurate resistance measurements of the

von Klitzing constant R_K ($R_H(i) = U_H(i)/I = R_K/i$, i: plateau of constant U_H), the value of α can be determined according to

$$\alpha = \frac{\mu_0 c e^2}{h} = \frac{\mu_0 c}{2R_k}. \qquad \textbf{(1.1)}$$

According to the demonstration by Krüger et al. [13], the fine-structure constant α was derived from the value of h/m_n (m_n: neutron mass). To do so, a beam of neutrons with a well known wavelength was produced by Bragg reflection in a perfect silicon crystal and the velocity of these neutrons was measured with a very precise time-of-flight method. According to the *de Broglie* equation $h/m_n = \lambda\upsilon$, the product of the wavelength and the velocity is equal to h/m_n.

The fine structure constant was then obtained from:

$$\alpha = \sqrt{2\frac{R_\infty}{c}\frac{h}{m_n}\frac{m_n}{m_e}}. \qquad \textbf{(1.2)}$$

Another way towards to determine α is the measurement of the electron magnetic moment, demonstrated by *Hanneke et al.* [4]. Using a one-electron quantum cyclotron, the measurement gives the electron magnetic moment $\mu = -\frac{g}{2}\mu_B\frac{2\boldsymbol{S}}{\hbar}$ in Bohr magnetons $\mu_B = e\hbar/(2m)$ and electron spin $\boldsymbol{S}$. The value of $g/2$ was obtained with very high accuracy (0.28 ppt). The fine structure constant α is related to *g* by the Standard Model according to:

$$\frac{g}{2} = 1 + C_2\left(\frac{\alpha}{\pi}\right) + C_4\left(\frac{\alpha}{\pi}\right)^2 + C_6\left(\frac{\alpha}{\pi}\right)^3 + C_8\left(\frac{\alpha}{\pi}\right)^4$$
$$+ C_{10}\left(\frac{\alpha}{\pi}\right)^5 + \ \ldots\ + a_{\mu\tau} + a_{hadronic} + a_{weak},$$

with the asymptotic series (C_i are numeric values) and $a_{\mu\tau}$ coming from QED.

The value of m_e/m_p has been determined from measurements of the g-factor of the electron in hydrogen like systems $\left({}^{16}O^{7+}, C^{5+}\right)$ in penning traps [14][15].

One application of more accurate values of the ratio m_e/m_p is to the fine-structure constant α which is related to this ratio by:

$$\alpha = \sqrt{2\frac{R_\infty}{c}\frac{h}{M_{Cs}}\frac{M_{Cs}}{m_p}\frac{m_p}{m_e}}. \qquad \textbf{(1.3)}$$

As mentioned above, the Rydberg constant represents the best known fundamental constant with a relative uncertainty of $5.0 \cdot 10^{-12}$ [5]. The factor h/M_{Cs} in equation (1.3) is of high importance, when the accuracy of this factor is taken into consideration. Therefore in other notations, h/M_{Rb} is used, when the mass of rubidium is taken as a reference instead of the mass of cesium.

The measurements of these important values use different methods. In the work of *Wicht et al.* [16] the value of h/M_{Cs} is obtained by measuring the recoil velocity $v_{rec} = \hbar k / M_{Cs}$ of a cesium atom due to the coherent scattering of a photon in an (Ramsey-Board) atom interferometer.

In the work of *Cladé et al.* [17], the ratio h/M_{Rb} is measured, using Bloch oscillations in a frequency-chirped optical lattice. Following the same principle as for cesium, h/M_{Rb} is determined from the accurate measurement of the rubidium recoil velocity $v_{rec} = \hbar k / M_{Rb}$ when the atom absorbs or emits a photon of wavevector *k*.

The remaining values of M_{Cs} and M_{Rb} (in atomic units u) have been very accurately measured by *Bradley et al.* [18] in a Penning trap, achieving uncertainties ≤ 0.2 ppb.

According to the recent "CODATA 2010 Adjustment of the Values of the Constants" [5], the updated relative standard uncertainties of the fundamental constants are:

	m_e/m_p	m_d/m_p	m_t/m_p	α	R_∞	h/m_p
$u(r)$	$4.1 \cdot 10^{-10}$	$9.2 \cdot 10^{-11}$	$8.2 \cdot 10^{-10}$	$3.2 \cdot 10^{-10}$	$5.0 \cdot 10^{-12}$	$1 \cdot 10^{-9}$

Table 1.1 Relative standard uncertainties $u(r)$ of the CODATA 2010 recommended values of the basic constants and conversion factors of physics and chemistry [5]. Note: the value of h/m_p refers to CODATA 2006.

Thus, the current limitations in the accuracy of determination of α is from h/m_p. However, researchers are looking forward to improve the value of h/m_p in the near future, thereby urging other groups to further reduce the uncertainty of m_e/m_p.

In case of the molecular hydrogen ion, the dependence of the ro-vibronic transitions on the ratio of m_e/μ is of interest. With the reduced mass $\mu = m_p m_d / (m_p + m_d)$ for HD^+ and $\mu = m_p/2$ the dependence is expressed by the following equations:

$$\frac{E_{vib}(h\nu_{vib})}{hc} \sim R_\infty \sqrt{m_e/\mu}, \quad \frac{E_{rot}(h\nu_{rot})}{hc} \sim R_\infty \, m_e/\mu. \tag{1.4}$$

Here, "~" means an approximate dependence.

Thus, measurements of the ro-vibronic energy differences in H_2^+ and HD^+ can lead to the determination of the fundamental mass ratios m_e/m_p and m_p/m_d. Either molecule can contribute to a future improvement of the determination of α.

The molecular hydrogen ion HD^+

Due to its relative simplicity, the HD^+ molecular ion offers the unique possibility to compare accurate theoretical calculations with high-precision experimental measurements including an estimation of the systematical error. Although HD^+ has long been a model system and has been theoretically investigated throughout the last decades, the theoretical publications by far outnumber the experimental ones.

In contrast to the H_2^+ molecule, the molecular hydrogen ion HD^+ posses a permanent dipole moment due to the imbalance of the nuclear masses $\left(m_d \approx 2m_p\right)$, which results in a center of mass shifted with respect to the (charge) center of the molecule (Figure 1.1).

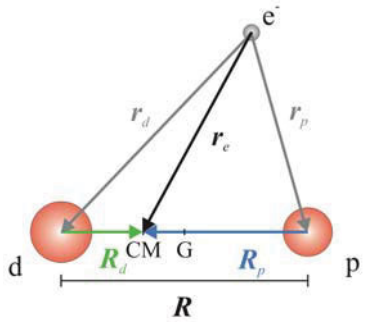

Figure 1.1 Simplified illustration of the HD^+ molecular ion (G: geometric centre), the charge centre is at G. Since $G \neq CM$ a permanent dipole moment exists as well as vibrational transition moments.

As will be described in more detail in chapter 2.1, the molecule therefore can easily absorb and emit electromagnetic radiation. In the quantum mechanical description, the energy levels are approximately obtained by solving the time-independent *Schrödinger equation*. In the *Born-Oppenheimer approximation*, any coupling of nuclear and electron motion is neglected and the dependence of the molecule's total energy U on the internuclear distance R is emphasized (Figure 1.2).

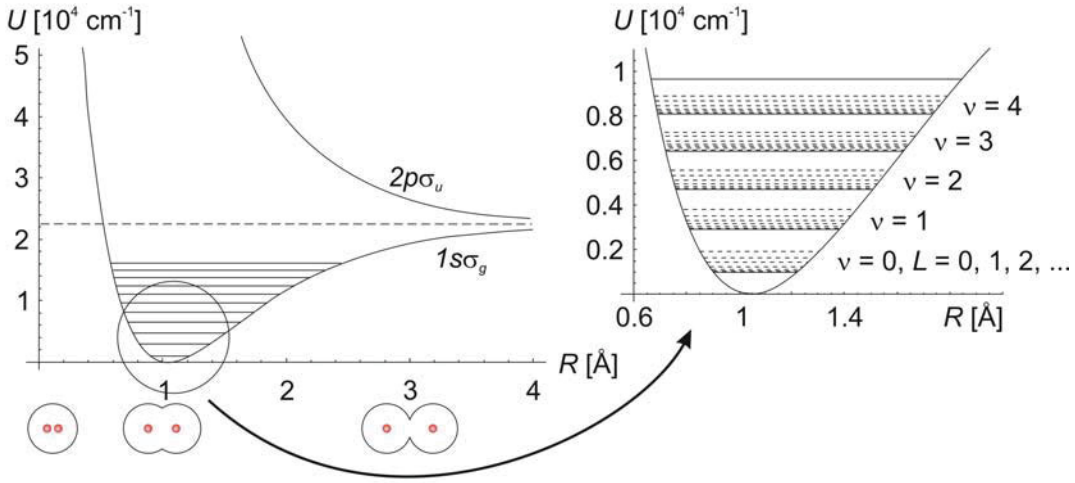

Figure 1.2 Potential energy curves of the ground (1sσ) and first excited (2pσ) electronic state as a function of the internuclear distance R of the HD^+ molecular ion according the *Born-Oppenheimer approximation* (after [77]).

The electronic ground state and the first excited state are labeled with 1sσ and 2pσ, respectively. The following nomenclature is used: The main quantum number of the electronic state is expressed by the Roman number, whereas the Latin letter gives the electron's orbital angular momentum quantum number (s = 0, p = 1, etc.). Accordingly, it is also the angular momentum of the state of the atom H (D), in which the molecule can dissociate $\left(\mathrm{HD}^+\left(1\mathrm{s}\sigma_\mathrm{g}\right)\right)\left(\mathrm{v}'=4\right)+h\nu_{266\,\mathrm{nm}} \rightarrow \mathrm{HD}^+\left(2\mathrm{p}\sigma_\mathrm{u}\right) \rightarrow \mathrm{H}(1\mathrm{s})+\mathrm{D}^+$ or $\mathrm{D}(1\mathrm{s})+\mathrm{H}^+\big)$ or equivalently, from which the molecule can originate. The orbital angular momentum of the bonding electron with respect to the internuclear axis (σ =0, π = 1, etc.) is represented by the Greek letter. An atom with angular momentum number *s* can only yield a σ molecule, whereas an atomic angular quantum number of *p* can yield both σ and π molecules, since *p* can have contributions in all spatial components p_x, p_y, p_z.

According to Figure 1.2, the potential energy distribution with respect to the nuclear separation *R* shows the following behavior.

The derivative of the potential energy with respect to the internuclear separation *R* gives the force acting on the atoms. Therefore, the potential of the excited state 2pσ is repulsive for all values of *R*. In contrast, the potential of the ground state 1sσ is only repulsive for small values of *R*, attractive for large values and zero at its minimum. Located close to the value of the internuclear separation of $R \approx 1$ Å, this value corresponds to the place, the atoms arrange. For large values of *R* the atoms are merely completely separated and the potential curves $U_{1s\sigma}$ and $U_{2p\sigma}$ approach each other due to the fact that the energy of the separated atoms is equal for both cases.

Figure 1.2 (left) illustrates the ro-vibrational energy levels of the molecule in the electronic ground state obtained by solving the *radial Schrödinger equation*. Here, the rovibrational states are described by the vibrational quantum number υ and the rotational quantum number *L*. 22 vibrational levels exist [19], each containing up to 49 rotational levels ($L = 0, 1, 2, \ldots, 48$) [22].

Actual values of the $\left(\upsilon=0, L=0\right) \rightarrow \left(\upsilon'=1, L'=1\right)$ vibrational and $\left(\upsilon=0, L=0\right) \rightarrow \left(\upsilon'=0, L'=1\right)$ rotational transition frequencies are:

$$\nu_{vib} \approx 1955 \text{ cm}^{-1}, \qquad \nu_{rot} \approx 44 \text{ cm}^{-1}. \tag{1.5}$$

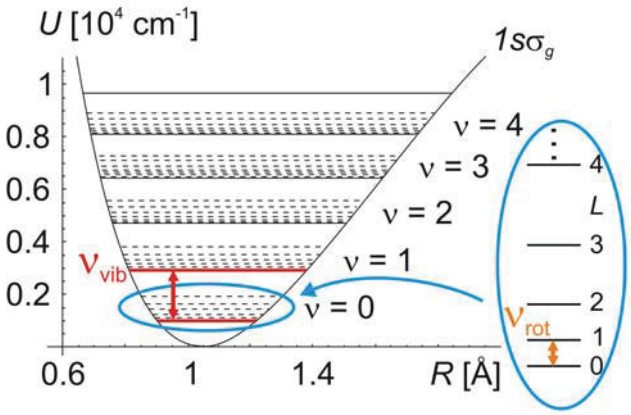

Figure 1.3 Illustration of the rotational and vibrational transitions within the ground electronic state (1sσ) of the HD^+ molecular ion.

Outline history

As mentioned above, the theoretical publications on H_2^+, HD^+, etc. by far outnumber the experimental ones. *Ab initio* calculations of dissociation energies of a multitude of rovibrational states in H_2^+ and HD^+ were reported by *Moss* [21][22] with a relative accuracy of 5 x 10^{-9}, including leading order relativistic and radiative corrections. Very high accuracy for the nonrelativistic (i. e. Schrödinger) rovibrational transition frequencies were obtained by [23][24] using the variational method. Here, a negligible uncertainty (relative accuracies are at 5 x 10^{-24} and 8 x 10^{-30} respectively) was achieved. According to the work of *V. Korobov*, the full relativistic rovibrational energies have been calculated *ab initio* with a precision about 1 x 10^{-10} [40]. Precise *ab initio* calculations of the hyperfine structure of the rovibrational states of the HD^+ have been carried out by *Bakalov et al*. [42], reaching an estimated uncertainty of about 50 kHz. *Korobov et al.* reported relativistic corrections of $m\alpha^6(m/M)$ order to the hyperfine structure of the H_2^+ molecular ion. Therefore the uncertainty in frequency intervals between hyperfine sublevels of a given rovibronic state could be reduced to about 10 ppm [25]. Recently, this has also been applied by Korobov to HD^+, and the uncertainties of the hyperfine contributions to a vibrational or rotational transition have been reduced to < 10 kHz for most transitions [90]. The theoretical accuracies achieved are summarized in Figure 1.4 and Figure 1.5.

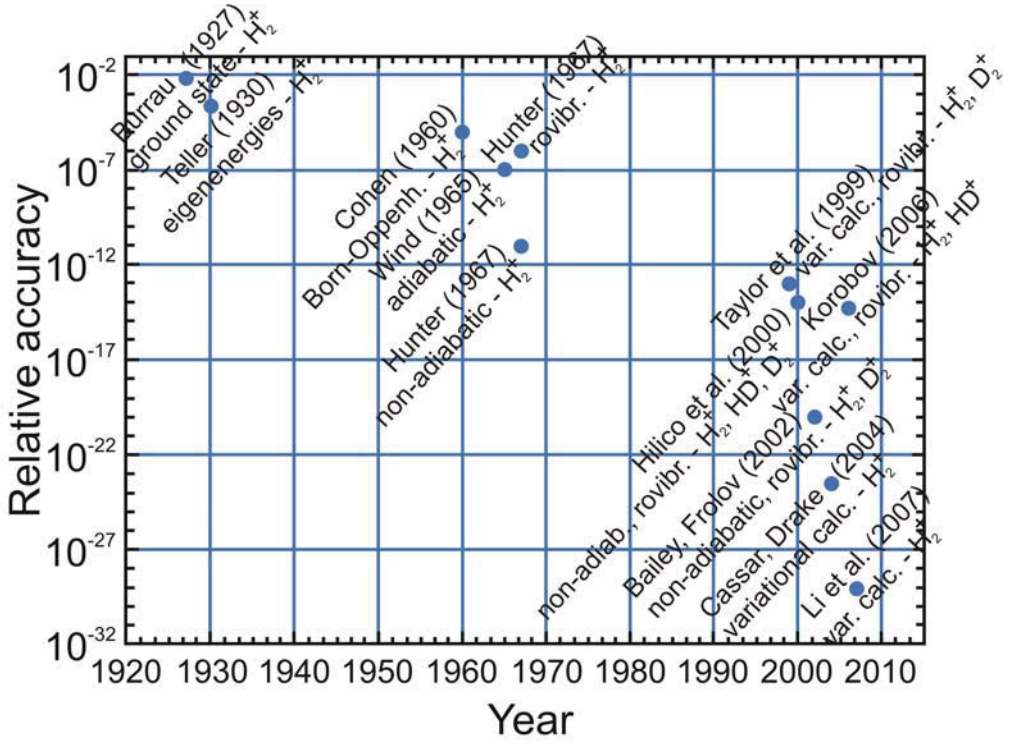

Figure 1.4 Overview on the theoretical inaccuracies for the Schrödinger eigenenergies of hydrogen molecular ions with the given calculated quantities. Non-relativistic calculations using the Born-Oppenheimer (adiabatic) or non-adiabatic approximations, or the variational methods are indicated and will be described in chapter 2 (from [35][36]).

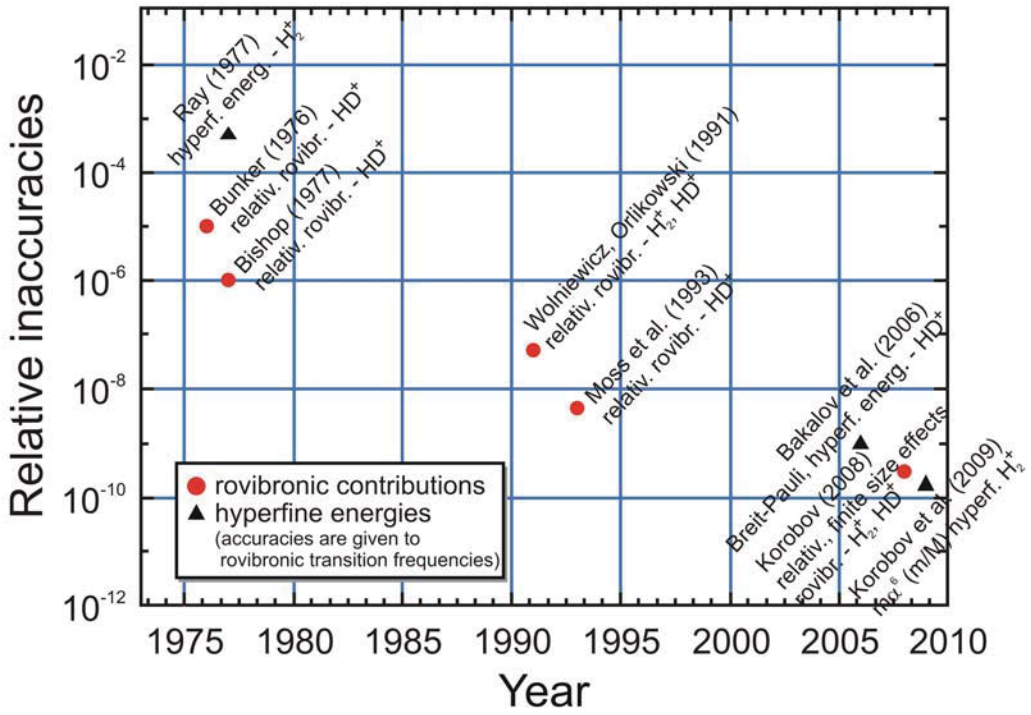

Figure 1.5 Overview on the theoretical accuracies for the full ro-vibrational transition energies in hydrogen molecular ions including the given calculated quantities and used methods. Radiative and relativistic corrections as well as corrections due to the finite size of the proton and the deuteron are taken into account in the results. The rovibronic contributions are shown in red, whereas the hyperfine contributions are indicated in black (from [35][36]).

Concentrating on the spectroscopy of the ro-vibrational transitions in molecular hydrogen and its isotopomers, several investigations on room-temperature molecular hydrogen ions or on ion beams were performed in the past (Figure 1.6).

Radio-frequency spectroscopy of the hyperfine structure of vibrational levels of H_2^+ ions, trapped in an ion trap, was performed by *Jefferts* in 1969 [26]. *Wing et al* [27] observed a few low-lying vibration-rotational transitions $(\upsilon = 1-3)$ of HD^+, e.g. $(\upsilon = 1, L = 1) \rightarrow (\upsilon' = 0, L' = 2)$, for the first time, using an ion-beam experiment. They observed a partially resolved hyperfine structure. The work of *Carrington et al*. [28][29] was the first to probe ro-vibrational transitions close to the dissociation limit $(\upsilon = 14-22)$ via radiofrequency / infrared double resonance measurements as well as resolving the hyperfine structures in these bands [30]. Microwave and laser spectroscopy of rotational and rovibrational transitions of H_2^+, HD^+ and D_2^+ close to dissociation was carried out also in an ion beam by [31][32]. The highest accuracies for dissociation energies were obtained by *Zhang et al.* with accuracies $\simeq 1\times10^{-6}$ [33]. The highest spectroscopic accuracy so far was reported from our group by the measurement of *Koelemeij et al.* [34], achieving an accuracy of 2 ppb by measuring the frequency of a vibrational overtone transition $\upsilon = 0 \rightarrow \upsilon = 4$.

The experimental accuracies achieved are summarized in Figure 1.6. An overview of the theoretical and experimental works in our group is given in Figure 1.7.

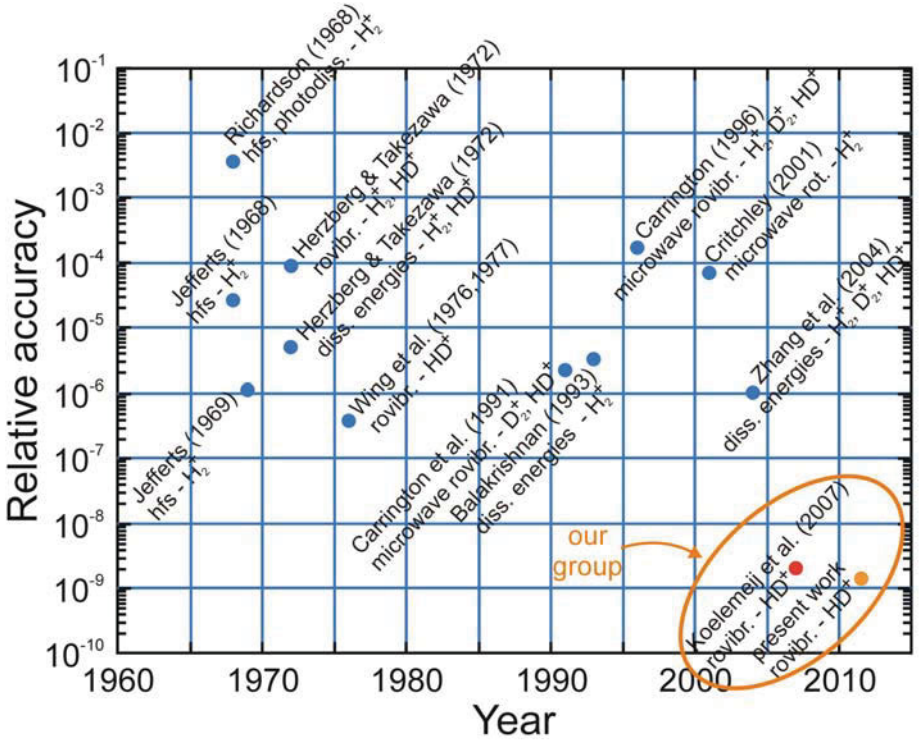

Figure 1.6 Overview on the experimental accuracies for the hyperfine (hfs), rotational and rovibrational transition frequencies in hydrogen molecular ions (H_2^+ , HD^+ , D_2^+) (from [35][74], modified).

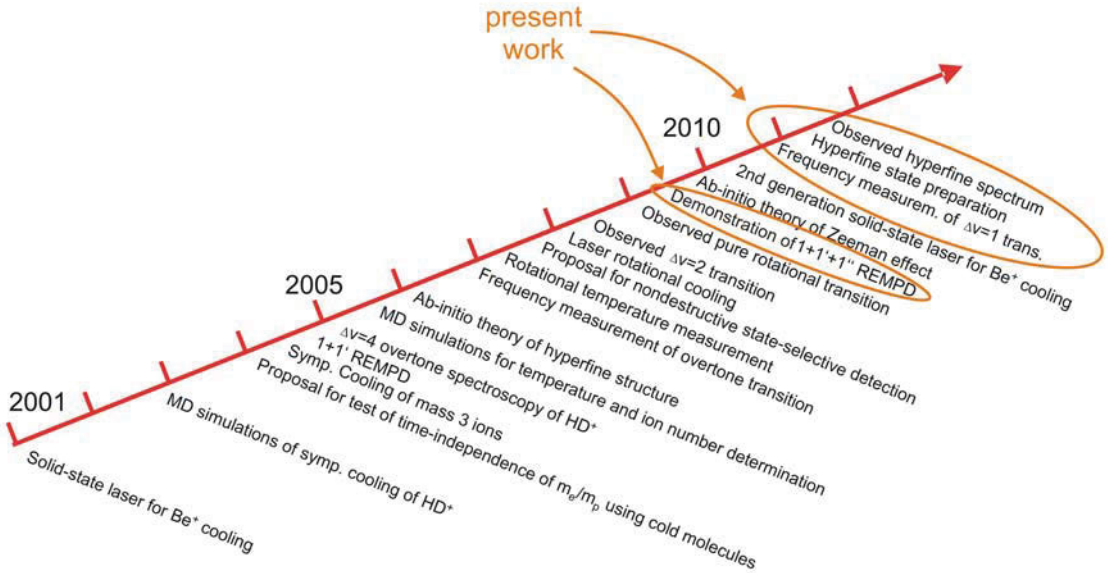

Figure 1.7 Overview on the theoretical and experimental works at the Institute for Experimental Physics in Düsseldorf (from [36]).

Objectives of this work

The knowledge of the fundamental constants and their accuracies is of highest interest in the field of physics, especially for fundamental tests. As emphasized above, precise high resolution spectroscopy measurements pave the way for their determination. Experimental works continuously benefit from technical innovations as well as from progress in theory, leading to higher accuracies in the experimental results and the unique possibility to compare them with *ab initio* calculations.

Taking benefit of the knowledge on the molecular hydrogen ion HD^+ in our group, we pursued high resolution spectroscopy of the fundamental transition, $(\upsilon = 0, L = 0) \rightarrow (\upsilon' = 1, L' = 1)$ within the framework of this thesis (Figure 1.8). This transition can be addressed with a laser at 5.115 µm. The development of a 5.1 µm spectrometer source and its application to high resolution measurements of the ro-vibrational fundamental transitions of the HD^+ molecular ion represent the main tasks of this work.

The spectroscopy laser source is based on the difference-frequency generation of two mid-IR laser sources at 1064 nm and 1344 nm respectively, in a periodically poled lithium niobate crystal (MgO:PPLN), generating the radiation used for the spectroscopy at 5.115 µm. The 1344 nm laser source is frequency stabilized to a GPS-referenced femtosecond Ti:sapphire frequency comb, whereas the 1064 nm laser is stabilized to a Doppler-free resonance in molecular iodine, yielding a narrow linewidth (about 720 kHz) laser wave at 5.115 µm. With a linewidth much smaller than the Doppler width of about 3 MHz of a typical fundamental transition in cold HD^+, the source is well suited for high resolution spectroscopy. Both laser frequencies are simultaneously measured with the frequency comb and the difference frequency at 5.115 µm is calculated with a computer (Figure 1.8).

This 5.115 µm spectrometer laser was used for high-resolution spectroscopy of cold, trapped molecular ions. Due to the spectrometer's ability to relatively-quickly frequency tune to any desired frequency within a range of 460 MHz around a set centre frequency, e.g. the unperturbed transition frequency of the fundamental transition $(\upsilon = 0, L = 0) \rightarrow (1,1)$, it was possible to demonstrate for the first time the addressing of single quantum states.

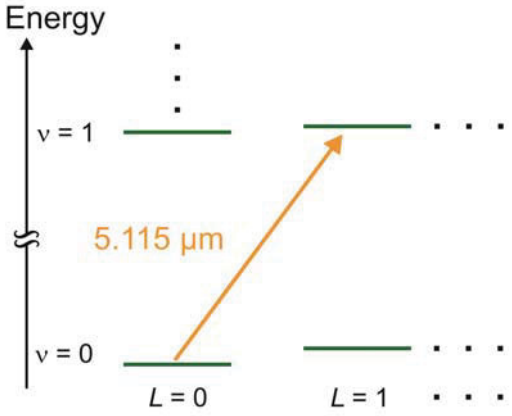

Figure 1.8 Simplified schematic of the fundamental transition $(\upsilon = 0, L = 0) \rightarrow (\upsilon' = 1, L' = 1)$ in the molecular hydrogen ion to be addressed with the 5.1 µm spectrometer source.

Furthermore, we demonstrated applications of this newly achieved quantum state "resolution": We resolved, for the first time, the hyperfine structure of two low-lying states of HD^+. Precise measurements of the hyperfine spacings, as well as the absolute frequency of the vibrational transitions could be demonstrated, both having never been measured before. The achieved frequency resolution is, to our knowledge, better than any previous measurement on any molecular ion.

With this new technique, it can be shown that the approach of sympathetically cooled molecular ions can lead to higher resolution in spectroscopy than established techniques, e.g. the elegant ion beam method [27].

On the molecular physics side, the main result of this work is, to our knowledge, the most precise test of *ab initio* theory of any molecule so far, improving our previous measurement in 2007 [34].

2 The HD^+ molecular ion

2.1 Molecular theory

In contrast to the even simpler H_2^+, the HD^+ molecular ion, consisting of a hydrogen and a deuteron nucleon, possesses a shifted center of mass with respect to the center of charge (Figure 2.1). This manifests itself in a permanent electric dipole moment. Within the framework of classical physics, the rotational and vibrational motion of the nuclei with respect to the center of mass can be described as an oscillating charge. Interpreted as a Hertzian dipole, the molecule therefore can absorb and dissipate electromagnetic radiation.
In the quantum mechanical treatment, the molecule's corresponding ro-vibrational energy is quantized and only discrete transitions are possible. These transitions are electric-dipole allowed because the above imbalance leads to nonzero electric dipole transition moments. The transitions can be addressed by monochromatic radiation and are of special interest for laser spectroscopy.

2.1.1 Spin-independent approximation

The theoretical description of the HD^+ molecular ion, starting from the nonrelativistic three-body Hamiltonian (Schrödinger equation), has undergone several steps of development, well reviewed in [37]. Based on nonrelativistic calculations using the *variational method* for the Coulomb bound-state problem described in [38], a precision of about 10^{-14}-10^{-30} has been reached for the range of states with $L \leq 4$ and $\upsilon \leq 4$ [40][45].
In addition, the leading relativistic [40] and radiative [41] corrections have to be considered.

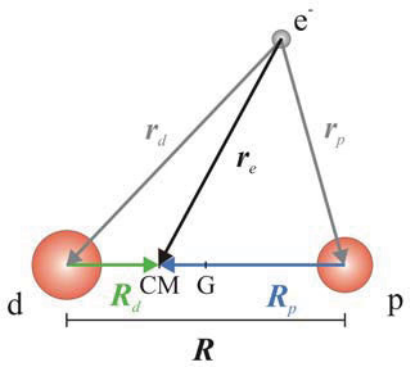

Figure 2.1 Simplified illustration of the HD^+ molecular ion (G: geometric centre). As the electron distribution is symmetric with respect to the mid-plane, the charge centre is at G. Since $G \neq CM$, a permanent dipole moment exists. $\boldsymbol{R}_d, \boldsymbol{R}_p, \boldsymbol{r}_e$ are the coordinates of the deuteron (d), proton (p) and electron (e) with respect to the centre of mass (CM) of the molecule, respectively. Here: $\boldsymbol{r}_d = \boldsymbol{r}_e - \boldsymbol{R}_d$, $\boldsymbol{r}_p = \boldsymbol{r}_e - \boldsymbol{R}_p$ and $\boldsymbol{R} = \boldsymbol{R}_p - \boldsymbol{R}_d$.

Leading-order relativistic corrections

The calculation of QED corrections will be used in the following as an expansion in terms of α, the fine structure constant.
The following consideration of HD^+ refers to [40] and makes use of a Breit-Pauli-type Hamiltonian as initial approximation. According to Figure 2.1 a centre-of-mass frame is used. $\boldsymbol{P}_d, \boldsymbol{P}_p$ and $\boldsymbol{p}_e$ are the momenta of the deuteron (d), proton (p) and electron (e), $\boldsymbol{R}_d, \boldsymbol{R}_p, \boldsymbol{r}_e$ are the coordinates with respect to the mass-center and $\boldsymbol{r}_d = \boldsymbol{r}_e - \boldsymbol{R}_d$, $\boldsymbol{r}_p = \boldsymbol{r}_e - \boldsymbol{R}_p$, $\boldsymbol{R} = \boldsymbol{R}_p - \boldsymbol{R}_d$. $Z_d = Z_p = 1$ are the nuclear charges, m_d, m_p, m_e are the mass of deuteron, proton and electron, respectively. The atomic units $\left(\hbar = e = m_e = 1\right)$ are used.
The contributions to the leading order relativistic corrections $\left(R_\infty \alpha^2\right)$ in the Breit-Pauli-Hamiltonian will be presented in explicit form in different terms.

The relativistic correction for the *bound electron* represents the major contribution,

$$E_{rc}^{(2)} = \alpha^2 \left\langle -\frac{\boldsymbol{p}_e^4}{8m_e^3} + \frac{4\pi}{8m_e^3}\left[Z_d \delta\left(r_d\right) + Z_p \delta\left(r_p\right)\right]\right\rangle. \qquad \textbf{(2.1)}$$

Additional corrections take the finite mass of nuclei into consideration and are called recoil corrections. The first contribution is the *transverse photon exchange*,

$$\begin{aligned} E_{tr-ph}^{(2)} = {} & \frac{\alpha^2 Z_d}{2m_e m_d}\left\langle \frac{\boldsymbol{p}_e \boldsymbol{P}_d}{r_d} + \frac{\boldsymbol{r}_d\left(\boldsymbol{r}_d \boldsymbol{p}_e\right)\boldsymbol{P}_d}{r_d^3}\right\rangle \\ & + \frac{\alpha^2 Z_p}{2m_e m_p}\left\langle \frac{\boldsymbol{p}_e \boldsymbol{P}_p}{r_p} + \frac{\boldsymbol{r}_p\left(\boldsymbol{r}_p \boldsymbol{p}_e\right)\boldsymbol{P}_p}{r_p^3}\right\rangle \\ & - \frac{\alpha^2 Z_d Z_p}{2m_d m_p}\left\langle \frac{\boldsymbol{P}_d \boldsymbol{P}_p}{R} + \frac{\boldsymbol{R}\left(\boldsymbol{R}\boldsymbol{P}_d\right)\boldsymbol{P}_p}{R^3}\right\rangle. \end{aligned} \qquad \textbf{(2.2)}$$

Note that the last term of (2.2) contributes about 10 % to $E_{tr-ph}^{(2)}$ and is therefore not negligible for the further treatment.
For heavy particles, the contribution of *kinetic energy* has to be included,

$$E_{kin}^{(2)} = -\alpha^2 \left\langle \frac{\boldsymbol{P}_d^4}{8m_d^3} + \frac{\boldsymbol{P}_p^4}{8m_p^3}\right\rangle. \qquad \textbf{(2.3)}$$

In the further discussion of the $\left(R_\infty \alpha^2\right)$ order, the nuclear spin of the proton $\left(I_p = 1/2\right)$ has to be taken into consideration. Note that the corresponding expression for the deuteron $\left(I_d = 1\right)$ vanishes.

$$E^{(2)}_{Darwin} = \frac{\alpha^2 4\pi Z_p}{8m_p^2}\left\langle \delta\left(\boldsymbol{r}_p\right)\right\rangle. \tag{2.4}$$

The last contribution is the leading-order electric charge finite size correction, defined both for proton and deuteron as:

$$E^{(2)}_{nuc} = \sum_{i=d,p} \frac{2\pi Z_i \left(R_i/a_0\right)^2}{3}\left\langle \delta\left(\boldsymbol{r}_i\right)\right\rangle. \tag{2.5}$$

R_i is the root-mean-square (rms) of the radius of the nuclear electric charge distribution, which is connected to the internal structure of complex particles.

The total contribution from the Breit-Pauli-Hamiltonian thus is:

$$\boxed{E_{\alpha^2} = E^{(2)}_{rc} + E^{(2)}_{kin} + E^{(2)}_{tr-ph} + E^{(2)}_{Darwin} + E^{(2)}_{nuc}.} \tag{2.6}$$

Leading-order radiative corrections

The contributions to the leading order radiative corrections of the order $\left(R_\infty \alpha^3\right)$ for a one electron molecular system are presented in explicit form in different terms, considering only the spin-independent part [40]. According to the *Bethe-logarithm*

$$\beta\left(L,\upsilon\right) = \frac{\left\langle \mathbf{J}\left(H_0 - E_0\right)\ln\left[\left(H_0 - E_0\right)/R_\infty\right]\mathbf{J}\right\rangle}{\left\langle\left[\mathbf{J},\left[H_0,\mathbf{J}\right]\right]/2\right\rangle}, \tag{2.7}$$

the one-loop self energy correction is given by

$$E^{(3)}_{se} = \frac{4\alpha^3}{3m_e^3}\left(\ln\frac{1}{\alpha^2} - \beta\left(L,\upsilon\right) + \frac{5}{6} - \frac{3}{8}\right)\left\langle Z_d\delta\left(\boldsymbol{r}_d\right) + Z_p\delta\left(\boldsymbol{r}_p\right)\right\rangle. \tag{2.8}$$

The Bethe logarithm represents the most difficult numerical problem in the computation of QED corrections of the three-body bound states [41].
The operator $\mathbf{J} = \Sigma_a z_a \boldsymbol{p}_a / m_a$ is defined as the *electric current density operator* of the system.

$\upsilon = 0,\ L = 0$	$\upsilon = 1,\ L = 1$
3.01233625(1)	3.01260814(3)

Table 2.1 The Bethe logarithm for the lowest rotational, L, and vibrational, υ, states of the hydrogen molecular ion HD^+ [90].

The next contribution of order $\left(R_\infty \alpha^3\right)$ is the *anomalous magnetic moment*

$$E_{anom}^{(3)} = \frac{\pi\alpha^2}{m_e^2}\left[\frac{1}{2}\left(\frac{\alpha}{\pi}\right)\right]\left\langle Z_d \delta\left(\boldsymbol{r}_d\right) + Z_p \delta\left(\boldsymbol{r}_p\right)\right\rangle. \tag{2.9}$$

The *one-loop vacuum polarization* of order $\left(R_\infty \alpha^3\right)$ represents another contribution

$$E_{vp}^{(3)} = \frac{4\alpha^3}{3m_e^2}\left(-\frac{1}{5}\right)\left\langle Z_d \delta\left(\boldsymbol{r}_d\right) + Z_p \delta\left(\boldsymbol{r}_p\right)\right\rangle. \tag{2.10}$$

The last contribution is the *one transverse photon exchange*

$$E_{tr-ph}^{(3)} = \alpha^3 \sum_{i=d,p}\left[\frac{2Z_i^2}{3m_e m_i}\left(-\ln\alpha - 4\beta\left(L,\upsilon\right) + \frac{31}{3}\right)\left\langle \delta\left(\boldsymbol{r}_i\right)\right\rangle - \frac{14Z_i^2}{3m_e m_i} Q\left(r_i\right)\right], \tag{2.11}$$

where $Q\left(r\right)$ is the Q term introduced by Araki and Sucher [43]

$$Q\left(r\right) = \lim_{\rho\to 0}\left\langle \frac{\Theta\left(r-\rho\right)}{4\pi r^3} + \left(\ln\rho + \gamma_E\right)\delta\left(\boldsymbol{r}\right)\right\rangle. \tag{2.12}$$

The total contribution of relativistic corrections thus follows as:

$$\boxed{E_{\alpha^3} = E_{se}^{(3)} + E_{anom}^{(3)} + E_{vp}^{(3)} + E_{tr-ph}^{(3)}.} \tag{2.13}$$

Higher-order relativistic corrections of order $R_\infty \alpha^4 \sim m_e c^2 \alpha^6$ and radiative corrections of order $R_\infty \alpha^5$ have been calculated for H_2^+ and HD^+ in [45].

2.1.2 Rotational levels and quantum states

In a diatomic molecule, a rotational level of quantum number J is $(2J+1)$-fold degenerate. In the case of HD^+ with its electron spin $\boldsymbol{S}_e$, nuclei with nuclear spin $\boldsymbol{I}_d, \boldsymbol{I}_p$, a rotational level L possesses $(2S_e+1)(2I_d+1)(2I_p+1)(2L+1)$ quantum states.

The degeneracy is partially lifted by the hyperfine interactions into a number of hyperfine states. These states split according to the electron spin - nuclear spin interaction $(\sim \boldsymbol{S}_e \cdot \boldsymbol{I}_{d,p})$ and / or the electron spin – rotation interaction $(\sim \boldsymbol{S}_e \cdot \boldsymbol{L})$.

For HD^+ with its unpaired electron $(\boldsymbol{S}_e = 1/2)$ and its nuclei with nuclear spins $\boldsymbol{I}_p = 1/2$, $\boldsymbol{I}_d = 1$, the molecule possess 4 (singlet) hyperfine states in zero magnetic field for $L = 0$. For $L = 1$ the number of hyperfine states increases to 10 (4 multiplets), see Figure 2.2. For $L \geq 2$ it is 12. The reference is the "*spin-independent*" transition frequency $f_0 = 58\ 605\ 052.139$ MHz. Here the nuclear and electron spin are zero.

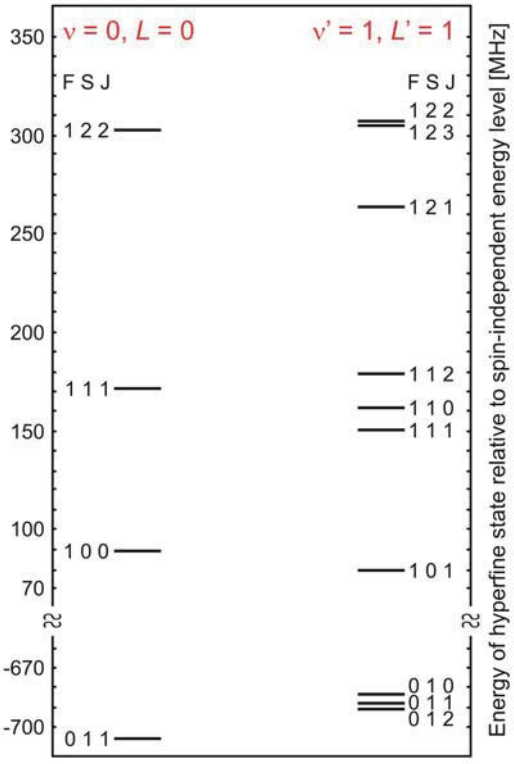

Figure 2.2 Energy diagram of the hyperfine states of the HD^+ molecular ion in zero magnetic field. Left side: the ro-vibrational ground level $(\upsilon = 0,\ L = 0)$, right side: the exited level $(\upsilon' = 1,\ L' = 1)$. The states are labelled by the approximate quantum numbers (F, S, J) according to the corresponding coupling scheme (2.19).

2.1.3 Spin-dependent Hamiltonian

The important contribution of the hyperfine energy has been investigated using adiabatic [44] and two-state adiabatic [30] approximations. The calculations included the electron-nuclear spin-spin and the electron-spin-rotation interactions and their theoretical predictions were in agreement with the spectroscopic measurements of *Wing et al.* and *Carrington et al.*
The comparison with precise r. f. measurements [30] however revealed a slight disagreement with the approximate theory leading to a further improvement in accuracy of *ab-initio* calculations of the energy levels [42].

The following consideration of HD^+ refers to [42] and makes use of a Breit-Pauli-type Hamiltonian to describe the spin interactions in the HD^+ ion and high-accuracy variational nonrelativistic Coulomb wavefunctions as initial approximations. $\boldsymbol{L}_i = \boldsymbol{R}_i \times \boldsymbol{P}_i$ are the orbital momenta of the particles. $\mu_e = -(1+\kappa_e)$ is the magnetic moment of an electron in Bohr magnetons, and $\mu_{p,d}$ are the magnetic moments of proton and deuteron in nuclear magnetons, Q_d is the deuteron quadrupole moment.

The spectrum of the HD^+ ion has been calculated using a Hamiltonian which takes the electromagnetic interactions of its constituents into account:

$$H = H^{NR} + V^{sh} + V^{spin}. \tag{2.14}$$

Here, H^{NR} is the nonrelativistic three-body Hamiltonian, while the correction term V^{sh} collects the contributions of the spin-independent interactions. It has been calculated in [40] as presented above, including the relativistic and radiative corrections up to an order $m\alpha^6$ and $m\alpha^7$ respectively [45]. The other correction term V^{spin} describes the spin interaction Hamiltonian and is the sum of pairwise interactions:

$$V^{spin} = V_{ep} + V_{ed} + V_{pd}. \tag{2.15}$$

The electron-proton and electron-deuteron interactions are given (in units $e = \hbar = 1$) by:

$$\begin{aligned} V_{ep} = \alpha^2 \Bigg\{ & \frac{1+2\kappa_e}{2m_e^2} \frac{(\boldsymbol{r}_p \times \boldsymbol{p}_e)\boldsymbol{S}_e}{r_p^3} - \frac{1+\kappa_e}{m_e m_p} \frac{(\boldsymbol{r}_p \times \boldsymbol{P}_p)\boldsymbol{S}_e}{r_p^3} - \frac{2\mu_p - 1}{2m_p^2} \frac{(\boldsymbol{r}_p \times \boldsymbol{P}_p)\boldsymbol{I}_p}{r_p^3} \\ & + \frac{\mu_p}{m_e m_p} \frac{(\boldsymbol{r}_p \times \boldsymbol{p}_e)\boldsymbol{I}_p}{r_p^3} - \frac{8\pi}{3} \frac{\mu_e \mu_p}{m_e m_p} \delta(\boldsymbol{r}_p)(\boldsymbol{S}_e \cdot \boldsymbol{I}_p) \\ & + \frac{\mu_e \mu_p}{m_e m_p} \frac{r_p^2(\boldsymbol{S}_e \cdot \boldsymbol{I}_p) - 3(\boldsymbol{r}_p \cdot \boldsymbol{S}_e)(\boldsymbol{r}_p \cdot \boldsymbol{I}_p)}{r_p^5} \Bigg\}, \end{aligned} \tag{2.16}$$

$$V_{ed} = \alpha^2 \left\{ \frac{1+2\kappa_e}{2m_e^2} \frac{(\boldsymbol{r}_d \times \boldsymbol{p}_e)\boldsymbol{S}_e}{r_d^3} - \frac{1+\kappa_e}{m_e m_d} \frac{(\boldsymbol{r}_d \times \boldsymbol{P}_p)\boldsymbol{S}_e}{r_d^3} - \frac{1}{m_d}\left[\frac{\mu_d}{2m_p} - \frac{1}{2m_d}\right] \frac{(\boldsymbol{r}_p \times \boldsymbol{P}_p)\boldsymbol{I}_p}{r_d^3} \right.$$
$$+ \frac{\mu_d}{2m_e m_p} \frac{(\boldsymbol{r}_d \times \boldsymbol{p}_e)\boldsymbol{I}_d}{r_d^3} - \frac{4\pi}{3} \frac{\mu_e \mu_d}{m_e m_p} \delta(\boldsymbol{r}_d)(\boldsymbol{S}_e \cdot \boldsymbol{I}_d)$$
$$\left. + \frac{\mu_e \mu_d}{2m_e m_p} \frac{r_d^2(\boldsymbol{S}_e \cdot \boldsymbol{I}_d) - 3(\boldsymbol{r}_d \cdot \boldsymbol{S}_e)(\boldsymbol{r}_d \cdot \boldsymbol{I}_d)}{r_d^5} \right\} + \frac{Q_d}{2} \frac{r_d^2 I_d^2 - 3(\boldsymbol{r}_d \cdot \boldsymbol{I}_d)^2}{r_d^5}.$$

The proton-deuteron interaction is described by:

$$V_{pd} = \alpha^2 \left\{ -\frac{2\mu_p - 1}{2m_p^2} \frac{[\boldsymbol{R} \times \boldsymbol{P}_p]\boldsymbol{I}_p}{R^3} + \frac{\mu_p}{m_p m_d} \frac{[\boldsymbol{R} \times \boldsymbol{P}_d]\boldsymbol{I}_p}{R^3} + \frac{1}{m_d}\left[\frac{\mu_d}{2m_p} - \frac{1}{2m_d}\right] \frac{[\boldsymbol{R} \times \boldsymbol{P}_d]\boldsymbol{I}_d}{R^3} \right.$$
$$- \frac{\mu_d}{2m_p^2} \frac{[\boldsymbol{R} \times \boldsymbol{P}_p]\boldsymbol{I}_d}{R^3} - \frac{4\pi}{3} \frac{\mu_p \mu_d}{m_p^2} \delta(\boldsymbol{R})(\boldsymbol{I}_d \cdot \boldsymbol{I}_p)$$
$$\left. + \frac{\mu_p \mu_d}{2m_p^2} \frac{R^2(\boldsymbol{I}_d \cdot \boldsymbol{I}_p) - 3(\boldsymbol{R} \cdot \boldsymbol{I}_d)(\boldsymbol{R} \cdot \boldsymbol{I}_p)}{R^5} \right\}$$
$$- \frac{Q_d}{2} \frac{R^2 \boldsymbol{I}_d^2 - 3(\boldsymbol{R} \cdot \boldsymbol{I}_d)^2}{R^5}. \qquad \textbf{(2.17)}$$

The nuclear spin-spin contact interaction is negligibly small and therefore omitted from consideration.

The effective spin Hamiltonian is obtained by averaging (2.16) and (2.17) over the spatial degrees of freedom:

$$H_{eff}^{hfs} = E_1(\boldsymbol{L} \cdot \boldsymbol{S}_e) + E_2(\boldsymbol{L} \cdot \boldsymbol{I}_p) + E_3(\boldsymbol{L} \cdot \boldsymbol{I}_d) + E_4(\boldsymbol{I}_p \cdot \boldsymbol{S}_e) + E_5(\boldsymbol{I}_d \cdot \boldsymbol{S}_e)$$
$$+ E_6\left\{2L^2(\boldsymbol{I}_p \cdot \boldsymbol{S}_e) - 3\left[(\boldsymbol{L} \cdot \boldsymbol{I}_p)(\boldsymbol{L} \cdot \boldsymbol{S}_e) + (\boldsymbol{L} \cdot \boldsymbol{S}_e)(\boldsymbol{L} \cdot \boldsymbol{I}_p)\right]\right\}$$
$$+ E_7\left\{2L^2(\boldsymbol{I}_d \cdot \boldsymbol{S}_e) - 3\left[(\boldsymbol{L} \cdot \boldsymbol{I}_d)(\boldsymbol{L} \cdot \boldsymbol{S}_e) + (\boldsymbol{L} \cdot \boldsymbol{S}_e)(\boldsymbol{L} \cdot \boldsymbol{I}_d)\right]\right\} \qquad \textbf{(2.18)}$$
$$+ E_8\left\{2L^2(\boldsymbol{I}_p \cdot \boldsymbol{I}_d) - 3\left[(\boldsymbol{L} \cdot \boldsymbol{I}_p)(\boldsymbol{L} \cdot \boldsymbol{I}_d) + (\boldsymbol{L} \cdot \boldsymbol{I}_d)(\boldsymbol{L} \cdot \boldsymbol{I}_p)\right]\right\}$$
$$+ E_9\left[L^2 I_d^2 - \tfrac{3}{2}(\boldsymbol{L} \cdot \boldsymbol{I}_d) - 3(\boldsymbol{L} \cdot \boldsymbol{I}_d)^2\right].$$

Further improvement of the theory has recently been published [46], expanding the description to the influence of an external magnetic field up to 1 G, typically present in ion traps. For this field strength, the hyperfine interactions dominate over the interaction with the external field.

Theoretical transition frequencies

To determine the theoretical frequency of any particular hyperfine transition, three contributions have to be considered. The result of the solution of the Schrödinger equation is the non-relativistic and major contribution. For the $(\upsilon = 0, L = 0) \rightarrow (1,1)$ transition, this amounts to 58 604 301.269 MHz [40], whose error (11 kHz) is mainly caused by the uncertainties of the electron-proton and proton-deuteron mass ratio m_e/m_p and m_p/m_d. The second contribution of 750.87 MHz comes from the relativistic and QED effects $\left(\Delta E_{\alpha^2} + \ldots + \Delta E_{\alpha^6}\right)$ [45], with an estimated uncertainty of 21 kHz (theoretical approximations).

From summing up both contributions, the spin-independent frequency f_0 is obtained with an uncertainty of 24 kHz. According to [42], the hyperfine contribution for transition S0, for example, is -38.68 MHz. The uncertainties of the hyperfine contributions are less than 10 kHz [90], obtained from theoretical approximations.

$\Delta E_{nr}/h$	58 604 301.269(11)
$\Delta E_{\alpha^2}/h$	1 003.551
$\Delta E_{\alpha^3}/h$	- 250.978
$\Delta E_{\alpha^4}/h$	-1.812
$\Delta E_{\alpha^5}/h$	0.109(21)
f_0	58 605 052.139(24)

Table 2.2 Summary of the relativistic and radiative contributions to the $(\upsilon = 0,\ L = 0) \rightarrow (\upsilon' = 1,\ L' = 1)$ transition frequency in HD^+, in MHz.

2.2 Hyperfine states

For the calculation of the spin structure of a ro-vibrational state (υ, L) the state-dependent *effective spin Hamiltonian* H_{eff}^{tot} is used.

The spin splitting of the energy levels of HD^+ is evaluated in the basis set of states with definite values of the squared angular momenta $\boldsymbol{F}^2, \boldsymbol{S}^2$. The coupling scheme is given by (refer to Figure 2.3):

$$\boldsymbol{F} = \boldsymbol{I}_p + \boldsymbol{S}_e, \qquad \boldsymbol{S} = \boldsymbol{F} + \boldsymbol{I}_d, \qquad \boldsymbol{J} = \boldsymbol{L} + \boldsymbol{S}. \tag{2.19}$$

In zero magnetic field, the total angular momentum $\boldsymbol{J}$ and its projection J_z are good quantum numbers. An eigenstate of the hyperfine Hamiltonian is labeled by $|L\,F\,S\,J\,J_z\rangle$, where F and S are only approximate quantum numbers.

The corresponding eigenvalues $\Delta E^{\upsilon L n J_z}$ of H_{eff}^{tot} represent the energy levels of HD^+ with respect to the "*spinless*" energies $E^{\upsilon L}$, calculated as eigenvalues of $H^{NR} + V^{sh}$ (refer to Figure 2.2 and Table 2.3).

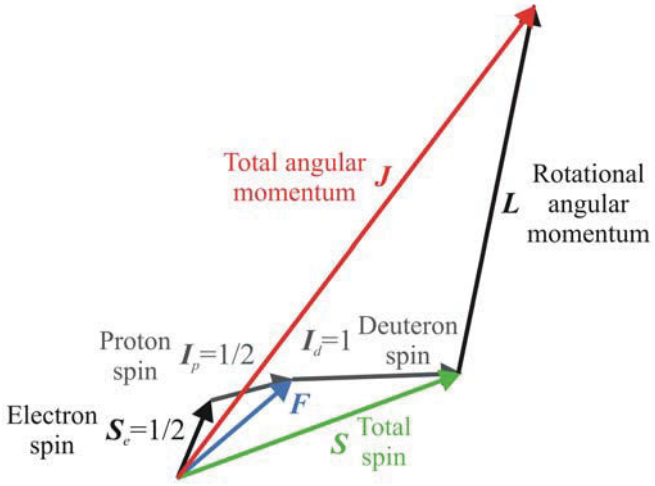

Figure 2.3 Simplified illustration of the spin and momenta of the HD^+ molecular ion in the centre-of-mass frame.

transition	{J,F,S} lower state	{J,F,S} upper state	frequency [MHz]	relative intensity
P4	{1,0,1}	{2,1,2}	1012.34	$1.93\cdot10^{-4}$
	{1,0,1}	{1,1,2}	969.53	$2.77\cdot10^{-4}$
	{1,0,1}	{2,1,1}	884.824	$7.71\cdot10^{-5}$
	{1,0,1}	{0,1,1}	867.358	$1.26\cdot10^{-4}$
	{1,0,1}	{1,1,0}	784.52	$5.34\cdot10^{-5}$
P3	{0,1,0}	{1,1,2}	174.743	$1.46\cdot10^{-3}$
P2	{1,1,1}	{1,1,2}	91.910	$2.84\cdot10^{-2}$
W4	{0,1,0}	{1,1,1}	61.415	$4.57\cdot10^{-2}$
S6	{1,0,1}	{0,0,1}	21.953	$1.43\cdot10^{-1}$
S5	{1,0,1}	{1,0,1}	17.854	$4.28\cdot10^{-1}$
S4	{1,0,1}	{2,0,1}	14.191	$7.14\cdot10^{-1}$
	{1,1,1}	{2,1,1}	7.204	$7.14\cdot10^{-1}$
	{2,1,2}	{2,1,2}	4.127	$7.14\cdot10^{-1}$
P1	{2,1,2}	{3,1,2}	2.607	1
S2	{1,1,1}	{0,1,1}	-10.262	$1.43\cdot10^{-1}$
S3	{0,1,0}	{1,1,0}	-10.267	$3.81\cdot10^{-1}$
S1	{1,1,1}	{1,1,1}	-21.417	$3.61\cdot10^{-1}$
S0	{2,1,2}	{1,1,2}	-38.686	$3.98\cdot10^{-1}$
	{1,1,1}	{1,1,0}	-93.10	$3.90\cdot10^{-2}$
W2	{2,1,2}	{1,1,1}	-152.013	$2.18\cdot10^{-2}$
W1	{2,1,2}	{1,1,0}	-223.696	$8.13\cdot10^{-3}$
	{0,1,0}	{1,0,1}	-776.933	$7.20\cdot10^{-5}$
	{1,1,1}	{0,0,1}	-855.668	$1.26\cdot10^{-4}$
	{1,1,1}	{1,0,1}	-859.766	$2.26\cdot10^{-5}$
	{1,1,1}	{2,0,1}	-863.429	$7.61\cdot10^{-5}$
	{2,1,2}	{1,0,1}	-990.362	$2.40\cdot10^{-4}$
	{2,1,2}	{2,0,1}	-994.025	$1.94\cdot10^{-4}$

Table 2.3 Table of the transition frequencies of the $(\upsilon = 0,\ L = 0\ ) \rightarrow (\upsilon' = 1,\ L' = 1)$ transition in HD^+. The frequencies are given with respect to the spinless frequency $f_0 = 58\ 605\ 052.139$ MHz.

The transitions and their relative intensity are illustrated in the energy diagram of the hyperfine states of HD^+ in Figure 2.4 and the stick spectrum in Figure 2.5 respectively.

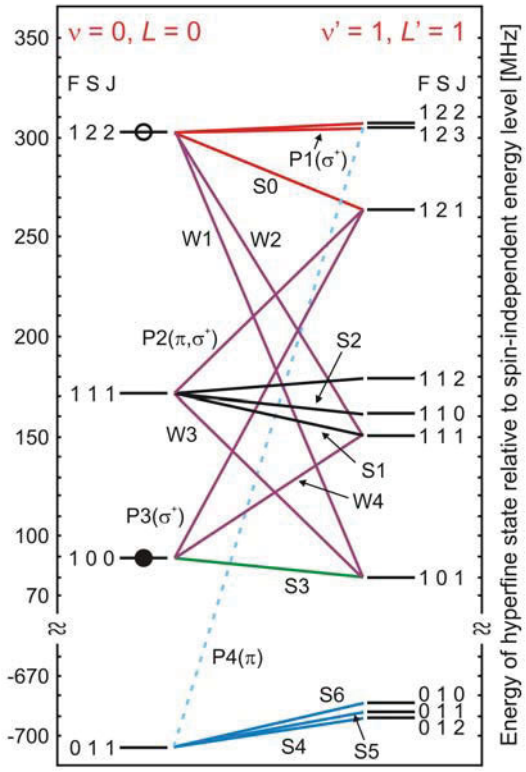

Figure 2.4 Energy diagram of the hyperfine states of the HD^+ molecular ion and the main electric dipole transitions in zero magnetic field. Transitions not changing the quantum numbers F, S are relatively strong and marked in red, black, green and blue. Transitions changing one or two of them are indicated in purple

The structure of the $(\upsilon = 0,\ L = 0) \rightarrow (\upsilon' = 1,\ L' = 1)$ one-photon excitation spectrum, relevant to this work, can be calculated [46].

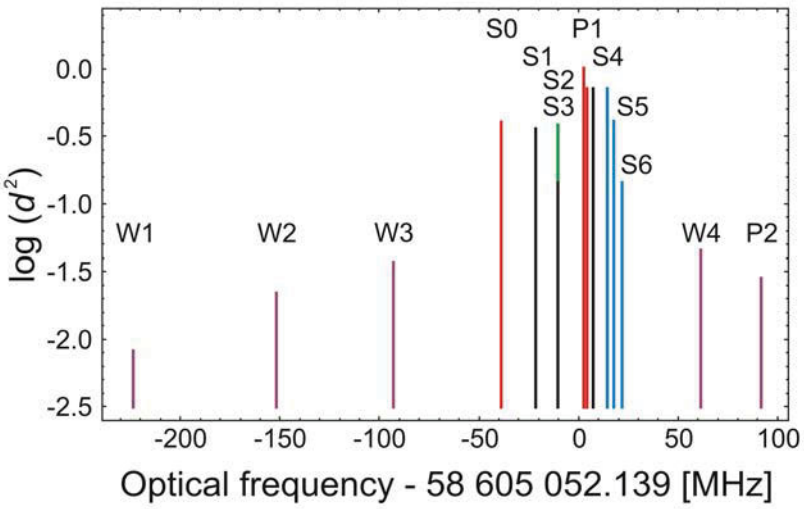

Figure 2.5 Stick spectrum of the $(\upsilon = 0,\ L = 0) \rightarrow (\upsilon' = 1,\ L' = 1)$ transition in zero magnetic field. The values of the squared transition moment d^2 are normalized to the strongest transition for illustrative purposes.

2.3 Zeeman structure of the hyperfine spectrum

In order to perform precise measurements of the transition frequencies and thereby improve values and limits, the contribution of many systematic effects have to be taken into consideration. The contribution of the Zeeman-effect, caused by background or applied magnetic fields, is one of the effects to be discussed.
Typically, a small quantization field can be applied to the experimental apparatus in order to split the Zeeman components. In addition, unwanted time-dependent magnetic fields may exist due to alternating currents flowing in the ion trap.
Starting from typical magnetic field strengths in ion traps, field ranges up to 1 G (relevant to this work) should be taken into consideration for the following. For these values, the hyperfine interactions dominate over the interaction with the external field. Thus, a first order perturbative calculation of the Zeeman energies with respect to the hyperfine states in section 2.2 can be performed.

The consideration of the external magnetic field yields in an additional term V^{mag} in equation (2.14):

$$H = H^{NR} + V^{sh} + V^{spin} + V^{mag}. \tag{2.20}$$

In the leading order approximation, the external magnetic field interaction term V^{mag} is given by:

$$V^{mag} = -\boldsymbol{m}\cdot\boldsymbol{B}, \qquad \boldsymbol{m} = \sum_i \frac{eZ_i}{2M_i c}\left(\boldsymbol{L}_i + \frac{\mu_i}{s_i}\boldsymbol{S}_i\right). \tag{2.21}$$

The summation is over the HD^+ constituents $(i = p,d,e)$ (Note: $\boldsymbol{I}_d \equiv \boldsymbol{S}_d, \boldsymbol{I}_p \equiv \boldsymbol{S}_p$), M_i, Z_i and μ_i are the mass, electric charge (in unit e) and magnetic moment in units $e\hbar/2M_i c$ of the particles. s_i describes the size of the spin ($s_{p,e} = 1/2$ for the proton and electron, $s_d = 1$ for the deuteron) and $\boldsymbol{B}$ is the external magnetic field.

Compared to the effective Hamiltonian H_{eff}^{hfs} obtained from (2.18), H_{eff}^{tot} contains additional terms, originating from V^{mag}. H_{eff}^{tot} is obtained by averaging $V^{spin} + V^{mag}$ over the spatial degrees of freedom:

$$H_{eff}^{tot} = H_{eff}^{hfs} + E_{10}(\boldsymbol{L}\cdot\boldsymbol{B}) + E_{11}(\boldsymbol{I}_p\cdot\boldsymbol{B}) + E_{12}(\boldsymbol{I}_d\cdot\boldsymbol{B}) + E_{13}(\boldsymbol{S}_e\cdot\boldsymbol{B}). \tag{2.22}$$

According to [46], the coefficients E_{11}- E_{13} in the adopted approximation following (2.21) are given in terms of masses and magnetic moments by:

$$E_{11} = -\frac{e\mu_p}{M_p c} = -4.2577 \text{ kHz G}^{-1}, \qquad E_{12} = -\frac{e\mu_d}{2M_d c} = -0.6536 \text{ kHz G}^{-1}, \qquad E_{13} = \frac{e\mu_e}{M_e c} = 2.8025 \text{ kHz G}^{-1}. \tag{2.23}$$

The value of the coefficient E_{10} is calculated using the *variational nonrelativistic wavefunction* of HD^+ of [40][46]:

$$E_{10} = -\mu_B \sum_i \frac{Z_i M_e}{M_i} \frac{\langle \upsilon L \| \boldsymbol{L}_i \| \upsilon L \rangle}{\sqrt{L(L+1)(2L+1)}}. \tag{2.24}$$

According to the coupling scheme (2.19) J_z, the z-axis projection of $\boldsymbol{J}$, is the only exact quantum number for the nonzero field $\boldsymbol{B}$, except for the so called "*stretched states*" with $F = S_p + S_e = 1$, $S = F + S_d = 2$, $J = S + L = L + 2$ and $J_z = \pm J$, for which F, S and J are also exact quantum numbers. As shown by Bakalov et al. [46], the hyperfine states of HD^+ are split into sub-levels, distinguished by means of the quantum number J_z. Considering low magnetic fields, the dependence of the eigenvalues $\Delta E^{\upsilon L n J_z}$ of H_{eff}^{tot} on the magnetic field B may be approximated with the quadratic form [46]

$$\left(\Delta E^{\upsilon L n J_z}(B) - \Delta E^{\upsilon L n J_z}(0)\right)/h \approx t^{\upsilon L n} \cdot J_z \cdot B + \left(q^{\upsilon L n} + r^{\upsilon L n} \cdot J_z^2\right) \cdot B^2. \tag{2.25}$$

This approximation reproduces the exact values with a relative error below 10^{-6} for $B < 1$ G except for the Zeeman components of the $L = 1$ states with $F = 1$, $S = 2$, $J = 2, 3$ and very close hyperfine energies, for which the third order contribution in B cannot be neglected. The corresponding values for $t^{\upsilon L n}$, $q^{\upsilon L n}$ and $r^{\upsilon L n}$ for the lower ro-vibrational states with $L \le 4$ and $\upsilon \le 4$ are given in table II of [46]. Following (2.25), the term quadratic in B is of main interest for states with $J_z = 0$ and gives an observable contribution for the remaining states for $B > 0.1$ G. A rearrangement of the spectrum can be observed for $B > 50$ G as the spectrum acquires a doublet form caused by the domination in H_{eff}^{tot} (2.22) of the term $E_{13}(\boldsymbol{S}_e \cdot \boldsymbol{B})$, while the small splitting is due to the $E_{11}(\boldsymbol{I}_p \cdot \boldsymbol{B})$ term. The dependence on B of the energy levels of the hyperfine states is illustrated in Figure 2.6 for the ro-vibrational ground state.

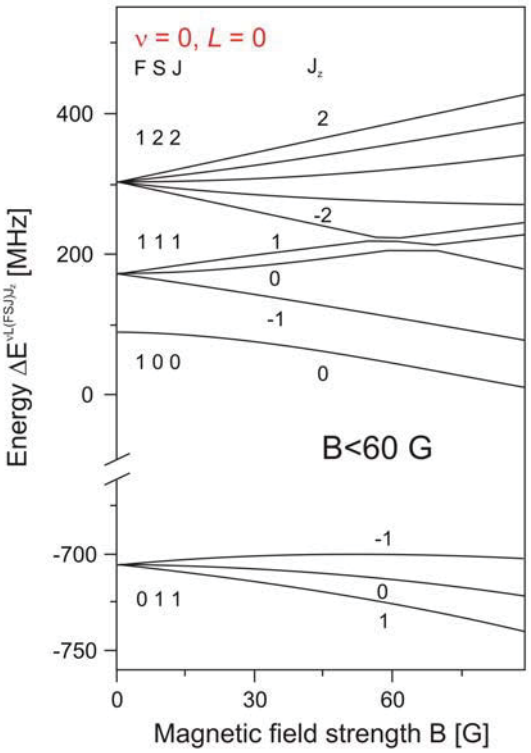

Figure 2.6 Energies $\Delta E^{\upsilon L(FSJ)J_z}$ of the hyperfine levels of the ground ro-vibrational level $(\upsilon = 0,\ L = 0)$ of HD^+ as a function of the magnetic field for B. The two "stretched states" are the top and bottom sub-levels at ~ 300 MHz $(J_z = \pm J = \pm 2)$ [46].

In case of an existing magnetic field the excitation spectrum can include additional Zeeman components. In this work, the resolution is limited to resolve discrete hyperfine lines but not the Zeeman subcomponents. As an example, for line S0, the shift of the line center due to unresolved lines is estimated to be less than 10 kHz.

2.4 Electric dipole transitions in HD^+

Einstein coefficients

To describe transitions in a molecule between two energy levels n and m with $E_n > E_m$ one has to distinguish between different processes. On the one hand, a transition can be induced by a photon of frequency $\nu_{nm} = (E_n - E_m)/h$ leading to absorption or stimulated emission. On the other hand, $n \to m$ transitions can occur spontaneously under emission of a photon of frequency ν_{nm}. The *Einstein coefficients* A_{nm} and B_{nm} describe the probability of these processes to occur. The probability per second for a molecule to undergo a spontaneous decay is given by A_{nm}. The other Einstein coefficient B_{nm} represents the probability per second of a molecule participating in an absorption process between levels. This process is proportional to the spectral energy density of the radiation causing the process. B_{nm} represents the proportionality constant. In case of the stimulated emission B_{mn} can be used in a similar way, whereas $B_{nm} = B_{mn}$ can be set as long as the levels n and m have equal statistical weights. The *Einstein coefficients* between degenerate states are given in SI units in [47]:

$$A_{n,m} = \frac{\hbar\omega^3}{\pi^2 c^3} B_{n,m} \text{ and } B_{n,m} = \frac{\pi \left|\vec{D}_{n,m}\right|^2}{3 g_n \varepsilon_0 \hbar^2}, \tag{2.26}$$

with the *transition dipole matrix element* of a degenerate state

$$\vec{D}_{n_\xi, m_\mu} = \int \psi^*_{n_\xi} \vec{p} \psi_{m_\mu} dr_e dr_c \tag{2.27}$$

and the wave functions ψ_{n_ξ} and ψ_{m_μ} of the respective states. The dipole matrix element $\vec{D}_{n_\xi, m_\mu}$ represents a combined nuclear-electronic transition moment for electronic transitions. Therefore, dipole operator $\vec{p}$ can be split into an electronic and a nuclear part $\vec{p} = \vec{p}_e + \vec{p}_c$.
In the Born-Oppenheimer approximation, the wave function is replaced by $\psi_j = \psi_{j,e}\chi_{j,c}$, where $\psi_{j,e}$ is the electronic wave function and $\chi_{j,c}$ is the nuclear wave function. This leads to another form of equation (2.27):

$$\vec{D}_{n_\xi, m_\mu} = \int \chi^*_{n_\xi, c} \left[\int \psi^*_{n_\xi, e} \vec{p}_e \psi_{m_\mu, e} dr_e \right] \chi_{m_\xi, c} dr_c + \int \chi^*_{n_\xi, c} \vec{p}_c \left[\int \psi^*_{n_\xi, e} \psi_{m_\mu, e} dr_e \right] \chi_{m_\mu, c} dr_c. \tag{2.28}$$

In case of pure ro-vibrational transitions $\left(\psi_{n_\xi, e} = \psi_{m_\mu, e}\right)$, the first term vanishes, whereas the second term vanishes for $\psi_{n_\xi, e} \neq \psi_{m_\mu, e}$. The latter is the case for changes of the electronic state or of the nuclear position.

According to [47], the total transition dipole moment for degenerate states is given by:

$$\left|\vec{D}_{n,m}\right|^2 = \sum_{\xi,\mu} \left|\vec{D}_{n_\xi, m_\mu}\right|^2. \tag{2.29}$$

The variables g_n represent the degeneracy factor. **Note:** In the equations (2.26) and (2.29), the frequency ν_{nm} is given in [Hz] and the dipole matrix element is in SI units as well.
The Einstein coefficients can be calculated once the wave functions and their corresponding energies have been obtained from the Schrödinger equation.

For example, according to the work of *Colbourn and Bunker* [49], the value of the total transition dipole matrix element $D_{(1,1)\to(0,2)}$ for the transition $A_{(1,1)\to(0,2)}$ is determined to be:

$$D_{(1,1)\to(0,2)} = 0.07799 \text{ [Debye]}, \quad 1 \text{ Debye} = 3.3564 \cdot 10^{-30} \text{ Cm} \approx 0.208 \text{ eÅ}. \tag{2.30}$$

Following the work of Amitay et al. [93] and relying on the values of [49], the Einstein coefficient, e.g. $A_{(1,1)\to(0,2)}$ is given by:

$$\begin{aligned} A_{(1,1)\to(0,2)} &= 7.2356 \cdot 10^{-6} \left(\Delta E_{(1,1)\to(0,2)} \left[\text{cm}^{-1}\right]\right)^3 \left|D_{(1,1)\to(0,2)} \left[\text{e}10^{-10}\text{m}\right]\right|^2 \\ &= 7.2356 \cdot 10^{-6} \left(1823.545\right)^3 \left|0.0779 \cdot 0.208\right|^2 \left|\left[\text{e}10^{-10}\text{m}\right]\right|^2 \\ &\approx 12 \text{ s}^{-1}. \end{aligned} \tag{2.31}$$

The radiative lifetime $\tau_{v'L'}$ of a ro-vibrational state $v'L'$ follows as

$$\tau_{v'L'} = \frac{1}{A_{v'L'}}, \tag{2.32}$$

where $A_{v'L'}$ is the total Einstein coefficient, which in the present case is the sum over all probabilities for spontaneous transitions between any two rovibrational states, in the ground electronic state. The lifetimes τ_{vL} for some selected ro-vibrational levels in HD^+ are given in Table 2.4.The transition probabilities $A_{(vL)\to(v'L')}$ and spontaneous emission lifetimes τ_{vL} of some transitions relevant for spectroscopy in this work are illustrated in Figure 2.7.

	$L=0$	$L=1$	$L=2$	$L=3$	$L=4$
$v=0$		149.259	15.65	4.371	1.803
$v=1$	0.055	0.055	0.056	0.057	0.060

Table 2.4 Lifetimes τ_{vL} in seconds for some selected ro-vibrational levels in HD^+.

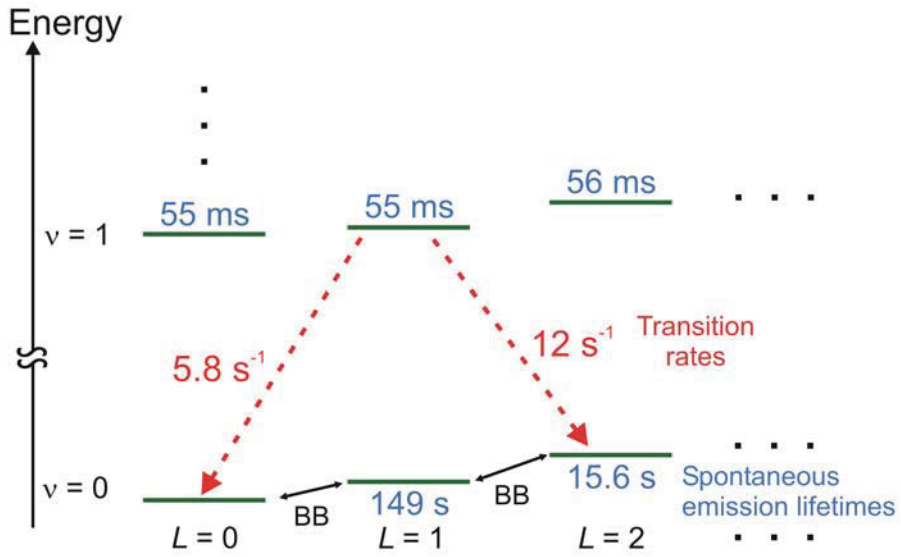

Figure 2.7 Transition probabilities $A_{(vL)\to(v'L')}$ and spontaneous emission lifetimes τ_{vL} of some transitions relevant for spectroscopy in this work. In addition, the black-body-induced excitation and de-excitation is indicated (BB).

Transition linewidth (FWHM)

The natural linewidth (FWHM) depends on the lifetimes of the corresponding states

$$\delta\nu = \frac{1}{2\pi}\left(\frac{1}{\tau_1}+\frac{1}{\tau_2}\right) \tag{2.33}$$

and is described by a Lorentz profile. Due to the long lifetimes of the ground-ro-vibrational levels, this linewidth is very small. Therefore, the Doppler broadening dominates. Its Doppler width is given by:

$$\delta\nu_D = \sqrt{8\ln 2\ k_B}\,\frac{\nu_{12}}{c}\sqrt{\frac{T}{m}}. \qquad \textbf{(2.34)}$$

As can be seen, the dominant dependence is on the resonance frequency ν_{12}, whereas the dependence on temperature and mass of the molecule is weaker. Due to thermal distribution of the molecules, the Doppler-profile is given by:

$$g_D(\nu) = g_0 e^{-4\ln 2\frac{(\nu-\nu_0)^2}{\delta\nu_D^2}},\ \text{with}\ g_0 = \frac{1}{\delta\nu_D}\sqrt{\frac{4\ln 2}{\pi}}. \qquad \textbf{(2.35)}$$

For HD^+ with m= 3 AME, the Doppler width is:

$$\delta\nu_D = 123{,}97\frac{\sqrt{T}}{\lambda_{12}}. \qquad \textbf{(2.36)}$$

The Doppler width at T=300 K and λ_{12}=5.115 µm is $\delta\nu \approx 0.42$ GHz and decreases to $\delta\nu \approx 2.4$ MHz at 0.01 K.

Excitation rates

According the derivation in [48], the excitation rate R_{12} from a state 1 to a state 2 per molecule and per time by a laser with the intensity $I_L(\nu)$ is given by:

$$R_{12}(\nu) = \sigma(\nu)\frac{I_L(\nu)}{h\nu} = \frac{1}{4}\frac{g_2}{g_1}\left(\frac{c}{\nu_{12}}\right)^2 A_{21} g_D(\nu)\frac{I_L(\nu)}{h\nu}. \qquad \textbf{(2.37)}$$

$\sigma(\nu)$ is the absorption cross section and ν_{12} is the resonance frequency of the transition.
The variables g_1, g_2 represent the degeneracy factors of the two levels. As mentioned in chapter 2.2, in a diatomic molecule like HD^+, a rotational level of quantum number J is in general (2J+1)-fold degenerate. Therefore, equation (2.37) can be expressed as:

$$R_{12}(\nu) = \frac{1}{4}\frac{2J_2+1}{2J_1+1}\left(\frac{c}{\nu_{12}}\right)^2 A_{21}\frac{1}{\delta\nu_D}\sqrt{\frac{4\ln 2}{\pi}}\frac{I_L(\nu)}{h\nu}. \qquad \textbf{(2.38)}$$

Note that this equation is only valid when the laser linewidth $\delta\nu_L$ is much smaller than the Doppler width $\delta\nu_D$ of the transition.

The excitation rate R_{12} for the transitions $(0,0)\rightarrow(1,1)$ with $A_{(1,1)\rightarrow(0,0)} \approx 5.8\ \text{s}^{-1}$ (e. g. lines S0, W4, P2, refer to Table 2.3), $\delta\nu \approx 2.4$ MHz at 0.01 K with typical laser intensities in the range of 0.09 - 2.31 µW and a beam diameter of 3 mm in the trap center is $R_{12} \approx 2.9 - 15.6\ \text{s}^{-1}$.

For given laser intensities, the internal state dynamics of the HD^+ molecule can be modelled by a set of rate equations. The following illustration shows a typical rate equation simulation of the ro-vibrational ground level $(\upsilon = 0,\ L = 0,\ 1,\ ...,\ 5)$.

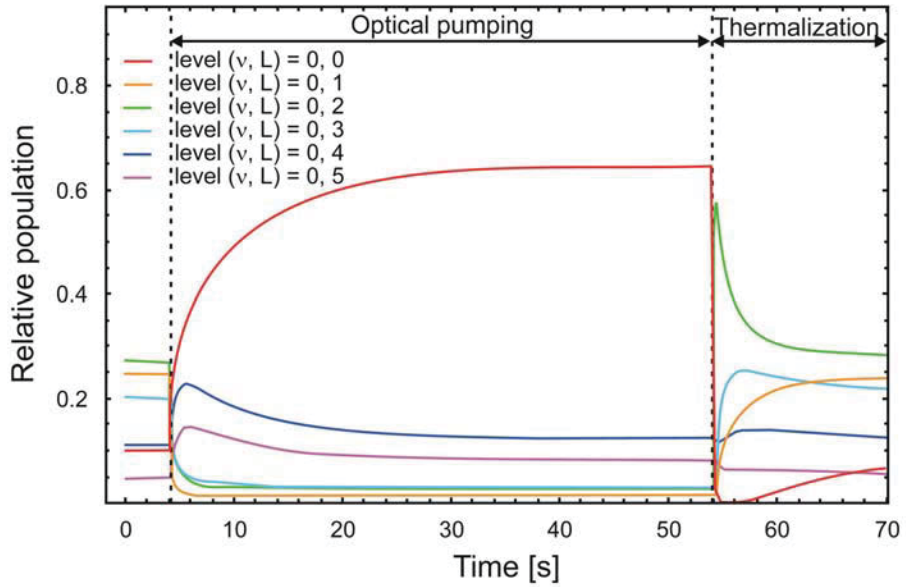

Figure 2.8 Illustration of a rate equation simulation for the optical pumping scheme (see chapter 5.2). The time evolution of the fractional rotational state populations in the vibrational ground state is shown for simultaneous optical pumping with the different pumping lasers (except $\lambda_p = 5484$ nm), described in chapter 3.4 and chapter 5.2. In addition, the thermalization with the T=300 K blackbody radiation after the optical pumping fields have been turned off is shown.

3 Trapping and cooling of ions

Storage and cooling of charged particles can be realized in ion traps placed in ultra-high vacuum chambers, providing a well-defined and nearly collisionless confined volume. In this work, a *linear quadrupole / Paul trap* has been used, which enables, due to its large potential depths of several eV, the storage and cooling of particles within the same trap.
Although *Doppler laser cooling* is an effective tool for the reduction of the translational energy of trapped ions, it can only be applied to certain species of ions. It is restricted to ions with a suitable electron configuration, providing closed optical transitions.
Despite this fact, an elegant way to extend this method is *sympathetic cooling*. Here, non-laser coolable ions, trapped simultaneously together with laser-coolable ones are cooled by Coulomb interaction between the particles.
For the precision spectroscopy of ultracold HD^+ in this work, laser cooled Be^+ ions trapped in a linear Paul trap serve as the cooling medium.

3.1 The linear Paul trap

The accumulation of equally charged particles near an electric potential minimum in the trapping region can be understood as the basic principle of ion traps. Following *Earnshaw's theorem* [69], a three-dimensional extremum of a potential $\Phi(x,y,z)$ violates the *Laplace equation*

$$\Delta\Phi = \frac{\partial^2\Phi}{\partial x^2} + \frac{\partial^2\Phi}{\partial y^2} + \frac{\partial^2\Phi}{\partial z^2} = 0. \qquad \textbf{(3.1)}$$

Consider a harmonic potential such as $\Phi = \alpha x^2 + \beta y^2 + \gamma z^2$. The Laplace equation yields $\alpha + \beta + \gamma = 0$ and reveals that the factors α, β, γ cannot satisfy the binding condition $\alpha < 0, \beta < 0, \gamma < 0$. This example demonstrates that in at least one spatial direction the potential will be non-binding.

Storing charged particles can be achieved by several different approaches [70]. In comparison to neutral particles, it is obvious that ions interact more strongly with electromagnetic fields. Therefore using combinations of static electromagnetic-fields (*Penning trap*) or the combination of static and alternating electric fields (*Paul trap* or *r. f. quadrupole trap*) enable their storage. The magnetic fields used in Penning traps are rather large and might limit the spectral resolution due to splitting and broadening of the spectral lines.
In this work, a linear Paul trap, consisting of three independent quadrupole-massfilters, two of them used as *endcap electrodes* on both sides, has been implemented [71]. This is advantageous, because with this trap geometry, an effective potential minimum in the trap center along the whole symmetry axis can be achieved. It enables the storage of more ions than in the 3D hyperbolic Paul trap with ring electrodes and endcaps, in which the ions are

only locally stored in the trap center. In addition, with this configuration good optical access can be obtained, which is very desirable for spectroscopy.

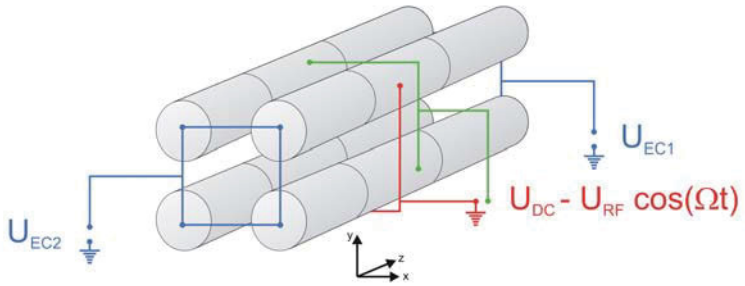

Figure 3.1 Schematic illustration of the linear Paul trap and the corresponding electric wiring.

3.1.1 The quadrupole mass filter – the radial confinement –

An ideal quadrupole mass filter consists of four hyperbolic electrodes arranged in a quadrupole configuration. For simplicity, they are often replaced in experiments by cylindrical electrodes, showing very similar performance near the trap center.

A pair of opposing electrodes is electrically connected and supplied with a voltage $\phi_0 = U_{DC} - U_{RF}\cos(\Omega t)$, generating the *quadrupole saddle potential*:

$$\phi(x,y,t) = \frac{U_{DC} - U_{RF}\cos(\Omega t)}{2r_0^2}\cdot(x^2 - y^2). \qquad (3.2)$$

Here, U_{DC} and U_{RF} are the amplitudes of the static and the alternating electric field, with the angular frequency Ω of the r. f. field. $r_0 = \sqrt{x_0^2 + y_0^2}$ is the distance from the surface of the electrodes to the trap center.
The equations of motion for two-dimensional motion of a particle of charge Q and mass m are given by:

$$\ddot{x} + \frac{Q}{mr_0^2}\left(U_{DC} - U_{RF}\cdot\cos(\Omega t)\right)\cdot x = 0, \qquad (3.3)$$

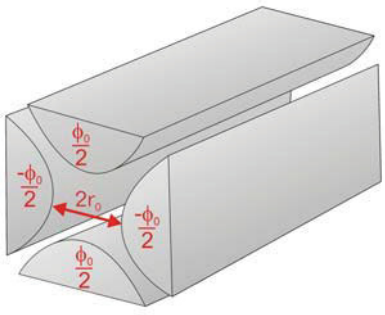

Figure 3.2 Schematic illustration of the linear quadrupole mass-filter.

$$\ddot{y} - \frac{Q}{mr_0^2}\left(U_{DC} - U_{RF}\cdot\cos(\Omega t)\right)\cdot y = 0. \qquad \textbf{(3.4)}$$

Using the following dimensionless (stability) parameters,

$$a = a_x = -a_y = \frac{4QU_{DC}}{mr_0^2\Omega^2}\ , \qquad q = q_x = -q_y = \frac{4QU_{RF}}{mr_0^2\Omega^2}\ , \qquad \tau = \frac{1}{2}\Omega t\ , \qquad \textbf{(3.5)}$$

the equations can be transformed into the *Mathieu differential equations*:

$$\frac{\partial^2 u}{\partial \tau^2} + \left(a_u - 2q\cos(2\tau)\right)u = 0 \ \text{ with } u = x, y. \qquad \textbf{(3.6)}$$

Stable trajectories of this equation of motion can be found only for certain values of the dimensionless parameters a, q. For those stable trajectories, the amplitudes in the x and y-directions are limited and therefore smaller than r_0. In case of unstable solutions, the ions come into contact with the electrodes and are therefore lost.

Following the above stability diagram, this means that the (a,q)-pairs of all ions lie on a straight line with slope $a/q = 2U_{DC}/U_{RF}$ for fixed parameters r_0, Ω, U_{DC} and U_{RF}.
The masses m_1 and m_2 refer the intersections of this line with the radial stability region and express the minimum and maximum mass which are radially confined. Hence, the quadrupole mass filter acts as a band-pass mass filter, trapping only ions with $m_2 \le m \le m_1$.

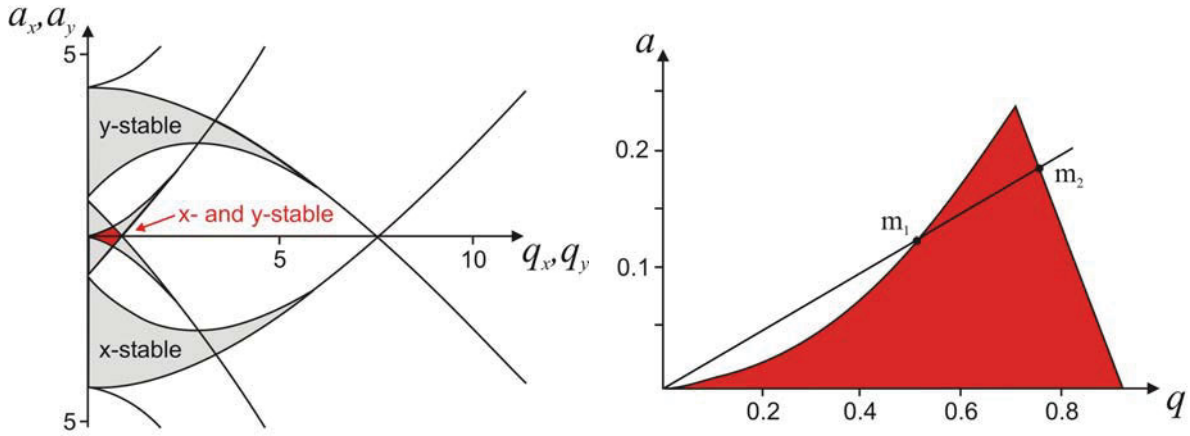

Figure 3.3 Stability diagram of the quadrupole mass-filter [72]
left: Regions allowing stable motion in x- or y-direction are shown in grey. The overlapping region, shown in red, illustrates stable motion in the xy-plane.
right: Magnified (positive) stable region in the xy-plane.

3.1.2 The axial confinement

For the axial entrapment, additional static *endcap* potentials U_{EC1} and U_{EC2} are applied to electrodes at the ends of each quadrupole electrode. These electrodes form in principle another quadrupole electrode configuration described above, but possess the same potentials $U_{EC1}=U_{EC2}$ respectively (see Figure 3.1).
The resulting axial potential close to the trap axis can be expressed as [73]:

$$\phi_z = \kappa U_{EC} z^2. \tag{3.7}$$

The coefficient κ is a trap constant ($\kappa \approx 3\times10^{-3}$ mm^{-2} for our traps, [74]), determined by the geometry and the distance of the endcap electrodes. Due to a defocusing effect of the endcap potentials on the radial confinement, a certain weakening has to be accepted. For most applications and also for the trap used in this work, $U_{DC}=0$ is convenient. The total two-dimensional trap potential then follows as:

$$\phi(x,y,t) = -\frac{U_{RF}\cos(\Omega t)}{2r_0^2}\left(x^2-y^2\right) - \frac{1}{2}\kappa U_{EC}\left(x^2+y^2\right). \tag{3.8}$$

Transforming the equation again into the *Mathieu differential equations* leads to:

$$\frac{\partial^2 u}{\partial \tau^2} + \left(a_z - 2q_u\cos(2\tau)\right)u = 0 \text{ with } u = x, y. \tag{3.9}$$

The corresponding dimensionless (stability) parameters slightly differ from those above:

$$a_z = -\frac{4\kappa Q U_{EC}}{m\Omega^2}\ , \qquad q = q_x = -q_y = \frac{2QU_{RF}}{mr_0^2\Omega^2}\ , \qquad \tau = \frac{1}{2}\Omega t\ . \tag{3.10}$$

Hence, the stability diagram differs slightly from that of the quadrupole mass filter above. Stably trapping a positively charged ion in the z-direction can only be achieved for $a_z < 0$, i.e. by applying a positive voltage U_{EC} to the endcap electrodes (Figure 3.4). In addition, the trapping range exceeds (arbitrary) large *q*-values, meaning (arbitrary) low masses of the ions, as long the endcap voltage U_{EC} and therefore the corresponding value of a_z can be maintained.

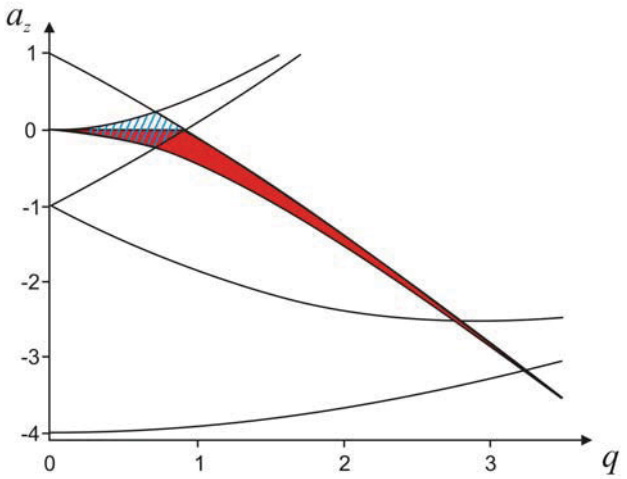

Figure 3.4 Stability diagram of the linear quadrupole trap. The first radial trapping region for positively charged ions is illustrated in red. For comparison, the radial trapping region of the quadrupole mass-filter is presented in blue hatching [75].

3.1.3 Ion motion in a linear Paul trap

The radial motion of an ion in a linear Paul trap can be expressed by the solutions of the Mathieu differential equations (3.9) for $-a_z, q \ll 1$:

$$u(t) = u_{\max}\left(1+\frac{q}{2}\cos(\Omega t)\right)\cos\left(\omega_{\mathrm{sec},r}t\right) \text{ with } u = x, y. \tag{3.11}$$

Here, $\omega_{\mathrm{sec},r}$ is called the *radial secular frequency*:

$$\omega_{\mathrm{sec},r} = \frac{\Omega}{2}\sqrt{\frac{q^2}{2}+a_z}\,. \tag{3.12}$$

Dependent on a_z, the radial secular frequency is decreased by the static field of the endcap electrodes. This so-called *secular motion* with low frequency $\omega_{\mathrm{sec},r} \ll \Omega$ and amplitude $u_{\max}$ described in (3.11), is the **dominant** motion for an ion in a linear Paul trap.

An additional motion, superposed on it, is called *micromotion*. This fast fluctuating motion is oscillatory at the trap r. f. frequency Ω and has a small amplitude (as long as $q \ll 1$), which is proportional to the distance to the trap axis. Hence, the secular motion can be interpreted as the time average of this combined motion and can be expressed as a motion in a time-independent harmonic *pseudo potential* Φ_{ps} with the oscillation frequency $\omega_{\mathrm{sec},r}$:

$$\Phi_{ps}(x,y) = \frac{1}{8}qU_{RF}\frac{x^2+y^2}{r_0^2} - \frac{1}{2}\kappa U_{EC}\left(x^2+y^2\right). \tag{3.13}$$

In three dimensions, this time independent pseudopotential for the linear quadrupole trap can be written as

$$\Phi_{ps}(x,y,z) = \frac{1}{2}\frac{m}{Q}\omega_{\mathrm{sec},r}^2\left(x^2+y^2\right) + \frac{1}{2}\frac{m}{Q}\omega_{\mathrm{sec},z}^2 z^2, \qquad \textbf{(3.14)}$$

with the *axial secular frequency*

$$\omega_{\mathrm{sec},z} = \frac{\Omega}{2}\sqrt{-2a_z}. \qquad \textbf{(3.15)}$$

Trapped ions will be lost when they reach the electrodes. From (3.13) the depth of the pseudopotential in the trap center ($z = 0$) can be estimated:

$$\Phi_0 = \Phi(r_0) = \frac{QU_{RF}}{8}q. \qquad \textbf{(3.16)}$$

Ions with kinetic energies higher than Φ_0 (in general several eV) will be lost.

Note: Expressions obtained for the radial secular frequency $\omega_{\mathrm{sec},r}$ and the axial secular frequency $\omega_{\mathrm{sec},z}$ are valid in this strict form only for a single ion confined in the trap. For more ions trapped simultaneously, contributions of space charge effects and coupling effects between different ion species, leading to sometimes significantly shifted resonance frequencies, have to be considered [76].

R. F. heating process

Taking into consideration that ions collide with residual gas particles or other trapped ions, a transfer of kinetic energy from the ions' micromotion to the secular motion takes place. Due to these disturbances, as well as electric noise, their motion can get out of phase with the trap r. f. field, gaining new kinetic energy in form of micro motion which is eventually transferred to secular motion. As a consequence, an irreversible energy transfer to the secular motion takes place, increasing the kinetic energy of the ions. Under certain conditions, the kinetic energy can be understood as an indicator of the ions' temperature (*secular temperature*). Hence, the described energy transfer from the micro motion to the secular motion is called *r. f. heating*. Various other factors such as the trap parameters, the number of trapped ions and the ion temperature itself influence the r. f. heating rate. Molecular dynamics (MD) simulations are necessary to investigate the r. f. heating rates [78].
Linear quadrupole traps have the advantage of a relative large trap volume close to the trap axis, where the ions' micro motion is small and thus the r. f. heating is negligible. The preparation of huge ion crystals of more than 10^5 ions has been demonstrated [79].

3.2 Cooling of trapped ions

3.2.1 Cooling techniques

Laser cooling

The technique of laser cooling, proposed independently in 1975 by Hänsch and Schawlow [80] and Wineland and Dehmelt [81], has become an essential and efficient way of removing the motional energy of ions via their interactions with laser light.

The basic principle of laser cooling (see Figure 3.5, a detailed treatment follows in Chapter 3.2.2) is the deceleration of particles using the transfer of momentum that occurs when an atom absorbs a photon. Due to a very small momentum transfer, the excited atoms need to return immediately to the ground state by emitting a photon to continue deceleration by repeated absorption. Thus the number of atom or ion species with a suitable electron configuration which fulfill the need for closed optical transitions are limited. Molecules usually possess numerous rovibrational levels, sometimes with long lifetimes or radiationless relaxation, making them unsuitable for the application of laser cooling. The procedure of sympathetic cooling however opens a way of indirectly laser cooling the favored molecule species.

Sympathetic cooling

In the procedure of sympathetic cooling one takes advantage of transferring kinetic energy between two or more different ion species trapped together in an ion trap. One species, laser-cooled, will receive kinetic energy from another ion species in the trap by elastic Coulomb collisions and dissipate it via the laser-cooling. As a result, the non-laser cooled ion will loose energy and participates indirectly in the laser-cooling and will be cooled down to the thermal equilibrium state between both ion species.

In contrast to other cooling techniques (i.e. buffer-gas cooling) sympathetic cooling can be applied to a large variety of ions, atomic or molecular ones, which can be trapped together with a laser-cooled species in an ion trap. This applies especially for molecules, which are not suitable for laser-cooling techniques due to lack of closed optical transitions or matching laser sources. Sympathetic cooling can be used independently of the particle's electric or magnetic moments, making it applicable for a large number of molecular species. While the masses of the interacting species are a restricting factor in buffer-gas cooling, sympathetic cooling is applicable to ions with higher, as well as lower mass. As shown in molecular dynamics (MD) simulations [82], the efficiency of sympathetic cooling does not significantly depend on the mass ratio between laser cooled and sympathetic cooled ion species but much more on their mass-to-charge ratios.

As will be shown in chapter 3.3, the mass-to-charge ratio causes a radial separation of the interacting ion species in the quadrupole ion trap. The more spatially close an ion species is to the laser-cooled ions, the more efficient is the sympathetic cooling due to stronger Coulomb interaction.

The experimental employment of sympathetic cooling in our group concentrated on $^{9}Be^{+}$ used for the mass range from 1-200 amu and $^{138}Ba^{+}$ up to 12400 amu.

3.2.2 Fundamentals of Doppler laser cooling

The principle of laser cooling is based on momentum conservation, whereby the free particle experiences a recoil during scattering of a photon, and shifting of the particle's resonance frequency due to the Doppler-effect.

Assume an atom with a two level system in ground state $|g\rangle$ and transition frequency ω_A (see Figure 3.5).

If the atom is moving with a velocity $\vec{v}$ against a slightly red-detuned laser field with a frequency ω_L (i.e. $\omega_L < \omega_A$) and the wave vector $\vec{k}_L$, the laser frequency appears to be increased by the Doppler shift $\vec{k}_L \cdot \vec{v}$. Resonance will occur for $\omega_A - \vec{k}_L \cdot \vec{v} = \omega_L$. At the moment of absorption, the atom receives the photon's momentum $\hbar\vec{k}_L$ in the direction of the laser beam and is thus decelerated. On the contrary, an atom moving in the same direction as the irradiated laser field will not absorb a photon because of a non-resonant transition frequency and thus will not change its momentum. The recoil due to spontaneous emission of a photon can be neglected, because spontaneous emission is isotropic in space, so that these recoils cancel out over many absorption and emission cycles.

Using a semi-classical model [83], in which the atom is treated quantum-mechanically as a two level system and its motion classically, the Doppler laser cooling can be quantitatively described. According to the detailed treatment in [84][85], the main results are presented in the following.

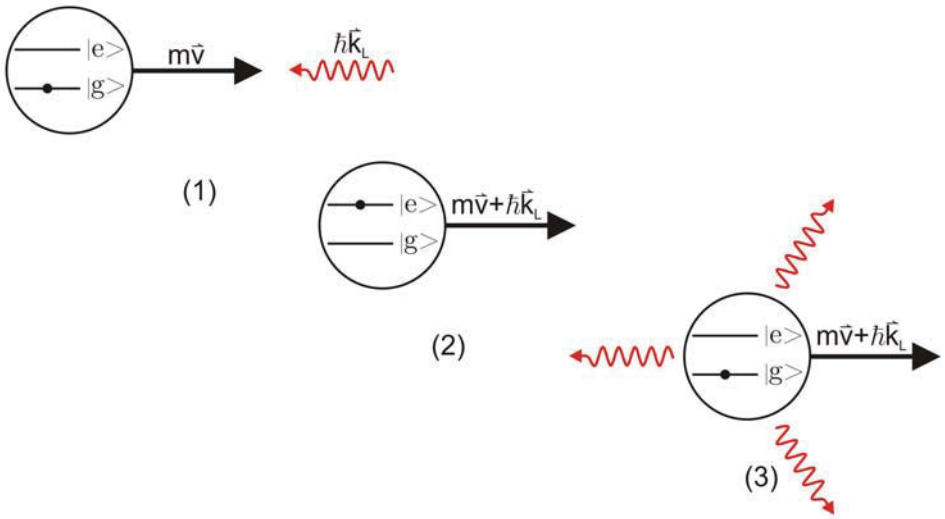

Figure 3.5 Scheme of the Doppler laser cooling cycle. (1) An atom in the ground state |g> with the momentum $m\vec{v}$ encounters a photon with a momentum $\hbar\vec{k}_L$. (2) Due to absorption of the photon, the atom is excited to the state |e> and its momentum is reduced by $\hbar\vec{k}_L$.
(3) Relaxation to the ground state by spontaneous emission of a photon in arbitrary directions for each process of absorption.

According to the above, we assume, a single atom A described by a two-level-system with an exited state $|e\rangle$ and a ground state $|g\rangle$, separated by an energy interval $E_e - E_g = \hbar\omega_A$. Assuming a monochromatic laser field L, with a frequency ω_L, the electrical field can be described as

$$\vec{E}_L(\vec{r},t) = \vec{e}_L(\vec{r})\hat{E}(\vec{r})\cos\left(\omega_L t + \vec{k}_L \cdot \vec{r}\right). \tag{3.17}$$

where $\vec{e}(\vec{r})$, $\hat{E}(\vec{r})$ and $\vec{k}_L$ are respectively the polarization, the amplitude and the wave vector of the laser field in $\vec{r}$. The excited state will decay by spontaneous emission with the rate $\Gamma = 1/\tau$, with the lifetime τ of the excited state $|e\rangle$.

The force due to the laser field, from absorption followed by spontaneous emission, can be written as [85]

$$\vec{F}_{light} = \text{photon momentum} \cdot \text{photon scattering rate} = \hbar\vec{k}_L \cdot \Gamma\rho_{ee}. \tag{3.18}$$

The population ρ_{ee} in the excited state is obtained by solving the optical Bloch equations (OBE):

$$\rho_{ee} = \frac{\Omega^2}{4\delta^2 + 2\Omega^2 + \Gamma^2}. \tag{3.19}$$

Here Ω is the Rabi frequency which determines the coupling strength between the atom and the light field and $\delta \equiv \omega_L - \omega_A$ is the laser detuning from the atomic resonance frequency.

According to (3.18) a moving atom with the velocity $\vec{v}$ and Doppler shift $\vec{k}_L \cdot \vec{v}$ leads to the light force

$$F_{light} = \hbar k_L \Gamma \frac{\Omega^2}{4\left(\delta - \vec{k}_L \cdot \vec{v}\right)^2 + 2\Omega^2 + \Gamma^2}. \tag{3.20}$$

For small velocities $\left(\vec{k}_L\vec{v} \ll \delta\right)$ a Taylor expansion [83] leads to

$$F_{light} = F_{light,0} + \beta v + \mathrm{O}\left(v^2\right). \tag{3.21}$$

The light force contains two contributions, a constant force $F_{light,0}$ and a motion-damping force βv with the damping coefficient

$$\beta = \hbar k_L^2 \frac{4S_0\left(\delta/\Gamma\right)}{\left(1 + S_0 + \left(2\delta/\Gamma\right)^2\right)^2}. \tag{3.22}$$

Here $S_0 \equiv \frac{2|\Omega|^2}{\Gamma^2} = \frac{I}{I_S}$ defines the saturation parameter on resonance with an atomic transition with a light field intensity I and a saturation intensity $I_S = \frac{2\pi^2\hbar c\Gamma}{3\lambda_L^3}$.

Assuming an ensemble of atoms with the above criteria (e.g. two-level system, etc.) confined in a linear quadrupole trap, the light force will cause the following effects on the ions, when exposed to a laser beam propagating along the trap axis.
According to (3.21) the atoms moving against the laser propagation ($v<0$) will be decelerated when β is negative. This occurs for negative values of detuning δ, i.e. red-detuned laser light. By contrast, for $\delta>0$ the atoms would be accelerated (Figure 3.6).

Disregarding all possible heating effects, the minimum temperature reachable with Doppler laser cooling is still limited. As described above, the direction of the spontaneous emission is random, leading to a "random walk" description of the atom's motion in momentum space [85]. The resulting limit to the temperature of laser cooling is the so-called Doppler limit, given by the Doppler temperature:

$$T_{Doppler} = \frac{\hbar\Gamma}{2k_B}. \qquad \textbf{(3.23)}$$

In case of the laser-cooled beryllium ions ($\Gamma \approx 2\pi\cdot 19.4$ MHz, [86]) used in this work, the Doppler limit is at $T_{Doppler} \approx 470\ \mu K$ [77][86]. Reaching this temperature is only possible under ideal conditions for a single ion in the trap centre and reducing all heating effects to a minimum.

It is sufficient to take only one laser beam for laser cooling in an ion trap. Despite the fact that only the atoms in the direction of propagation are translationally cooled, the remaining degrees of freedom are cooled due to the interactions of the ions with each other.

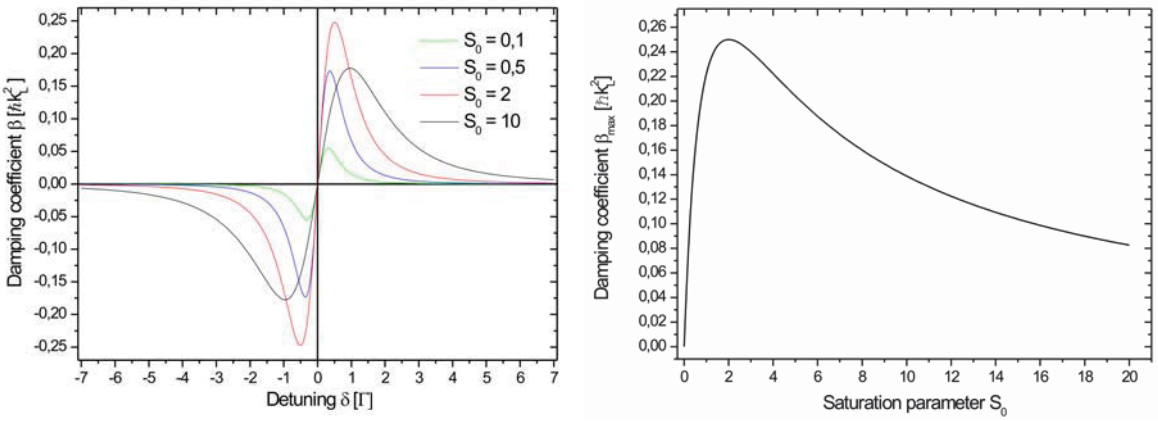

Figure 3.6 left: Damping coefficient β in the two level system as a function of detuning δ for different values of the saturation parameter S_0.
right: Damping coefficient β as a function of the saturation parameter S_0. For $\Delta=-\Gamma/2$ and $S_0=2$ and therefore with an intensity $I=2\cdot I_S$ (an intensity I which is twice as high as the saturation intensity I_S) the damping coefficient β reaches its absolute maximum value.

3.2.3 Doppler laser cooling of Be^+

Beryllium ($^9_4Be^+$), with an atomic mass of 9 auk., is the lightest hydrogen-like atomic ion that is suitable for laser cooling. It also enables *sympathetic cooling* of light molecules (refer to chapter 3.2.1).

For laser cooling of $^9Be^+$ ions one makes use of the $^2S_{1/2}(F = 2) - {}^2P_{3/2}$ transition. Due to the nuclear spin of I=1/2, hyperfine splitting of the energy levels occurs, leading to a splitting of $\Delta\nu_{HFS} = 1.25$ GHz of the $^2S_{1/2}$ ground state. If excited at a wavelength of λ_A=313.1327 nm, the $^2P_{3/2}$ state can decay into either hyperfine levels of the ground state. The preferred cooling procedure uses σ^+-polarized laser light to cause the $^9Be^+$ ions to cycle between the $^2S_{1/2}(F = 2, m_F = 2)$ ground state and $^2P_{3/2}(F = 3, m_F = 3)$ excited state (natural linewidth $\Gamma = 2\pi \cdot 19.4$ MHz [86]). Due to imperfections in the σ^+-polarization, decay into the F=1 ground state occurs as well. Using a part of the "main" cooling laser light by detuning the frequency via generating a sideband at −1.25 GHz, a "repumper laser" can deplete the F=1 ground state. In addition, a continuous red-detuning of the 313 nm cooling laser light over the Doppler broadened line is required for most effective cooling of the $^9Be^+$-ions (see 3.2.2).

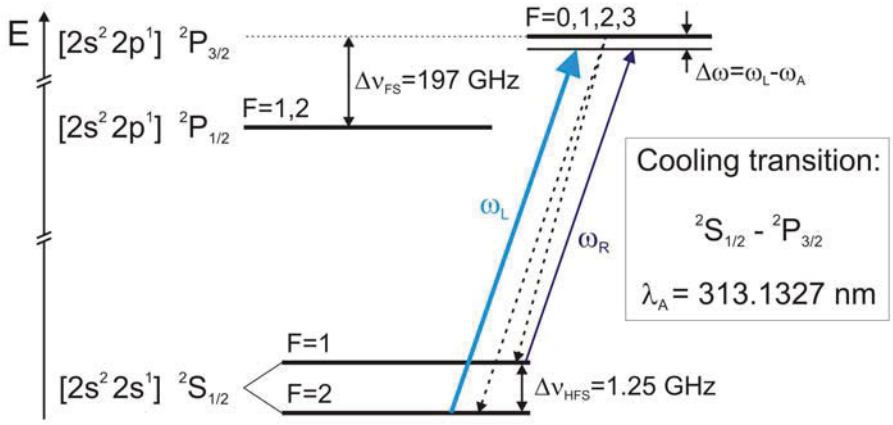

Figure 3.7 Level scheme of the relevant laser cooling transitions of Be^+ [77].

3.3 Coulomb ion crystals

According to the discussion in chapter 3.1.3, the motion of ions, confined in the linear quadrupole trap is determined by the *pseudo potential*

$$\Phi_{ps}(x,y,z) = \frac{1}{2}\frac{m}{Q}\omega_{\mathrm{sec},r}^2\left(x^2+y^2\right)+\frac{1}{2}\frac{m}{Q}\omega_{\mathrm{sec},z}^2 z^2$$

and their mutual Coulomb interaction

$$\Phi_{C,i} = \frac{1}{4\pi\varepsilon_0}\sum_j \frac{Q_j}{r_{ij}}. \qquad \textbf{(3.24)}$$

The neighbouring ions *j* with charges Q_j generate an electric potential $\Phi_{C,i}$, felt by an ion *i* at distance r_{ij}. When possessing the same charges, the ions, confined in the trap center by the trap potential, will electrostatically recoil from each other. As a result, the ions would form a diffuse ion cloud, in which the ions would move in a disordered way according to their thermal velocities.

When the translational energy of the ions is sufficiently reduced due to laser cooling, the ion ensemble can change from a disordered ion cloud to an ordered ion crystal. For the appearance of this so called *Coulomb crystallization* it is crucial that, in comparison to the particles' mutual interactions, the disturbing translational motion is minor.
The relative contribution of both effects can be described by the *plasma coupling parameter*

$$\Gamma = \frac{1}{k_{\mathrm{B}}T}\cdot\frac{Q^2}{4\pi\varepsilon_0 a_{WS}}. \qquad \textbf{(3.25)}$$

It represents the ratio of the mean Coulomb energy of interaction with the neighbouring ions and the thermal energy per degree of freedom. The ions' mean distance is given by the *Wigner-Seitz radius*

$$a_{WS} = \left(\frac{3}{4\pi n_0}\right)^{1/3}, \qquad \textbf{(3.26)}$$

which is defined as the radius of the sphere with a volume equal to the volume per ion, where n_0 is the ion density in the ensemble.

Non-neutral plasmas in general and trapped ion ensembles especially can be characterized according to the plasma coupling parameter Γ.
In case of $\Gamma < 2$ the ensemble is purely gaseous. For $\Gamma \gtrsim 1$ the plasma is called strongly coupled. For $\Gamma \gtrsim 2$, a phase transition to a liquid state due to the occurrence of a short-range order is predicted by MD simulations of infinite non-neutral plasmas [87].

In case of $\Gamma > 170$, MD simulations and thermodynamic approaches predict another phase transition to the structured phase. Here, the typical mean ion distance is $a_{WS} \approx 30\ \mu\text{m}$ at translational temperatures of about 3 mK [88].

In this work, one-component ion crystals containing beryllium ions are used for sympathetic cooling. Therefore beryllium is evaporated from an oven, positioned from the outside close to the linear Paul trap electrodes in the trap center region. Following the evaporation process, an electron gun generates the Be^+-ions, cooled by a laser at λ_A=313.1327 nm. The image presented in Figure 3.8 was taken with a CCD camera, observing the spontaneous fluorescence emission of the atomic ions when exposed to the cooling laser.
The next step, following the trapping and laser cooling of the Be^+-ions, is the adding of the HD^+-ions to trap. For this purpose neutral HD-gas is inserted into the trap and itself ionized by the electron gun.
Trapping both ion species simultaneously and achieving a good spatial overlap makes the sympathetic cooling most effective. According to the *Mathieu (stability) parameters* discussed in chapter 3.1.2, formula (3.10), the condition for stable trapping is achieved for

$$q = q_x = -q_y = \frac{2QU_{RF}}{mr_0^2\Omega^2} < 0.9\ .$$

In addition, a small q-parameter is advantageous, since particles located closer to the trap axis posses a smaller heating rate. Due to $q \sim Q/m$, adjusting the trap potentials $U_{trap,LC}$ and $U_{trap,SC}$ for each ion species to be similar, a good spatial overlap can be achieved for $Q^2/m_{LC} \approx Q^2/m_{SC}$. Thus, choosing (light) beryllium ions to sympathetically cool light (like HD^+-ions) and medium-sized atoms and molecules is favored.

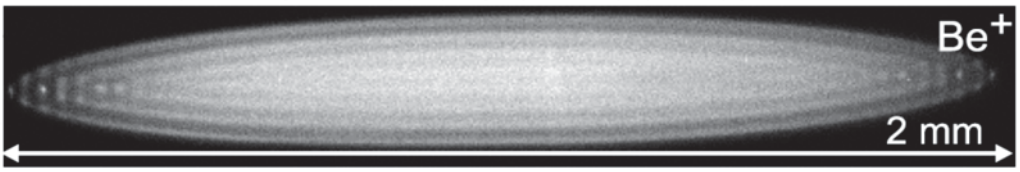

Figure 3.8 Image of a large typical one-component Coulomb crystal [74]. It contains 2500 laser-cooled $^9Be^+$-ions at a translational temperature of 20 mK. The trap axis z is horizontal.

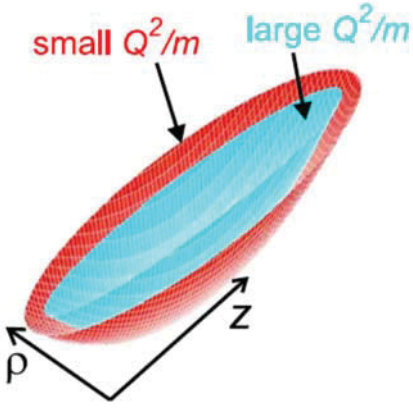

Figure 3.9 Sketch of the effective trap potential for different values of Q^2/m. Here $\rho = \sqrt{x^2 + y^2}$ and z are the radial and axial trap coordinates [74].

Figure 3.10 illustrates a typical beryllium crystal after loading and sympathetic cooling of HD^+ molecules. The SC particles radially separate from the atomic coolants, according to their mass-to-charge ratio. For sympathetically cooled HD^+ ions, as result of the smaller mass-to-charge ratio, the trap potential is steeper. Thus, it is energetically favorable when the ions are located closer to the trap axis as compared to the Be^+ atomic coolants. An indication of this behavior is the appearance of a dark, non-fluorescing core in the initially pure ion crystal.

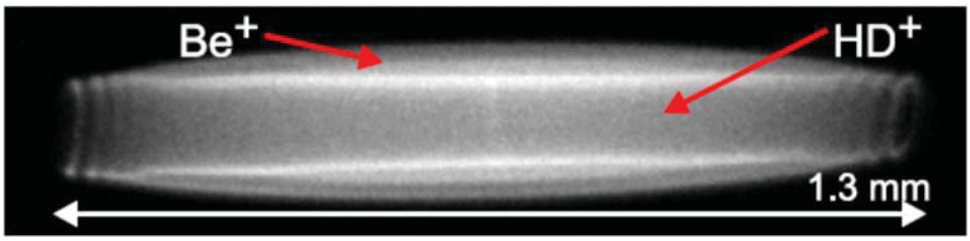

Figure 3.10 Image of a typical mixed-species Coulomb crystal [74]. It contains 2000 laser-cooled Be^+-ions and 100 sympathetically cooled HD^+-ions at 30 mK. The trap axis z is horizontal.

A CCD camera image of an actual crystal, used in our experiments at 10-15 mK, is presented in the following. The crystal is about 2.1 mm long and contains about 1500 Be^+ ions and 100-150 HD^+ ions.

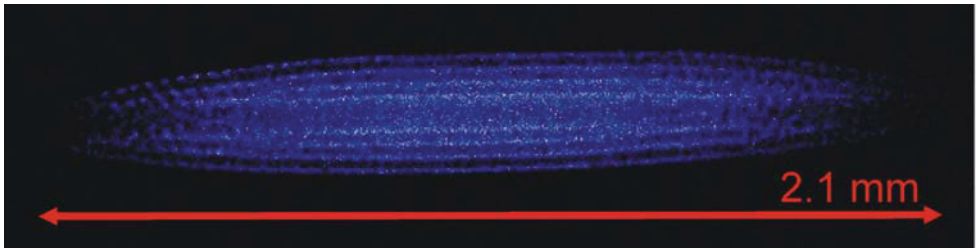

Figure 3.11 Image of an actual mixed-species Coulomb crystal, used for our measurements. It contains about 1500 laser-cooled Be^+-ions and 100-150 sympathetically cooled HD^+-ions at 10-15 mK. The trap axis z is horizontal.

3.4 Rotational cooling

In order to perform high precision spectroscopy with charged molecules, a variety of preparations have to be conducted. As has been shown, charged molecules can be effectively stored in ion traps and translationally cooled using sympathetic cooling by atomic ions, with storage times exceeding several hours. In case of the HD^+ molecular ion used in this work, the production by electron impact ionization and the interaction with the black-body radiation of the surrounding vacuum chamber yields a significant population of a substantial number of internal states. An important procedure is the manipulation of internal states by transferring population between rotational states. The idea, proposed by Vogelius et al. [50], is to optically transfer a significant fraction of the population of rotational levels by "*optically pumping*" via a higher vibrational level, from where the population spontaneously decays into the ro-vibrational ground level. In addition, the omnipresent black-body radiation continuously repopulates the levels addressed by the radiation from higher energy levels, further increasing the effectiveness of this procedure.
As has been shown in [51], it is possible to optically pump about 75 % of an ensemble of HD^+ into the ro-vibrational ground level $(\upsilon = 0,\ L = 0)$.

The optical pumping scheme used in this work is shown in Figure 3.12. All relevant transitions take place within the $1s\sigma$ electronic ground state of the molecule. The rotational cooling is performed by a $\lambda_p = 5484$ nm quantum cascade laser, driving the dipole allowed $(0,2) \rightarrow (1,1)$ transition. For part of the measurements, a $\lambda_p' = 2713$ nm diode laser was used to drive the $(0,1) \rightarrow (2,0)$ transition. Compared to pure rotational excitation, e.g. $(0,0) \rightarrow (0,1)$, or a microwave transition within a rotational level, vibrational transitions offer a much faster spontaneous decay following the excitation process.
The overtone transition $(0,1) \rightarrow (2,0)$ with $\Delta\nu = 2$ is allowed due to imperfect parabolic potential energy curves of the electronic ground state of HD^+. Population pumped at λ_p' to the $(2,0)$ state decays by spontaneous emission to the $(1,1)$ state with a rate of approx. 32 s^{-1}. Another decay to $(0,0)$ due to the selection rule $\Delta L = 1$ can occur at approx. 6 s^{-1} or to $(0,2)$ at approx. 12 s^{-1}. The latter is again subject to optical pumping at λ_p. With these relatively short decay times, a reasonably rapid pumping of the molecule can be achieved.
The use of the rotational cooling laser is of importance, because it significantly increases the fractional population of molecules in $(\upsilon = 0,\ L = 0)$ from ca. 10% to 60 - 75% [51].

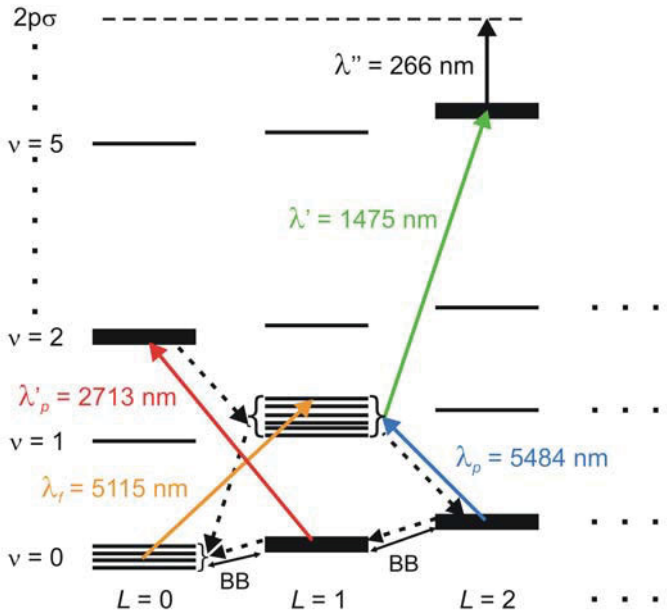

Figure 3.12 Energy levels of HD^+ with relevant transitions. The hyperfine splitting of the levels is only shown schematically as lines for the $(\upsilon = 0,\ L = 0)$ and $(\upsilon = 1,\ L = 1)$ levels. For all other levels, the hyperfine splitting is implied in the thick bars. Full lines: laser induced transitions, dashed lines: some relevant spontaneous emission transitions, BB: black-body induced transitions.

4 The 5 µm laser spectrometer

In order to perform high resolution spectroscopy of cooled molecules, it is obviously necessary to use narrow-linewidth laser sources. In addition, it is also necessary to measure their frequencies with respect to a primary frequency standard. One approach to achieving the desired 5 µm radiation and determining the laser's frequency is the parametric down conversion process of two lasers with relatively short wavelengths. Today's quantum cascade lasers (QCL) offer the desired wavelength ranges, but their stabilization for application to high resolution spectroscopy is still challenging, because they do not overlap with the spectral range of current frequency combs of the Ti:sapphire or Er:fibre types.
In this work, the difference frequency generation (DFG) of a cw Nd:YAG laser, frequency stabilized to a hyperfine transition in molecular iodine, and of a novel quantum dot external cavity diode laser (QD-ECDL) has been implemented. Figure 4.1 gives an overview of the system.

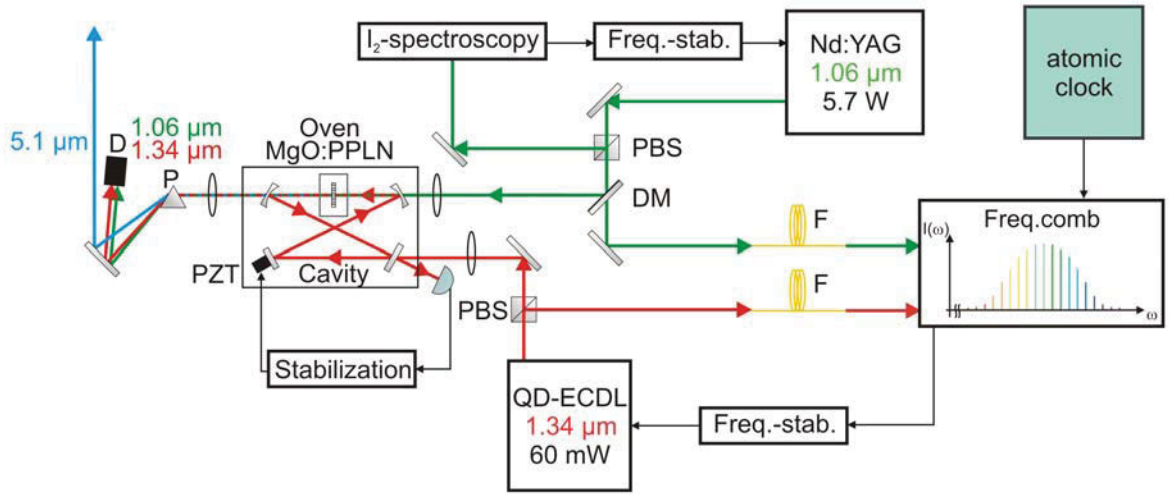

Figure 4.1 Simplified schematic of the 5.1 µm source showing the main components of the system. A more detailed schematic is presented in Figure 4.16. F: single mode optical fibre, PBS: polarizing beam splitter cube, DM: dichroic mirror, PZT: piezo, P: prism, D: beam dump.

4.1 DFG in periodically poled MgO:$LiNbO_3$

The generation of optical frequencies in the mid-IR-range is a challenging task. Focusing on the process of parametric down conversion, there are two implementations, difference frequency generation (DFG) and optical parametric oscillation (OPO). Examples are given in the references [56][57][58][59][60], where the longest wavelength reached has been 4.57 µm [59]. The main limiting effect in reaching the desired wavelengths is the observation of intrinsic absorption of the typically-used oxide crystals beyond 4.5 µm [60].

In this work, we have studied two different crystals, on the one hand orientation-patterned (OP) GaAs, on the other hand magnesium-doped periodically-poled lithium niobate ($MgO:LiNbO_3$), to extend the upper wavelength limit into the strongly absorbing spectral range.
Choosing these crystals as candidates for the DFG for 5.1 µm is motivated by the high / very high nonlinearity (d_{eff} = -34.4 pm/V / d_{eff}= -100 pm/V) of the crystals. While $MgO:LiNbO_3$ has become nowadays a widely used standard material, we are grateful to have the possibility to test a GaAs crystal provided by the THALES group.

4.1.1 Theory of difference frequency generation (DFG)

In the following, the basic concept of frequency conversion in nonlinear-crystals shall be given; more detailed descriptions can be found in [61][62].

The electric field $\vec{E}(\vec{r},t)$ of an incoming wave entering a medium leads to a deformation of the electron distribution around the single atomic nuclei of the crystal. More precisely, light electrons oscillate relative to the heavy atomic nuclei with the frequency of the radiation. The sum of to these oscillating dipoles is called induced polarization $\vec{P}(\vec{r},t)$.
In a dielectric medium, the polarization is not only proportional to the electric field $\vec{E}(\vec{r},t)$ according to $\vec{P}(\vec{r},t)=\varepsilon_0\cdot\chi^{(1)}\vec{E}(\vec{r},t)$ ($\chi^{(1)}$: linear susceptibility). Nonlinear contributions to the polarization occur and can be expressed in a Taylor expansion of the electric field:

$$\vec{P}(\vec{r},t)=\varepsilon_0\cdot\chi^{(1)}\vec{E}(\vec{r},t)+\vec{P}_{NL} \quad \text{with} \quad \vec{P}_{NL}=\varepsilon_0\left[\chi^{(2)}\cdot\vec{E}^2(\vec{r},t)+\chi^{(3)}\cdot\vec{E}^3(\vec{r},t)+\ldots\right]. \qquad \textbf{(4.1)}$$

The quantities $\chi^{(2)}$ and $\chi^{(3)}$ are termed (nonlinear) susceptibilities of second and third order and are material specific parameters.
The contribution of the $\chi^{(2)}$ susceptibility to the polarization is important for the second harmonic generation (SHG), the sum and difference frequency generation (SFG / DFG), as well as the optical parametric amplification (OPA).
Effects that result from the contribution of the $\chi^{(3)}$ susceptibility are generation of the third harmonic (THG), self focusing, induced scattering (Rayleigh, Raman) and two-photon absorption.

In case of the difference frequency generation (DFG), two pump waves with the frequencies ω_3 and ω_2 generate a new wave with the frequency $\omega_1 = \omega_3 - \omega_2$. According to the convention $\omega_3>\omega_2>\omega_1$, the waves with the higher frequencies are named pump wave (ω_3) and signal wave (ω_2), the generated wave with the lowest frequency is named the idler wave (ω_1).

Figure 4.2 Simplified principle of the difference frequency generation (DFG) in a nonlinear crystal.

The difference frequency generation depends on the $\chi^{(2)}$ susceptibility, a tensor of third order, which can be described by the so called nonlinear coefficient $d_{ijk} \equiv \frac{1}{2}\chi^{(2)}_{ijk}$.

$\chi^{(2)}_{ijk}$ is a tensor of 3rd order (3x3x3 matrix), and as mentioned above, it is a material specific parameter, which is determined by the crystal properties. The nonlinear or *d-coefficient* d_{ijk} describes the particular coefficient of the tensor.

A simplification is brought about by the symmetry rules of *Kleinman* [63]. It can be shown that the $\chi^{(2)}$ tensor is symmetric in case of the assumption of lossless crystals, which is the case for linear interactions. The sequence of indices is without physical relevance $\left(\chi_{ijk} = \chi_{ikj}\right)$ and therefore can be substituted by contracted indices, so that the tensor can be transformed into a 3x6 matrix.

$$\begin{aligned} xx &= 1 \qquad yz = zy = 4 \\ yy &= 2 \qquad xz = zx = 5 \\ zz &= 3 \qquad xy = yx = 6 \end{aligned} \tag{4.2}$$

The relation between the polarization of 2nd order and the electric field components of a monochromatic wave are given by:

$$\vec{P}^{(2)}_{NL} \equiv \begin{bmatrix} \left(P^{(2)}_{\omega_1}\right)_x \\ \left(P^{(2)}_{\omega_1}\right)_y \\ \left(P^{(2)}_{\omega_1}\right)_z \end{bmatrix} = 2\varepsilon_0 \begin{bmatrix} d_{11} & d_{12} & d_{13} & d_{14} & d_{15} & d_{16} \\ d_{21} & d_{22} & d_{23} & d_{24} & d_{25} & d_{26} \\ d_{31} & d_{32} & d_{33} & d_{34} & d_{35} & d_{36} \end{bmatrix} \cdot \begin{bmatrix} \left(E_{\omega_3}\right)_x \left(E^*_{\omega_2}\right)_x \\ \left(E_{\omega_3}\right)_y \left(E^*_{\omega_2}\right)_y \\ \left(E_{\omega_3}\right)_z \left(E^*_{\omega_2}\right)_z \\ \left(E_{\omega_3}\right)_y \left(E^*_{\omega_2}\right)_z + \left(E_{\omega_3}\right)_z \left(E^*_{\omega_2}\right)_y \\ \left(E_{\omega_3}\right)_x \left(E^*_{\omega_2}\right)_z + \left(E_{\omega_3}\right)_z \left(E^*_{\omega_2}\right)_x \\ \left(E_{\omega_3}\right)_x \left(E^*_{\omega_2}\right)_y + \left(E_{\omega_3}\right)_y \left(E^*_{\omega_2}\right)_x \end{bmatrix} \tag{4.3}$$

Assuming that the electric fields $\vec{E}_{\omega_{3,2,1}}(\vec{r},t)$ propagate in the z-direction through a nonlinear crystal, the corresponding fields and the polarization $\vec{P}_{NL,\omega_1}(\vec{r},t)$ can be written as:

$$\left(\vec{E}_{\omega_{3,2,1}}\right)_{x,y,z}(\vec{r},t) = \hat{e}_{x,y,z} \cdot E_{0\omega_{3,2,1}}(\vec{r}) \cdot e^{i\omega_{3,2,1}\cdot t} \cdot e^{-i\cdot k_{3,2,1}\cdot z} + c.c.$$

$$P_{NL,\omega_1}(\vec{r},t) = \hat{e}_z \cdot 4 \cdot d_{eff} \cdot \varepsilon_0 \cdot E_{0\omega_3}(\vec{r}) \cdot E^*_{0\omega_2}(\vec{r}) \cdot e^{i\cdot\omega_1 t} \cdot e^{-k_1 z} + c.c.\ ,$$

with the wave numbers: $k_{\omega_{3,2,1}} = \frac{n_{\omega_{3,2,1}} \cdot \omega_{3,2,1}}{c}$.

$E_{0\omega_{3,2,1}}(\vec{r})$ is the field amplitude, $\hat{e}_{x,y,z}$ is the unit vector of the polarization and d_{eff} is the effective nonlinear coefficient which determines the value of the polarization $\vec{P}_{NL,\omega_1}(\vec{r},t)$. Depending on the direction and the polarization of the fundamental wave propagating through the crystal, different nonlinear coefficients of the susceptibility sensor are effective.

4.1.2 Quasi-phase-matching

Two incoming waves with different frequencies entering a nonlinear crystal can generate waves with the difference frequency, the sum frequency or the double frequency (second harmonic) of the single waves. The preference for one of the possible frequencies depends on the matching of the phase velocities between the polarization wave and the to be generated wave.
In the case of perfect phase matching, the conservation of energy $\omega_i = \omega_p - \omega_s$ as well as the conservation of momentum $\vec{k}_i = \vec{k}_p - \vec{k}_s$ has to be fulfilled. In this case, the generated wave is in phase with the polarization wave induced by the two incoming waves, and the energy transfer to the generated wave is maximal. Due to dispersion, the two incoming waves of different frequencies will have a phase mismatch of π after traveling a distance of the coherence length $L_c = \frac{\pi}{|\Delta\vec{k}|}$, causing a minimum energy transfer to the generated wave.

In order to compensate the phase mismatch, it is desired to achieve

$$\Delta\vec{k} = \vec{k}_p - \vec{k}_s - \vec{k}_i = 2\pi\left(\frac{n_p}{\lambda_p} - \frac{n_s}{\lambda_s} - \frac{n_i}{\lambda_i}\right) = 0\,.$$

The refractive indices in a birefringent medium are strongly dependent on the temperature. Therefore it is possible to optimize to a certain degree the phase matching conditions by adjusting the crystal's temperature.

A more elegant way of achieving the phase matching conditions is the method of quasi-phase matching.

By dividing the crystal into segments with the coherence length $L_c = \frac{\pi}{|\Delta\vec{k}|}$ and arranging them such that each segment and therefore its optical axis is oriented 180° to the one before, the phase mismatch in each segment will be compensated by that in the following segment. After passing through two segments of total length $2 \cdot L_c$ the polarization wave and the generated signal wave are back in phase again. This procedure enables one to use parallel polarized

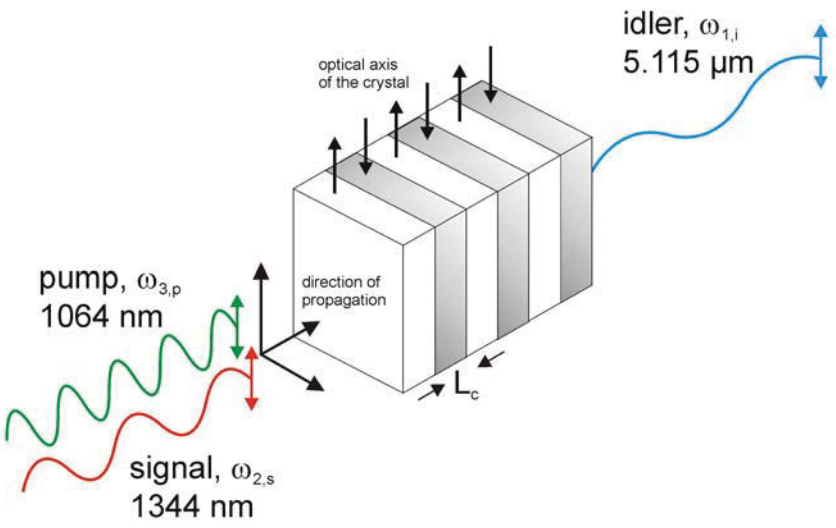

Figure 4.3 Principle of quasi-phase matching by use of differently-oriented crystal elements. The wave propagation is perpendicular to the optical axis of the crystal. The polarization is parallel to the optical axis and remains parallel (in the ideal case) for the generated idler wave.

pump waves (pump and signal wave) and therefore to take advantage of the larger main diagonal elements of the susceptibility tensor, leading to a more effective conversion. In this case, the polarization of the generated wave (idler) is also parallel polarized.

The technical process of manipulating a nonlinear crystal is called *optical poling*. In this process, the above described periodic structure is implemented in the nonlinear crystal by applying a strong electric field (e.g. 21 kV /mm for 50 ms [64]), creating permanent ferroelectric domains in the crystal which remain stable up to a temperature of 800 °C.

With the poling period $\Lambda = 2 \cdot L_C = 2 \cdot \frac{\pi}{\left|\Delta \vec{k}\right|}$ the phase mismatch in the case of the process of quasi-phase-matching can be written as

$$\Delta \vec{k}_q = \vec{k}_p - \vec{k}_s - \vec{k}_i - \frac{2\pi}{\Lambda}. \qquad \textbf{(4.4)}$$

Using the *Sellmeier equation* including the material constants for the particular material use, the refractive indices for the ordinary and the extraordinary beam of each wavelength used in the conversion process can be determined. In this thesis, a magnesium-doped lithium niobate crystal ($MgO:LiNbO_3$, MgO 5 mol.%) has been used. According to [65] the *Sellmeier equation* for the extraordinary beam propagating through this crystal is:

$$n_e^2(\lambda) = 4.5469 + 0.094779 / \left(\lambda^2 - 0.044394\right) - 0.026721 \cdot \lambda^2. \qquad \textbf{(4.5)}$$

Using (4.4) and considering the thermal expansion, the necessary value $\Lambda(T)$ of the poling period can be calculated for each conversion process at a given temperature.

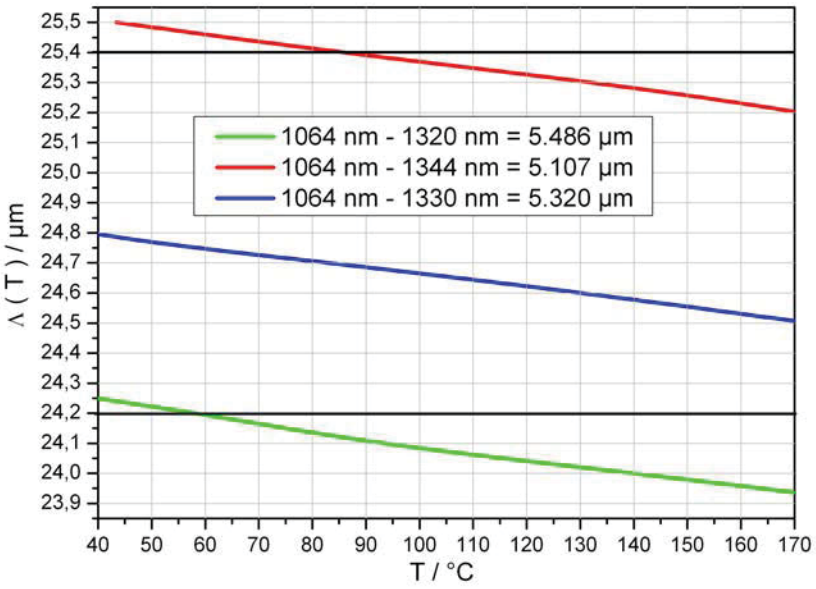

Figure 4.4 Temperature dependence of the calculated poling period Λ for generation of the desired wavelengths. For a fixed poling period, a suitable working temperature for most efficient frequency conversion can be read off.

The $MgO:LiNbO_3$ crystal used in this thesis is 7.4 mm long, 0.5 mm thick (width 10 mm) and possesses six different poling periods from 21.5 µm to 25.4 µm. Especially for the desired difference frequency generation of 5.115 µm, the poling period of 25.4 µm has been used at a temperature of 71°C for most effective frequency conversion.

4.1.3 Choice of nonlinear crystals

In choosing an appropriate nonlinear crystal for the desired frequency conversion, several characteristics have to be taken into consideration. Especially in the case of difference frequency generation in this work, the range between the 1064 nm pump wave and the 1344 nm signal wave on the one hand, and the generated 5.1 µm idler wave on the other hand, which has to be covered by a crystal's properties, is challenging. While the choice of a crystal with a high nonlinear coefficient and therefore high conversion efficiency (chapter 4.1.1) is obvious, the occurring absorption of the pump-/signal waves or the idler wave in some nonlinear crystals decreases the conversion efficiency and restricts the utilization.
In order to evaluate the pros and cons of a certain available nonlinear crystal, test measurements have been carried out, especially concerning the absorption in crystals at the used wavelengths.
With a quantum cascade laser (QCL, Maxion DQ5-M575 F) at 5.485 µm provided by the group of Peter Hering, the attenuation coefficient α of the following test samples could be roughly estimated:

MgO:CLN	MgO:SLT	PP-$LiNbO_3$
$\alpha \approx 6$ cm^{-1}	$\alpha \approx 4$ cm^{-1}	$\alpha \approx 9$ cm^{-1}

Due to the observed absorption close to the desired 5.1 µm radiation in the MgO doped congruent lithium niobate ($MgO:LiNbO_3$, CLN) or stoichiometric lithium tantalite ($MgO:LiTaO_3$) and the pure periodic poled lithium niobate ($PP\text{-}LiNbO_3$), testing an alternative material was of interest.

Orientation patterned (OP) GaAs

In comparison to other standard quasi-phase-matched oxide nonlinear materials (e.g. $PP\text{-}LiNbO_3$), GaAs is not restricted due to intrinsic absorption in the mid-IR spectral region at wavelengths beyond 4.5 µm [60]. GaAs crystals feature a high transparency range (0.9 – 17 µm) and a very high nonlinear coefficient ($d_{eff} = -100$ pm/V). Because they do not possess birefringence, a different quasi-phase-matching technique to the one described in chapter 4.1.2 is realized. As the electric field poling technique cannot be implemented, the crystal must be grown with its optical axis periodically reversed (*orientation patterning*, OP). Fabrication of wafer-sized OP-GaAs structures can be realized [66].

The tested GaAs sample (manufactured by THALES group) was 33 mm long, 0.45 mm thick and possessed several periods, from which one at 33.2 µm has been used.
Despite our efforts, generated radiation at 5.5 µm using 1064 nm (pump) and the QD-ECDL tuned to 1320 nm (signal) could not be observed. According to absorption measurements, the attenuation coefficient α at 100 °C of the used OP-GaAs crystal including the Fresnel-reflection of both surfaces could be determined to $\alpha \approx 5.06$ cm^{-1} at 1064 nm (Figure 4.5).

Due to this high absorption of the pump beam, the transmission of 1064 nm radiation was limited to only 19 %, leading to damage of the crystal and abandoning of the crystal test (Figure 4.6).

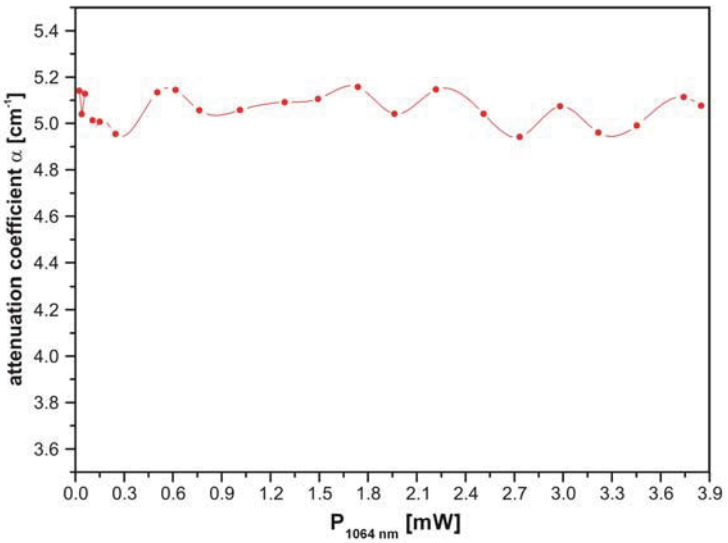

Figure 4.5 Measurement of the attenuation coefficient α of OP-GaAs at 1064 nm and 100 °C depending on the laser power.

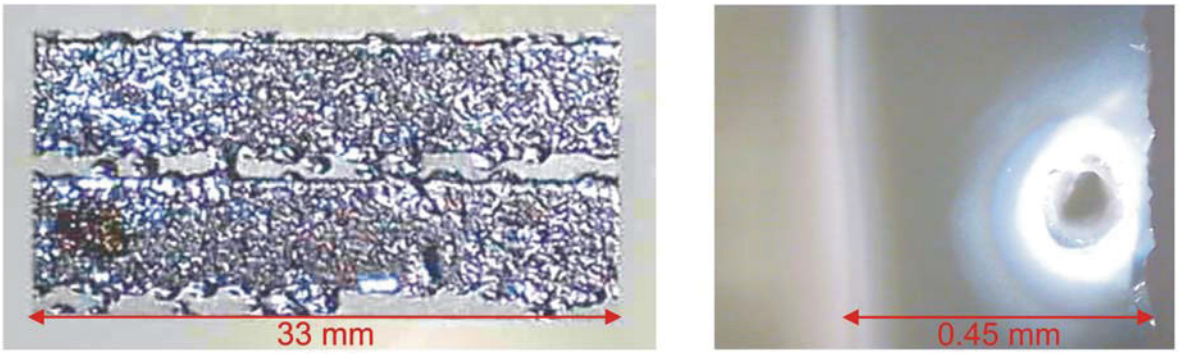

Figure 4.6 left: Photo of the used OP-GaAs crystal (10 x magnification).
right: Photo of the damaged input surface of the crystal (33.2 µm period) (200 x magnification).

Periodically poled lithium niobate (MgO:PPLN)

In this work, a magnesium oxide doped periodically poled lithium niobate (PP-MgO:$LiNbO_3$) crystal has been chosen, thus taking into consideration the expected absorption losses for the generated 5.1 µm radiation. The attenuation coefficient of the crystal has been independently measured at 5.485 µm to be $\alpha = 6.75\ \text{cm}^{-1}$.

As already mentioned in chapter 4.1.2, the crystal used is 7.4 mm long, 0.5 mm thick (height 10 mm) and possesses six different poling periods from 21.5 µm to 25.4 µm.

The MgO-doped crystal (5 mol. %) has similar effective nonlinear coefficients $\left(d_{eff} = \frac{2}{\pi} d_{33} = \frac{2}{\pi} \cdot (-34.4\ \text{pm/V}) \right)$ to pure $LiNbO_3$ but exhibits a higher optical damage threshold. In case of *optical damage*, absorption of photons at impurities in the crystal can occur, which leads to a local intensity-dependent change of the refraction index and therefore a change in beam propagation, resulting in a decrease in the conversion efficiency. While this effect can be suppressed in pure $LiNbO_3$ by operation at temperatures above 150 °C, the MgO-doped crystals allow working even at room temperature, giving advantages for thermal stabilization especially when used in resonators.

In order to minimize reflection losses and retain good resonator characteristics, crystal faces are plane parallel polished and have been AR coated for the wavelengths used.

In total, five different poling periods (21.8 µm, 22.1 µm, 22.4 µm, 24.2 µm, 25.4 µm) of the crystal have been tested in a single-pass configuration, before the final setup for the DFG of 5.115 µm including a resonator for the 1344 nm radiation was realized (see chapter Figure 4.4).

The first successful frequency conversion was tested with a difference-frequency generation (DFG) of a 808 nm laser diode and a 1064 nm Nd:YAG laser (Innolight Mephisto 2500) generating radiation around 3.3 µm.

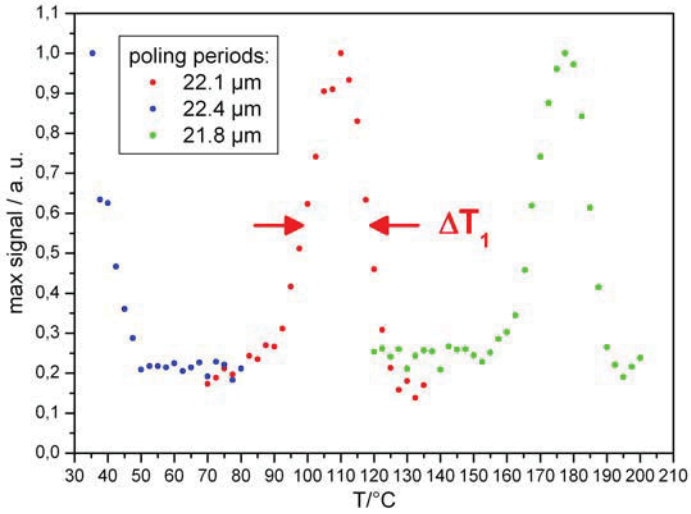

Figure 4.7 Measurement of the temperature dependence of the difference frequency generation (DFG) around 3.3 µm $(\Delta T_1 \approx 19.4°C)$.

Choosing the poling period of **Λ=24.2 µm** and the difference frequency generation (DFG) of 5.5 µm using 1064 nm (pump) and the QD-ECDL tuned to around 1320 nm (signal), the following temperature dependence of the generated radiation could be observed:

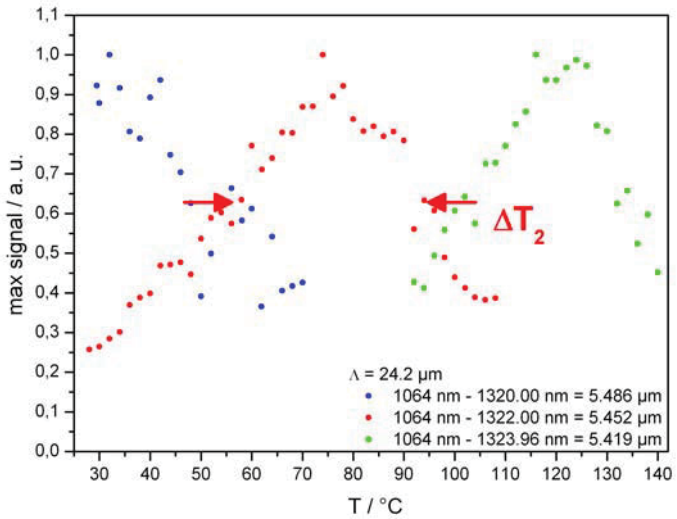

Figure 4.8 Measurement of the temperature dependence of the difference frequency generation (DFG) between 5.42 and 5.48 µm $(\Delta T_2 \approx 38.8°C)$.

Comparing the temperature dependence of the DFG for the different wavelengths presented in Figure 4.7 and Figure 4.8 reveals a large difference due to the increase of absorption for longer wavelengths, reducing the effective length of interaction between the pump and signal beams.

Retuning the QC-ECDL to the range around 1344 nm and choosing the poling period of the crystal of **Λ=25.4 µm**, the difference frequency generation in the range between 5.09 and 5.13 µm was demonstrated.

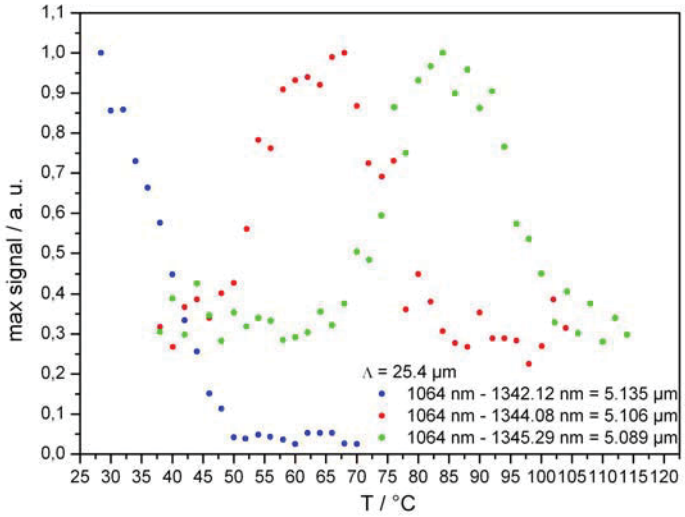

Figure 4.9 Measurement of the temperature dependence of the difference frequency generation (DFG) between 5.09 and 5.13 µm.

By building up the resonator for the 1344 nm radiation around the oven including the PP-MgO:$LiNbO_3$ crystal as described in chapter Figure 4.4, the available total power for the DFG at 1344 nm increased by a factor of up to 60. Due to the known absorption of the generated 5.1 µm radiation, great effort had to be invested in calibration and maximization of the output power. Instead of positioning the beam waists of the pump and signal beam in the crystal's center for best beam overlap, it was necessary to move them iteratively from the crystal's back surface by moving the whole oven with translation stages while observing the output power. According to calculations and respecting the geometry of the 1344 nm enhancement cavity, the waist of the QD-ECDL in the crystal has been set to $w_0 \approx 83$ µm. Expecting the highest conversion efficiency for similarly shaped and positioned beam waists for the pump and signal beam, a measurement of the beam characteristics after the output power optimization shows the following results.

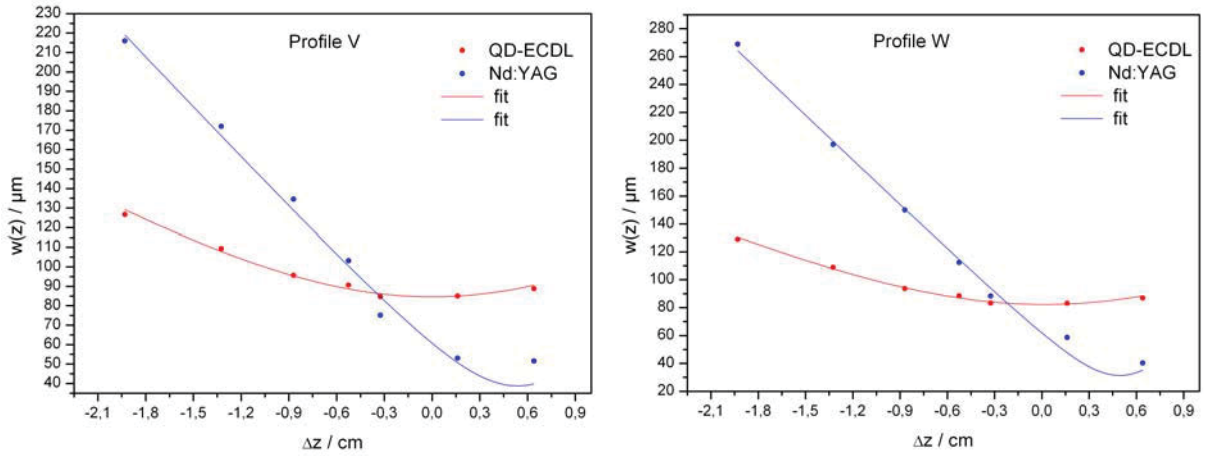

Figure 4.10 Measurement and fit of the beam shapes and beam waists in the crystal with respect to the position of the waist of the QD-ECDL beam. The beams enter the crystal from left (Profile V: orientation 45°, Profile W: orientation 135° to optical table).

Due to positioning the crystal in the enhancement cavity of the 1344 nm radiation, optimization of the cavity alignment directly determines the crystal's position as well. Changing its position or the angle of incidence of the QD-ECDL beam by rotating the crystal

directly affects the coupling and enhancement efficiency. Due to different beam shapes of the lasers used, their behavior following the use of lenses and telescopes for beam manipulation results in a slightly different beam propagation through the crystal. As can be seen in Figure 4.10, the position of the waist of the pump wave at 1064 nm is about 5 mm behind the waist of the signal wave at 1344 nm, offering a similar beam diameter in the given beam waist range.

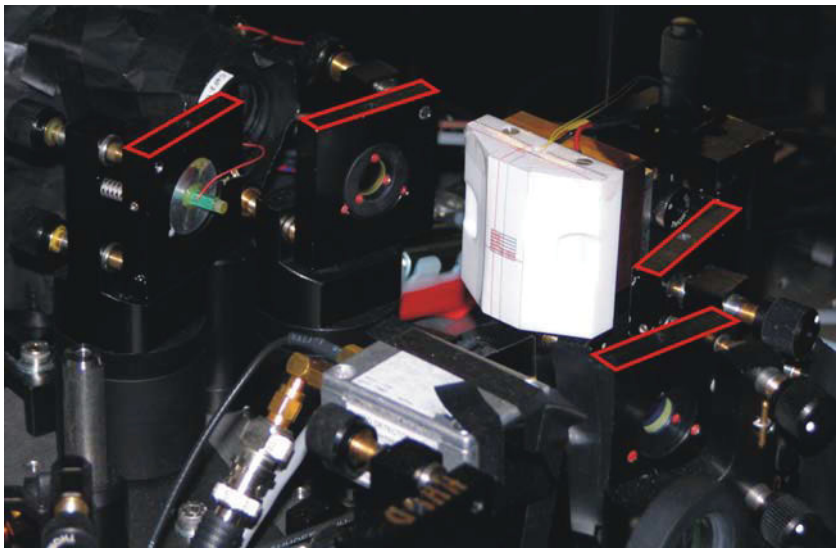

Figure 4.11 Photograph of the Peltier element driven oven including the MgO:$LiNbO_3$ crystal. The four surrounding mirrors forming the bow-tie type resonator can be recognized as well. The photodiode used for the Pound Drever Hall stabilization is in front (silver box).

During the optimization process, the temperature dependence of the total generated output power was more carefully investigated for the target wavelength of 5.115 µm.

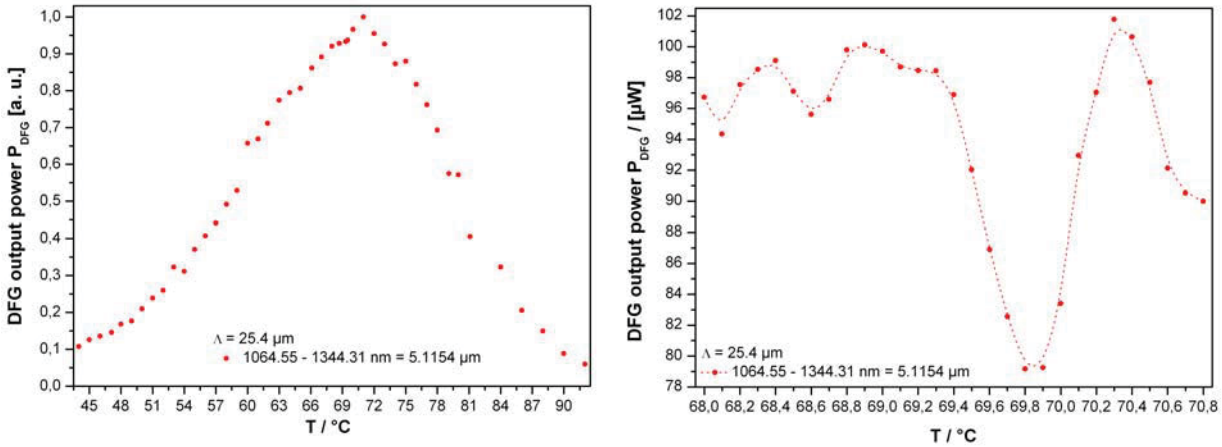

Figure 4.12 left: Temperature dependence of the difference frequency generation over a wide temperature range.
right: Signal optimization by temperature adjustment in the tip region.

Optimizing the temperature for the process of quasi-matching described in chapter 4.1.2 also affects the resonator parameters for the enhancement of 1344 nm radiation. As can be seen in Figure 4.12, the maximum output power at 5.115 µm varies to a small degree already within a temperature change of some tenths of a °C. Although very small, the temperature variation leads to a slight change in the cavity coupling, so that in addition, the circulating power

experiences minor fluctuations leading to changes of the total generated radiation at 5.115 µm.
Taking into account all parameters influencing the experiment (room temperature instability, laser source performance, alignments of the experimental apparatus, etc.), with 5.93 W at 1064 nm and 19 mW at 1344 nm in front of the cavity (leading to about 0.9 W circulating in the cavity), the actually generated maximal output power at 5.115 µm was 105 µW.

4.2 The 12 W cw Nd:YAG pump laser

A high power Nd:YAG laser (Innolight / Laser Zentrum Hannover) is used as a pump laser for the difference frequency generation. The laser contains a master-slave system, achieving a total output power of 12 W at 1064 nm. The master laser (Mephisto 800 NE / Innolight) is a non-planar ring resonator (NPRO) with an output power of about 800 mW at 1064 nm and a short-term stability of 1 kHz / 100 ms. The slave laser is composed of a ring resonator consisting of two Nd:YAG laser crystals and two Brewster plates, each crystal pumped by a fibre-coupled diode laser with 17 W output power at 808 nm. The slave laser is coupled to the master laser via injection locking (Figure 4.13).
About 1 W of the output beam is used for second harmonic generation (SHG) to 532 nm in a nonlinear crystal (PPKTP) for the purpose of stabilizing the laser's frequency to a rovibrational transition of molecular iodine via Doppler-free saturation spectroscopy and possesses a residual spectral line width of 150 kHz. The remaining power of the radiation at 1064 nm before the crystal used for difference frequency generation (DFG) to 5.1 µm is about 6 W. A more detailed description of the Nd:YAG pump laser system can be found in [53].

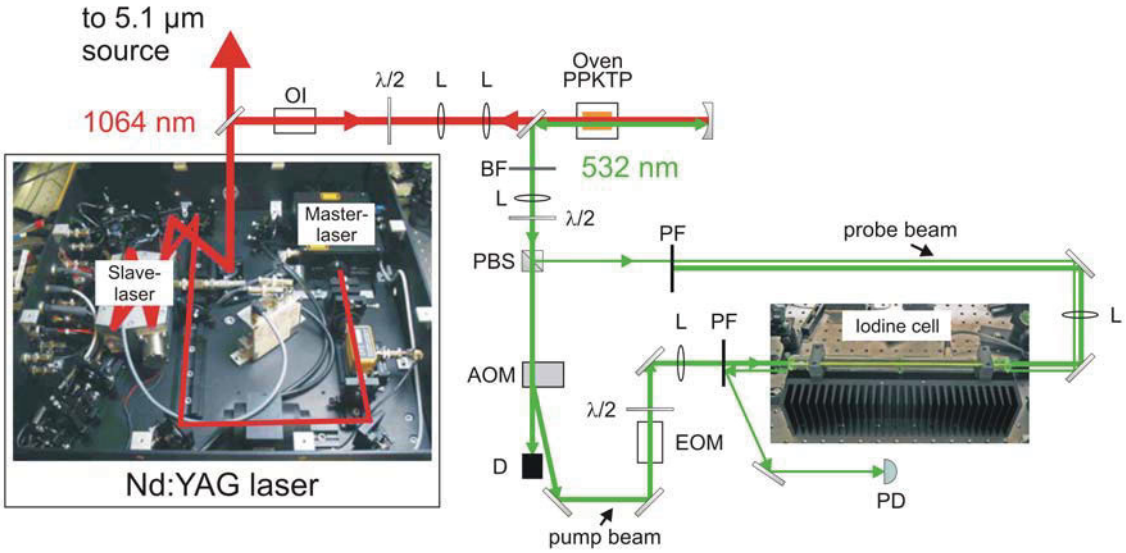

Figure 4.13 Schematic of the Nd:YAG laser source, stabilized to molecular iodine. A small fraction of the output beam is used for second harmonic generation in a PPKTP crystal, whereas the main power is sent to the 5.1 µm laser source (Figure 4.16). The 532 nm beam is split into two beam paths for Doppler-free saturation spectroscopy in an iodine cell. OI: optical isolator, λ/2: half wave plate, L: lens, PBS: polarizing beam splitter cube, BF: bandpass filter, PF: polarization filter, PD: photo detector, D: beam dump. (The two photos are taken from [53].)

4.3 The 1344 nm QD-ECDL source

The signal source for the difference frequency generation (DFG) is a home-built quantum dot external cavity diode laser (QD-ECDL) [54] (Innolume LD:GC-1320-CM200) in Littrow configuration with a free-running line width of 5 MHz. The laser is tunable in the range of 1316-1345 nm by turning the diffraction grating (Thorlabs GR13-1210). Due to operation of the laser diode (LD) at the (mechanical) tuning limit and in addition in a temperature regime around 60°C to obtain the necessary 1344 nm wavelength for the DFG, the total output power of the LD decreases to about 45 mW. In addition, the observation of optical feedback makes it necessary to operate the LD with the use of two optical isolators, one bulk isolator (Isowave I-13B-5) and a fibre-based isolator (Thorlabs IO-H-1310 APC), reaching a total isolation of -90 dB.

The laser head consists of the laser diode mounted in a brass holder, a short focal length lens in its brass holder and the diffraction grating mounted on an alpaca holder, themselves mounted on a larger base plate made from alpaca. The head is thermally stabilized with a thermistor and a peltier element at about 60 °C. The peltier element itself is mounted on a solid aluminum block which acts as a thermal reservoir, giving additional stability to the system. In order to protect the LD from air currents and acoustic noise, the laser head is surrounded by a three layer thermal- and acoustic shielding structure (see Figure 4.14 c)-e)). In combination with a home-built PID-controller, a mean thermal stability of about ± 2 mK could be reached at the working temperature of 60 °C.

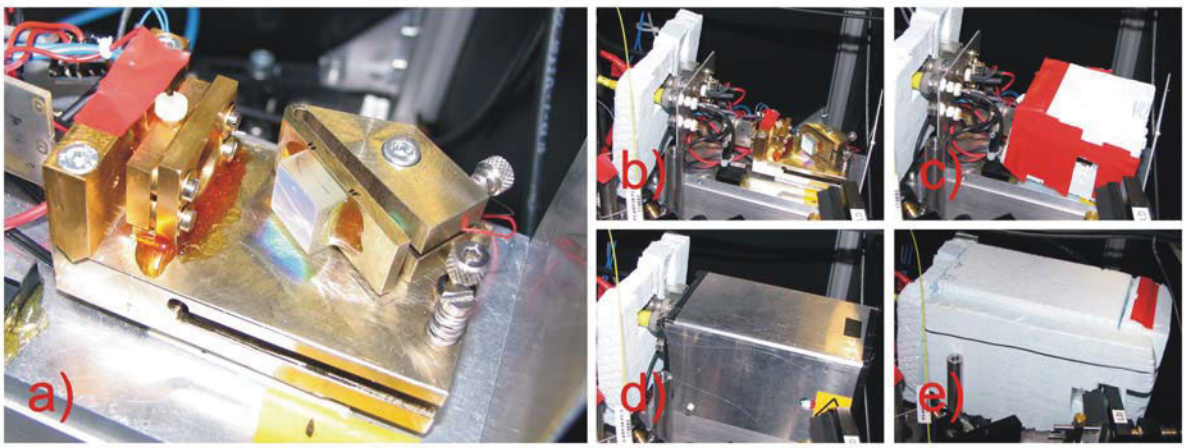

Figure 4.14 a) (from left to right) The laser diode and the short focal lens mounted in a brass holder, the grating, mounted on an alpaca holder. The base plate (alpaca) is thermally stabilized with a peltier element.
b)-e) different stages of thermal- and acoustic isolation.

4.4 Experimental setup

The realized experimental setup, containing the iodine stabilized Nd:YAG and the QD-ECDL source described in chapters 4.2 and 4.3, is illustrated in Figure 4.16. The beam leaving the QD-ECDL possesses, similar to other semiconductor laser diodes, an elliptical shape. For compensation, a prism pair is positioned directly after the laser's aperture. In addition to the optical isolation, the fibre-coupled optical isolator has the function of mode cleaning, leaving a well-shaped gaussian beam with a defined polarization. Using a polarizing beam splitter cube (PBS), a small fraction (ca. 3 mW) of the radiation at 1344 nm is transferred via an unstabilized PM single mode fibre to the frequency comb laboratory for stabilization of the QD-ECDL. The main portion, used for the difference frequency generation, is coupled into a PM single mode fibre based intensity modulator (Photline Technologies, MX1300-LN-10) for an additional frequency manipulation, further described in chapter 4.6. The lens (L1) of the fibre outcoupler is used as the focusing lens to obtain the necessary waist for most effective incoupling into the enhancement cavity. The additional half-wave plate in combination with the PBS guarantees a clean polarization in the $MgO:LiNbO_3$ crystal.

Enhancement cavity for 1344 nm

In order to most effectively use the low power of the QD-ECDL for the difference frequency generation process, an enhancement cavity, solely resonant for the QD-ECDL radiation has been set up. The layout as a singly-resonant cavity guarantees the ability to maintain a frequency tunable source at 5.1 µm. With a Nd:YAG source locked in frequency to iodine, the laser diode is the frequency-tunable source. In addition, due to the high output power of the Nd:YAG, it is not necessarily important to enhance this radiation with a cavity. The "bow-tie"-type ring resonator is stabilized in its length to the diode laser's frequency using the Pound-Drever-Hall method [55]. For this purpose a bias tee (Mini circuits ZFBT-282-1.5A+) is connected to the current input of the laser diode (see Figure 4.15).
The QD-ECDL laser light (frequency ν_o) is frequency / phase modulated with a frequency ν_m (here 23 MHz). Thereby, the resulting frequency spectrum contains the center frequency and two sidebands $\nu_o \pm \nu_m$. These sidebands possess the same amplitude but they are phase shifted by 180°. A high-frequency photodiode (PD) detects the reflected signal from the incoupling mirror of the cavity, as well as the "leakage beam", a part of the light traveling around in the resonator. In case of perfect resonance, the beat between the three waves becomes zero, because the sidebands are 180° out of phase and interfere destructively. Small changes in the amplitude's or phase relations between the three waves cause an amplitude modulation with a frequency ν_m in the detector signal. The mixer compares the modulation signal with the detector signal, extracting the part that is at the same frequency as the modulation signal.
Using a low pass filter, the resulting signal can be used as an error signal for the lock box. In order to hold the cavity on resonance to the laser diode's frequency, the resonator length is adjusted using a piezo element.

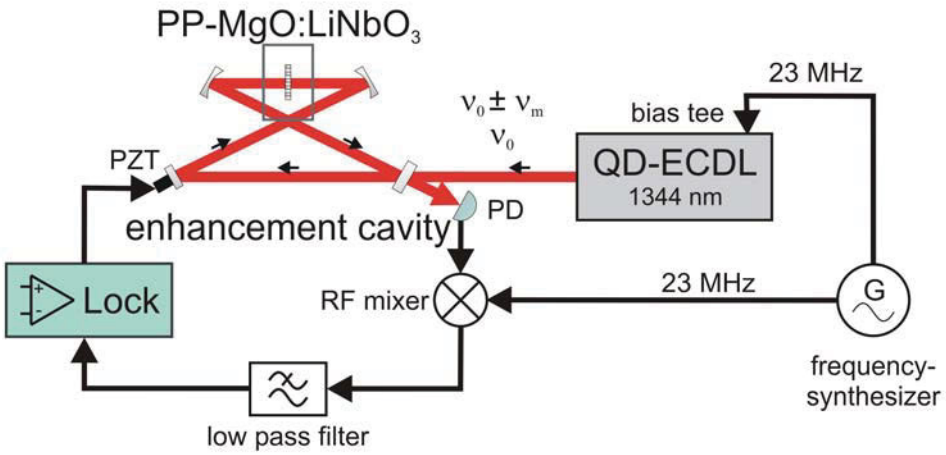

Figure 4.15 Simplified locking scheme of the Pound-Drever-Hall stabilization of the enhancement cavity to the QD-ECDL.

For the process of difference frequency generation, it is necessary to insert the particular nonlinear crystal within the cavity. With it, a finesse of 200 and an enhancement factor of up to 60 has been achieved, leading to a circulating power of 0.9 W at 1344 nm.

The iodine stabilized Nd:YAG (ca. 6 W) beam goes through a dichroitic mirror to transfer about 30 mW via an unstabilized PM single mode fibre to the frequency comb laboratory for frequency detection. The main beam is sent to the DFG setup and focused by lens L2 into the $MgO:LiNbO_3$ crystal, while the use of half-wave plates and a PBS guarantee the right polarization.

After traversing the crystal, the three beams are coupled out of the enhancement cavity using a specially-coated CaF_2 mirror. Despite having a transparency of only about 60 % for the generated 5.1 µm radiation, this coated mirror turned out as the best alternative compared to other intracavity solutions such as the positioning of an additional Germanium plate, which disturbs the cavity stability. Due to its transparency at 5.1 µm, all optics in the optical path were made from CaF_2. Using lens L3, the 5.1 µm radiation is collimated to reach the HD^+ experiment, located about 3.5 m away from the 5.1 µm source. To separate the three beams, a CaF_2 prism and a beam dump for the 1064 nm and 1344 nm beams were installed. For detection of the generated 5.1 µm radiation, a PC controlled motorized flip mirror (Thorlabs MFF001) and a sensitive fast pyroelectric IR detector (InfraTec LME-353) were mounted. This sensor is used in a lock-in detection scheme. For this reason, the 1064 nm beam passes through a chopper wheel before entering the DFG crystal.

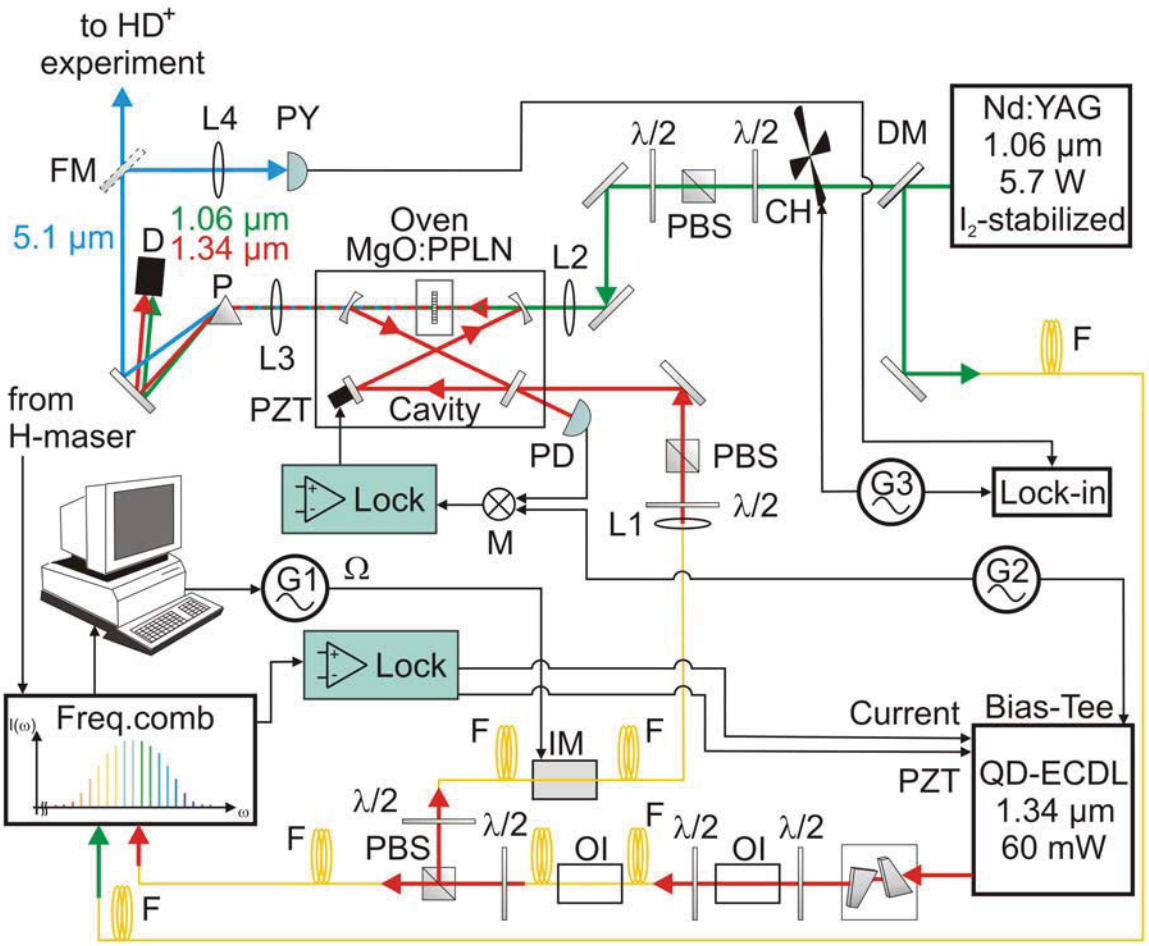

Figure 4.16 Schematic of the experimental setup of the 5.1 µm laser source. λ/2: half wave radiation plate, OI: optical isolator, F: single mode optical fibre, PBS: polarizing beam splitter cube, IM: intensity modulator, G: radio frequency oscillator, L: lens, PD: photo detector, PZT: piezo, P: prism, D: beam dump, PY: pyroelectric sensor, CH: chopper, DM: dichroitic mirror, FM: flip mirror.

The frequency comb (based on MenloSystems FC 8004) used for the stabilization of the QD-ECDL and the frequency detection of the 1064 nm laser, receives a 10 MHz reference signal from a hydrogen maser, located in the neighboring laboratory.

To avoid absorption losses at 5.1 µm due to moisture in air, test measurements have been performed. No absorption in air could be observed, confirming the distance to the next water line, consistent to the prediction according to the HITRAN database.

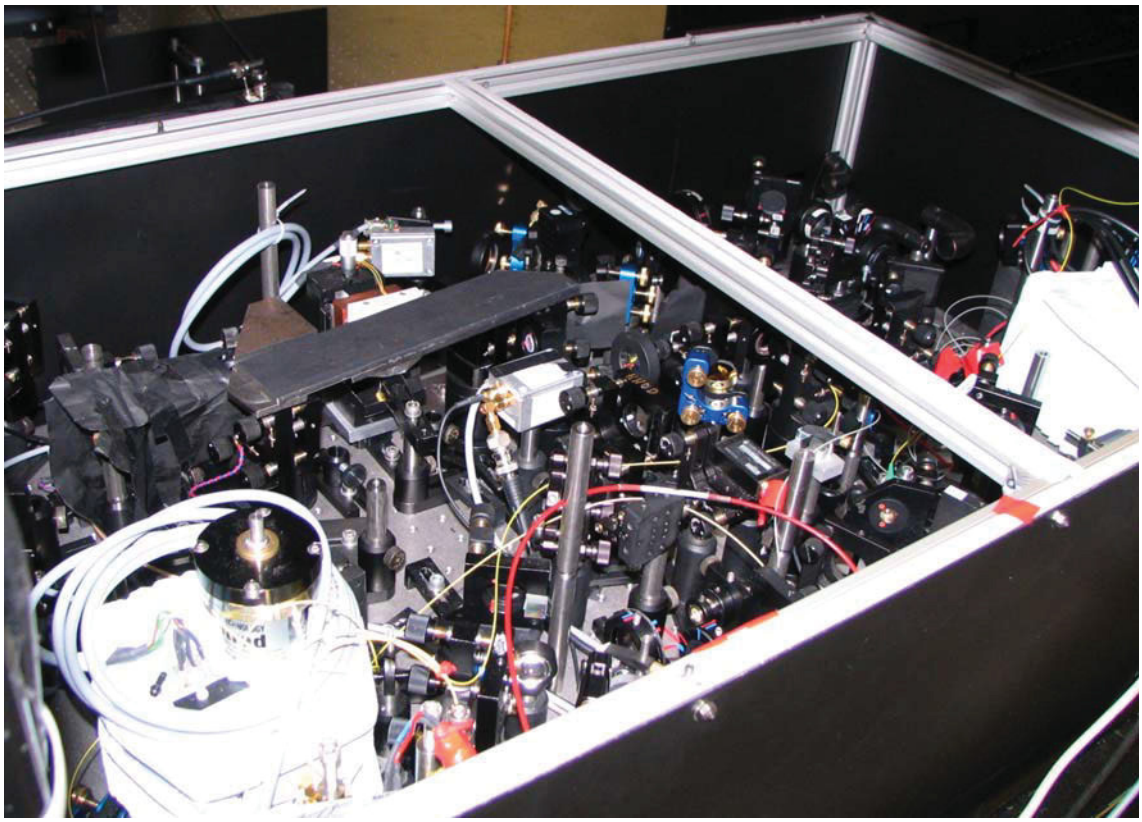

Figure 4.17 Photograph of the experimental setup of the 5.1 µm laser source. On the right hand side, the 1344 nm diode laser is seen, covered with a thermal insulation. In the left top, the resonator including the oven with the MgO:PPLN crystal can be seen, hidden beneath iron stabilization plates. The whole setup is surrounded by a metal box for thermal and acoustic isolation. The 1064 nm Nd:YAG laser beam enters the box from the right. The generated 5.1 µm radiation leaves the box to the left top (towards the spectroscopic experiment).

4.5 Frequency measurement and stabilization with the frequency comb

An optical frequency comb consists of a large number (10^5 – 10^6) of equidistant, narrow-band laser frequencies (modes) with a known position in the frequency domain (so called "comb needles"). This comb of frequencies f_n is given by $f_n = f_{CEO} + nf_{rep}$, with the repetition rate f_{rep} and an offset frequency f_{CEO} ("*carrier envelope offset frequency"*) (Figure 4.18).

The main component of the frequency comb used is a Ti:Saphire short pulse fs-laser (FEMTOLASERS FEMTOSOURCE scientific 2000), which produces the described comb structure and determines the mode spacing by its repetition rate f_{rep}. In addition, a photonic crystal fibre (PCF) broadens the primary frequency spectrum up to one octave and a nonlinear interferometer determines the offset frequency f_{CEO}.

In this work, a MenloSystems FC 8004 frequency comb, modified in-house, has been used. Its modes are spaced about 200 MHz with an emission range of 500 nm – 1600 nm [67].

The frequency comb itself is stabilized by locking the frequency comb's repetition rate f_{rep} and the carrier envelope frequency f_{CEO} to a GPS-disciplined H-maser.

For measurement of an unknown cw laser source, its radiation has to be heterodyned with the corresponding modes provided by the frequency comb. Unnecessary comb needles are blocked by suitable optical bandpass filters or via a diffraction grating in the overlap. Using a fast photodetector, the emerging ruff. beat note can be counted with a dead time free frequency counter. With this method, the optical frequency can be absolutely determined. See [67] for more detailed information.

For measurement of the frequency of the 5.1 µm source, both lasers are sent via an unstabilized single mode optical fibre link (ca. 70 m) to the frequency comb.

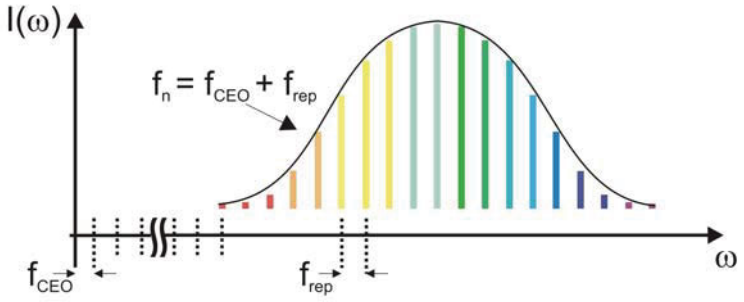

Figure 4.18 Schematic view of the emission spectrum ("comb needles") of the frequency comb.

4.5.1 Frequency read-out of the I_2-stabilized Nd:YAG laser

In contrast to the 1344 nm diode laser source, the Nd:YAG laser is already frequency-stabilized to a hyperfine transition in molecular iodine. Therefore, its contribution to the generated difference frequency at 5.1 µm can be determined by a frequency measurement with the frequency comb. As illustrated in Figure 4.19, the 1064 nm wave is transferred via an optical fibre to the frequency comb laboratory. For best overlap the beam shape is optimized by a telescope. The superposition with the filtered 1064 nm radiation provided by the frequency comb is done by a polarization beam splitter cube (PBS). After this PBS, the polarization of both beams is orthogonal, inhibiting the generation of a heterodyne beat note. Adjustment of a partial projection of the beams onto a common axis of a second rotatable PBS is done with a half wave plate for both beams. To support the mode superposition over a longer distance, the beams are coupled into a single mode optical fibre, which is connected to a fibre coupled fast photodetector (Thorlabs PDA10CF-EC).
Due to the frequency stabilization using the Pound-Drever-Hall method described in chapter 4.4, the signal in addition contains the modulation frequency at 29 MHz, which has to be suppressed with a 29 MHz notch filter. Using an optical spectrum analyzer, the peak of the displayed beat note is read out and transferred to a computer for further frequency analysis.

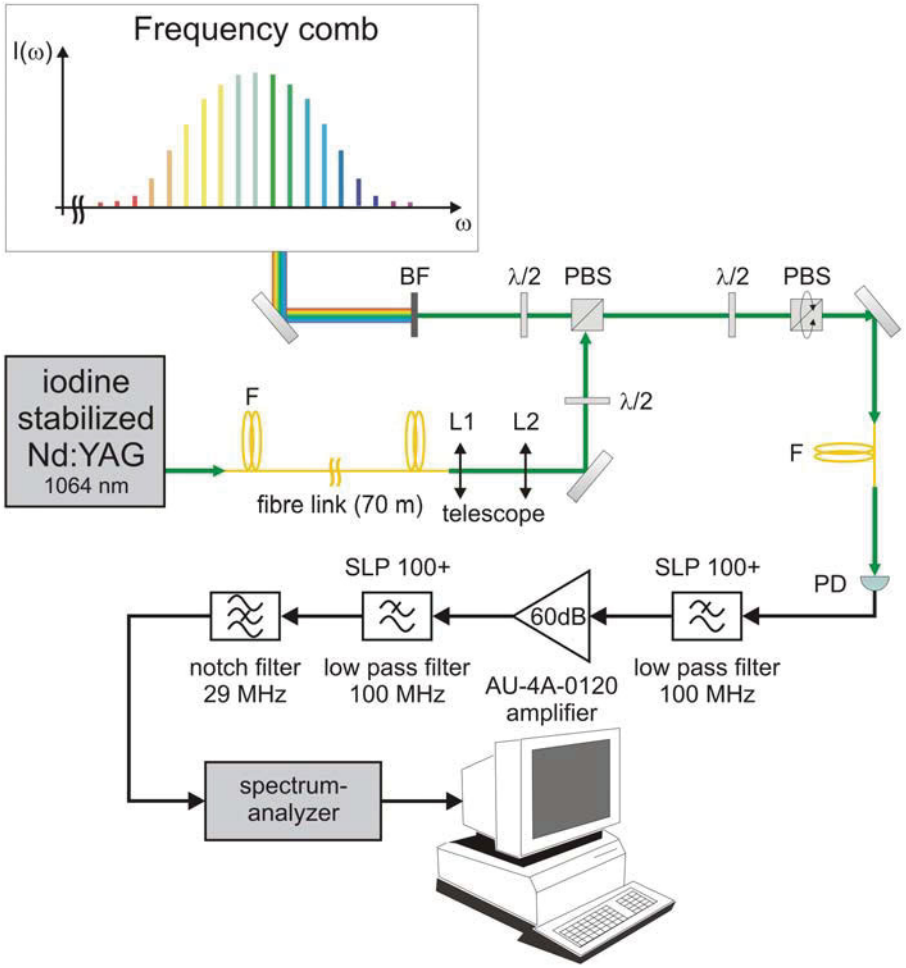

Figure 4.19 Schematic of the experimental setup for the frequency read-out of the iodine-stabilized Nd:YAG laser. BF: bandwidth filter 1064 nm, λ/2: half wave radiation plate, F: single mode optical fibre, PBS: polarizing beam splitter cube, L: lens, PD: photo detector.

4.5.2 Frequency stabilization of the QD-ECDL to the frequency comb

In comparison to the Nd:YAG laser, the frequency comb is not used only for the frequency measurement, but even more importantly, for the entire frequency stabilization process of the laser at 1344 nm and thus the frequency stability of the generated 5.1 µm radiation.
The QD-ECDL's radiation (ca. 3 mW) is transported to the frequency comb via an unstabilized optical fibre and is superposed with the radiation provided by the frequency comb, using a single mode optical fibre combiner (Laser 2000, WT-2P2C10A166, division ratio 10:90). Using a diffraction grating, frequency comb modes close to the 1344 nm wavelength can be isolated for improvement of the signal to noise ratio and sent onto a fast photodetector. The signal is amplified and filtered with suitable electronic components, illustrated in Figure 4.20. To observe the r. f. beat note, a spectrum analyzer (Agilent E4440A) is used. The signal is then split, on the one hand to send it to a tracking oscillator for

frequency measurement, on the other hand, to use it for the frequency stabilization of the QD-ECDL.
The tracking oscillator, phase-locked to the 20 – 35 dB input signal, improves the signal to noise ratio up to 60 dB for reliable counting by a frequency counter and further frequency analysis.

The signal used for the frequency stabilization of the QD-ECDL is centred around a frequency of 40 MHz, to combine the technical demands for the frequency stabilization described below with the operating range of the used tracking oscillator. For further processing a frequency of 24 MHz has been added to the signal, using a frequency generator and a mixer, to obtain a working point at 64 MHz. The beat note then is divided by 128 via a digital frequency divider. The application of this device, proposed by [68], is advantageous, because it strongly enlarges the capture range of the lock and enables one to stabilize even small signals. The output signal, a nearly-rectangular-shaped TTL signal, is transformed to a close-to-sinusoidal signal for the following frequency-to-voltage converter (Analog Devices, AD650) with a zero-crossing at 0.5 MHz, using a capacitor and a low pass filter. A subsequent lock box prepares the signal for the laser control input. The QD-ECDL is stabilized directly via the current input, using a ca. 70 m long BNC cable from the frequency comb laboratory to the ion trap laboratory.

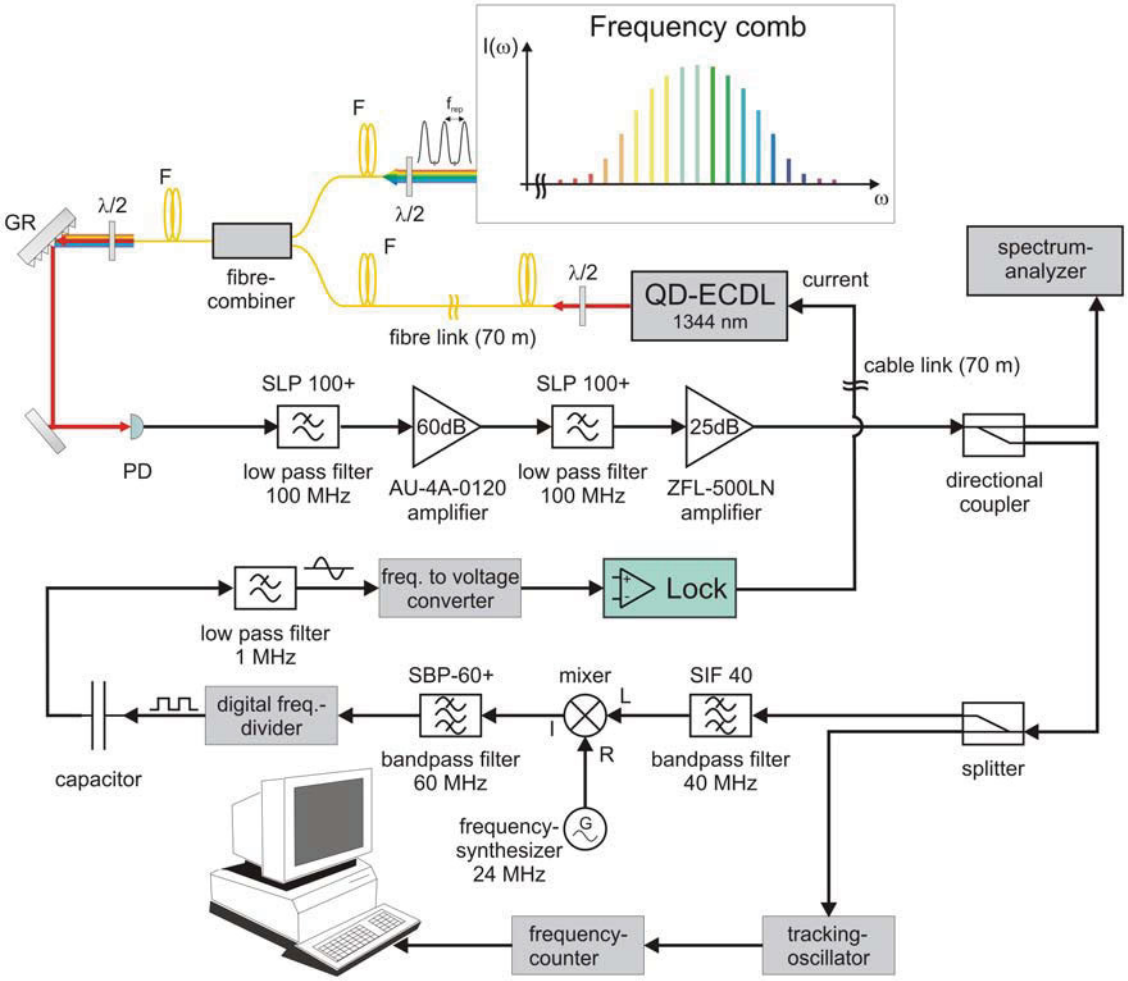

Figure 4.20 Schematic of the experimental setup for the frequency stabilization of the QD-ECDL laser to the frequency comb. F: single mode optical fibre, GR: diffraction grating, PD: photo detector.

Despite the characteristics of the lock box to obtain a stable lock additional work had to be invested to exclude possible noise sources, decreasing the lock quality. Therefore, great effort was concentrated in the in-house development of a low-noise QD-ECDL current driver (700 mA). Comparing it to available commercial sources, competitive technical performance could be achieved. According to noise measurements with a low noise amplifier (Stanford Research SR560) and a spectrum analyzer (Agilent E4440A), the contribution of the current source to the total frequency noise was estimated to be < 2 kHz on short time scales.
In addition, the temperature stability of the laser head, described in chapter 4.3, with its direct impact on the laser frequency had to be characterized. A mean thermal stability of about ± 2 mK could be reached at the working temperature of 60 °C.

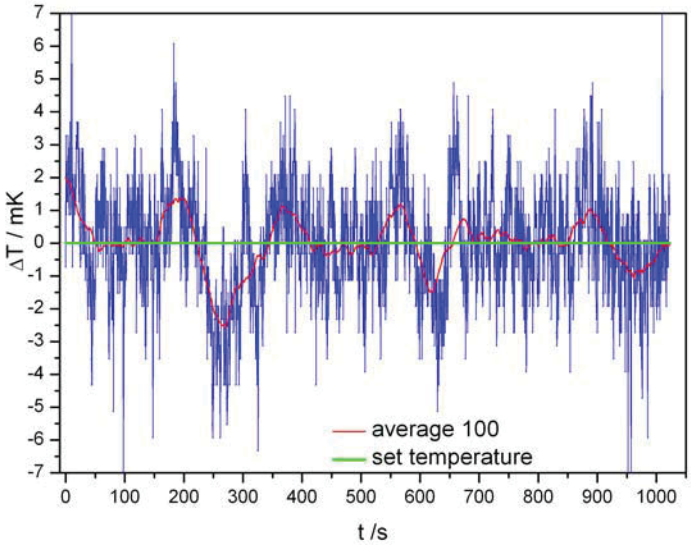

Figure 4.21 Plot of the typical (mean) temperature instability of the QD-ECDL around the set temperature (green line).

Noise measurements using a spectrum analyzer were carried out to characterize the long BNC-cable connection (ca. 70 m) used to deliver the control signal to the laser source. The external noise picked up by the cable has a direct influence on the current driving the 1344 nm laser. It was determined to cause a maximum frequency instability < 75 kHz.

4.5.3 Results of the frequency stabilization

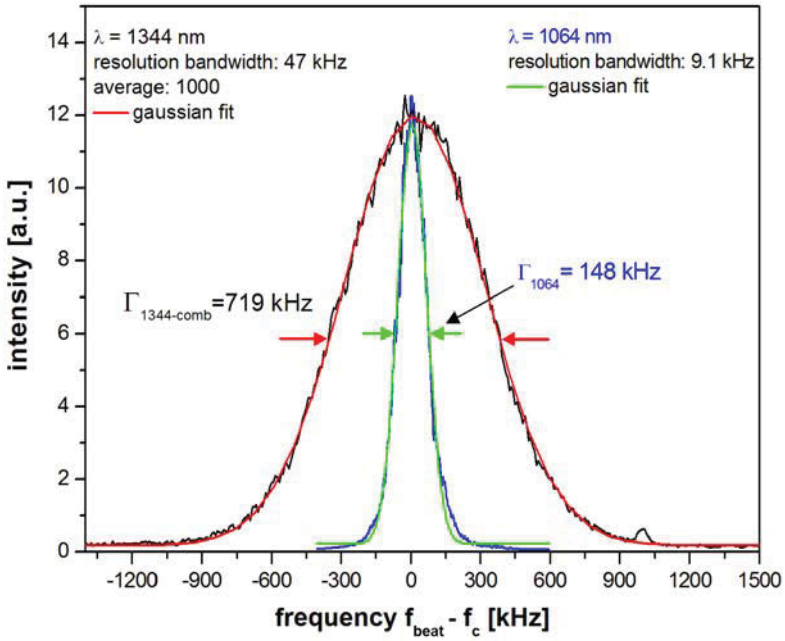

Figure 4.22 Beat notes of the 1344 nm QD-ECDL with the frequency comb and of the 1064 nm Nd:YAG laser with a narrow linewidth (10 kHz) Nd:YAG laser (ILF 100, Institute of Laser Physics, Novosibirsk).

According to Figure 4.22, the time-averaged beat between the stabilized QD-ECDL and the frequency comb is Gaussian, with a full-width at half maximum $\Gamma_{1344-comb} \approx 720$ kHz. The linewidth of the iodine-stabilized Nd:YAG laser is $\Gamma_{1064} \approx 150$ kHz, determined by heterodyning it with another independent narrow linewidth (10 kHz) Nd:YAG laser (ILF 100, Institute of Laser Physics, Novosibirsk). The linewidth of the comb modes is $\Gamma_{comb} \approx 272$ kHz, also determined by heterodyning with the same independent Nd:YAG laser. This linewidth is assumed to be the same at 1064 nm and at 1344 nm. Following these characteristics, the spectral width of the 5.1 µm radiation can be determined to

$$\Gamma_f = \left(\Gamma_{1064}^2 + \Gamma_{1344}^2\right)^{1/2} = \left(\Gamma_{1064}^2 + \Gamma_{1344-comb}^2 - \Gamma_{comb}^2\right)^{1/2} \simeq 0.68 \text{ MHz}.$$

According to the above described experimental approach of frequency stabilization and counting of the individual laser beat notes, all frequencies are logged together with the frequency comb's repetitions rate f_{rep} and the calculated DFG frequency using a computer program. The frequency traces of the stabilized Nd:YAG and the QD-ECDL sources, measured with the frequency comb, are illustrated in Figure 4.23. It is clearly seen that the frequency-instability of the iodine-stabilized Nd:YAG laser dominates the instability of the 5.1 µm radiation.

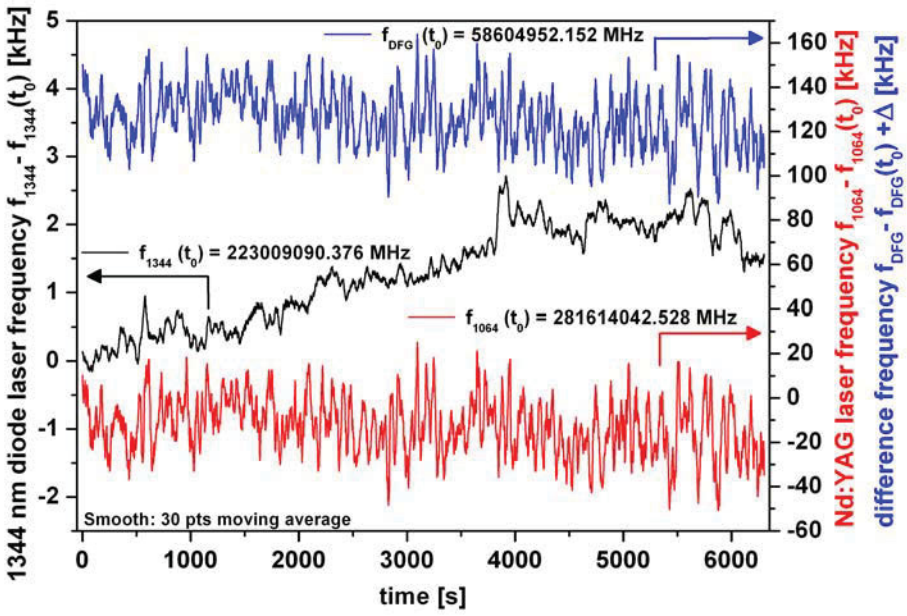

Figure 4.23 Frequency traces of the Nd:YAG laser and of the QD-ECDL, measured by the frequency comb over more than one hour and the corresponding frequency trace of the generated difference frequency at 5.1 µm. The DFG frequency trace has a frequency offset of $\Delta = +140$ kHz for the purpose of illustration. Note the different vertical scales.

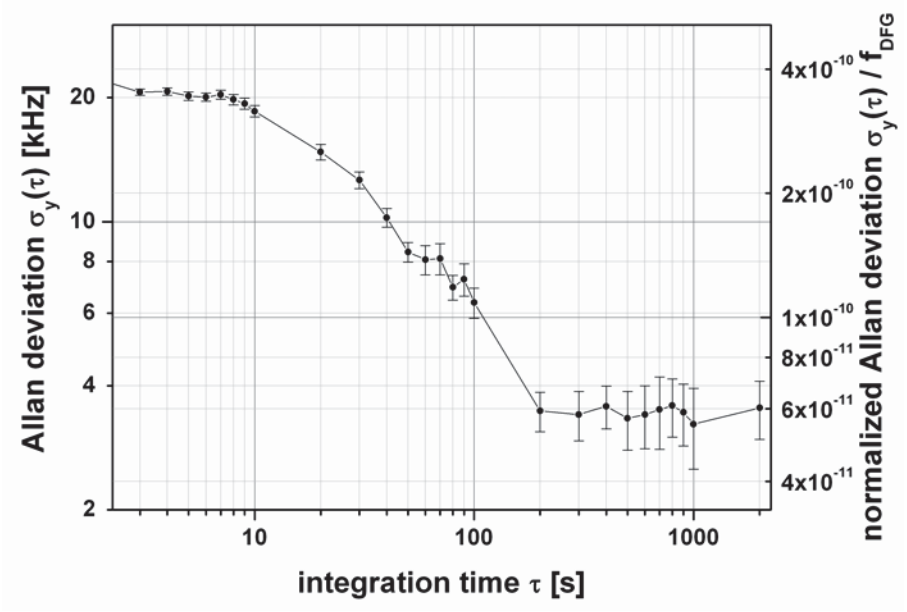

Figure 4.24 Allan deviation of the optical frequency of the generated 5.1 µm radiation. The values are computed from the calculated absolute frequency data of the 5.1 µm laser source, shown in Figure 4.23. The right axis shows the Allan deviation σ_y normalized to the optical frequency f_{DFG}.

The instability (Allan deviation) of the 5.1 µm radiation is shown in Figure 4.24. It is less than 25 kHz for short integration times τ, dropping to 4 kHz for an integration time above 200 s. Both the linewidth and the instability of the generated radiation at 5.1 µm are significantly lower than the 3 MHz Doppler width of the HD^+ hyperfine transitions (see chapter 7) studied in this work.

4.6 Frequency tuning of the 5 µm radiation

Tuning of the generated 5.1 µm radiation can be done by variation of the comb's repetition rate f_{rep} while all systems remain in lock. A typical frequency sweep of (only) 10 MHz/min could be achieved, depending on the comb's stability. Because this method was limited in stepsize and sometimes sensitive to the comb's performance, another more effective approach was developed.

Once locked to the frequency comb, the QD-ECDL's frequency, and thus the generated frequency of the 5.1 µm radiation can be tuned using a integrated-optic intensity modulator (Photline Technologies, MX1300-LN-10). This $LiNbO_3$-based low-insertion-loss intensity modulator is driven by a signal generator (HP 8675 A) with a r. f. frequency Ω and generates two symmetric sidebands $\left(f_{1344} \pm \Omega\right)$ with respect to the carrier frequency f_{1344}, which is kept fixed (stabilized to the comb). For sufficiently high r. f. strength, the carrier is suppressed and its power (nearly) completely transferred to the sidebands. The enhancement cavity is locked to a designated sideband, e. g. $\left(f_{1344} - \Omega\right)$ via the Pound-Drever-Hall technique. The

generated 5.1 µm radiation $f_{1064} - (f_{1344} - \Omega)$ then has a frequency offset "+ Ω " with respect to the frequency $f_{1064} - f_{1344}$ measured by the comb. By sweeping the r. f. frequency Ω of the intensity modulator over time, the lock system of the enhancement cavity follows the sweep, causing a (reverse) frequency sweep of the generated 5.1 µm radiation. Figure 4.25 shows a typical frequency sweep of the 5.1 µm radiation by use of the intensity modulator.

The maximum sweep range is $|\Delta\Omega| = 15 - 475$ MHz (for each sideband). The maximum frequency tuning rate is 35 MHz/s. The output power obtained was about 2.2 µW at 5.1 µm. The observed minor power changes are caused by small, modulation-frequency-dependent, fluctuations of the modulation depth, which affect the total power coupled into enhancement cavity. To ensure locking of the cavity to the desired sideband and therefore knowledge of the exact frequency generated at 5.1 µm, the applied voltage on the piezo of the enhancement cavity is constantly monitored. Choosing the negative sideband "- Ω " as described, the corresponding piezo voltage decreases with increasing modulation frequency showing the opposite behaviour for the positive sideband "+ Ω ".

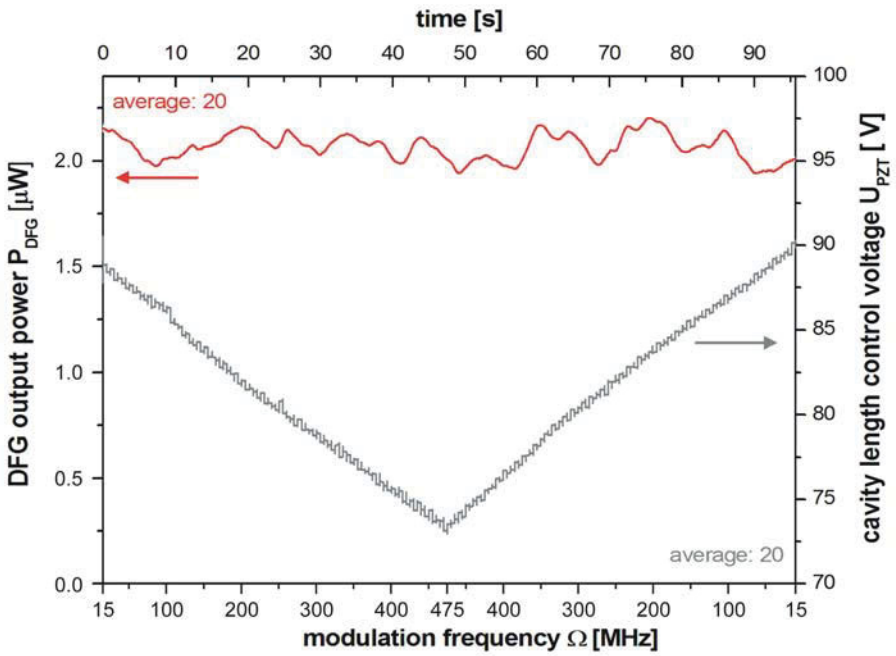

Figure 4.25 DFG output power and the corresponding monitored piezo voltage of the enhancement cavity during a typical (single) frequency sweep with the intensity modulator. Here, the frequency has been ramped back and forth, changing the modulation frequency Ω = 15 MHz to 475 MHz.

5 Experimental setup and procedure

Performing spectroscopy on the HD^+ molecular ion represents the last of many steps necessary for the preparation of the system for measurement. A short overview will be given in this chapter, leading to a detailed discussion of the performed hyperfine-structure-resolving spectroscopy of HD^+.

5.1 Trapping and cooling

The experiment must be executed under ultra-high vacuum (UHV) conditions (2×10^{-11} mbar) in order to strongly suppress collisions of the particles with the background gas and to prevent chemical reactions involving the ions. Storage and cooling of the ion species is done with a linear quadrupole ion trap (see chapter 3.1), positioned in the center of the UHV-chamber (Figure 5.1). The Beryllium oven in the UHV chamber, is situated beneath the ion trap, close to the center. The Beryllium atoms are sublimated from the oven and electron-impact-ionized in-situ by an electron gun, aimed at the trap center. Once ionized, the particles are trapped in the quadrupole ion trap. During the ionization process, the production of ions is not restricted to Beryllium atoms, but takes place as well for residual gas molecules, consisting mainly of the air constituents N_2, O_2 and H_2. According to chapter 3, the effective trap potential is depends on the charge-to-mass ratio; therefore residual gas ions (with masses similar to Be^+) can also be trapped to a certain extent. The process of trap loading takes about 1-2 minutes, producing a "hot" cloud of Be^+ and residual gas ions.
Already during the loading process, the cooling laser at 313 nm is introduced to the ion trap and frequency-detuned for most effective Doppler cooling, as described in chapter 3. The fluorescence signal, observed following the scattering of photons by Be^+ ions while traversing the resonance frequency of the (moving) ion, can be registered with a photomultiplier and a charge-coupled-device (CCD) camera mounted outside the UHV trap behind fused silica viewports. By contrast to the Be^+ ions, the cooling laser is off-resonance for the residual ions, which appears as dark areas in the cloud, showing no fluorescence signal. Because the presence of residual gas ions in the trap inhibits the formation of a Beryllium Coulomb crystal, it is necessary to remove the residual gas ions from the trap. As described in chapter 3.1, the trap can be employed as a mass-filter. Variation of the amplitude of the static electric field U_{DC} leads to a change of the stability parameter a (see equation (3.5)). Thus the mass range of ions which are trapped can be influenced, causing a selective loss of ions and a "cleaning" of the Be^+-cloud. Due to more-effective cooling, a Coulomb crystal finally forms after several repetitions of the cleaning process.

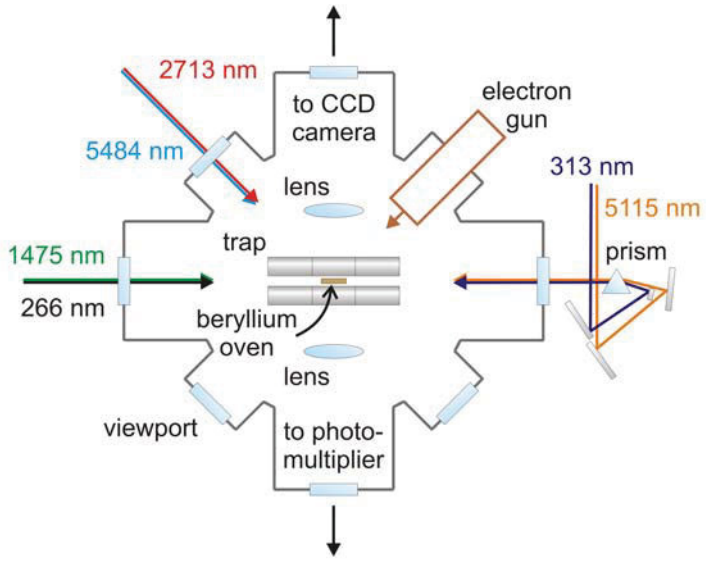

Figure 5.1 Illustration of the experimental setup. The linear quadrupole trap is centered in the UHV chamber. The beryllium oven is underneath the trap, the CCD camera and the photomultiplier are behind viewports (fused silica) outside the chamber. The cooling and spectroscopy lasers enter the UHV chamber through MgF_2 viewports. The polarization of the 5.1µm beam is orthogonal to the surface of the optical table.

After production of a "clean" Beryllium Coulomb crystal, a small amount of HD gas is lead into the trap region through a leak valve and ionized in-situ by the electron beam of the electron gun. The HD^+ ions get trapped and are embedded within the Be^+ crystal, as shown in Figure 3.10,and are cooled via sympathetic cooling (see chapter 3.2.1).

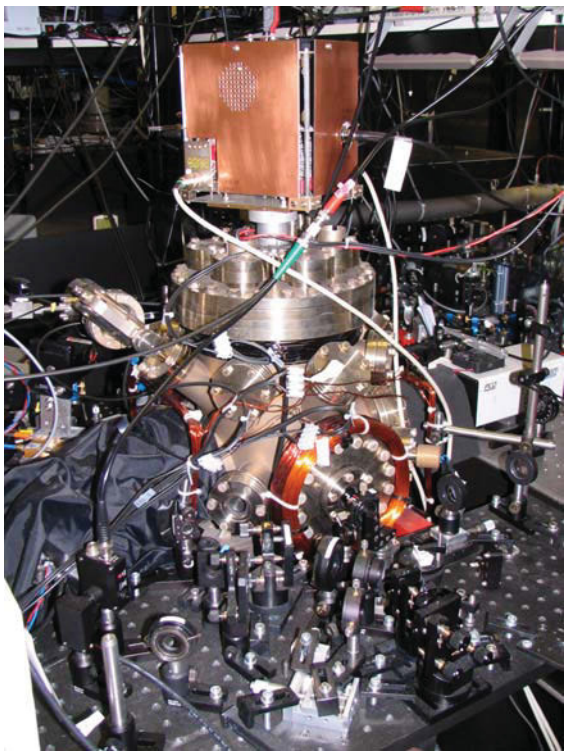

Figure 5.2 Photograph of the UHV chamber in the experimental setup. The 313 nm and 5.1 µm waves enter the chamber through the viewport, surrounded by magnetic coils in front. The CCD camera is seen on the right hand side (white box), the photomultiplier (left) is covered with black cloth.

Secular excitation

For detection of the sympathetically cooled ions, one takes advantage of the induced transfer of kinetic energy from the micromotion to the secular motion, described in chapter 3.1.3. Using an additional electrode (plate) perpendicular to the trap axis and applying a small AC voltage, the ions' motion can be shifted out of phase with the trap r. f. field. Thus the ions gain new kinetic energy in form of micromotion, which is then be transferred to the secular motion (see chapter 3.1.3). This energy transfer becomes observable due to a resultant change in the fluorescence signal.

Quantitatively, the secular excitation leads to an additional heating of the Coulomb crystal with a heating rate Γ_N which is proportional to the number N of the HD^+ ions in the trap. In steady state, the cooling rate and the heating rate of the crystal are in balance $\Gamma_c = \Gamma_h$.

To first approximation, below saturation the cooling rate Γ_c is proportional to the Be^+ fluorescence rate Γ_f. When the secular excitation is switched off, the fluorescence rate can therefore be expressed by:

$$\Gamma_f \sim \Gamma_c = \Gamma_h = \Gamma_0. \qquad \textbf{(5.1)}$$

Here Γ_0 represents the background heating rate independent of the number of HD^+ ions.

Turning on the secular excitation yields:

$$\Gamma_f \sim \Gamma_c = \Gamma_h = \Gamma_0 + \Gamma_N. \qquad \textbf{(5.2)}$$

(1+1'+1'')-Resonance-enhanced-multiphoton-dissociation (REMPD)

HD^+ possesses only small fluorescence rates, which makes it unusable for spectroscopic applications. The (1+1')-resonance-enhanced-multiphoton-dissociation (REMPD) method [52], although destructive, was implemented to enable work with even these low-fluorescence signals. In combination with the 5.1 μm spectroscopy source, the method can be considered as a (1+1'+1'')-REMPD. The method is illustrated in Figure 5.3.

The molecules are excited with the 5.1 μm spectroscopy laser $(\upsilon = 0, L = 0) \rightarrow (\upsilon' = 1, L' = 1)$ and simultaneously with the 1475 nm diode laser (ca. 1 mW), driving the $(\upsilon' = 1, L' = 1) \rightarrow (\upsilon'' = 5, L'' = 2)$ overtone transition. An additional 266 nm laser (25-30 mW) dissociates the molecules from the latter level.

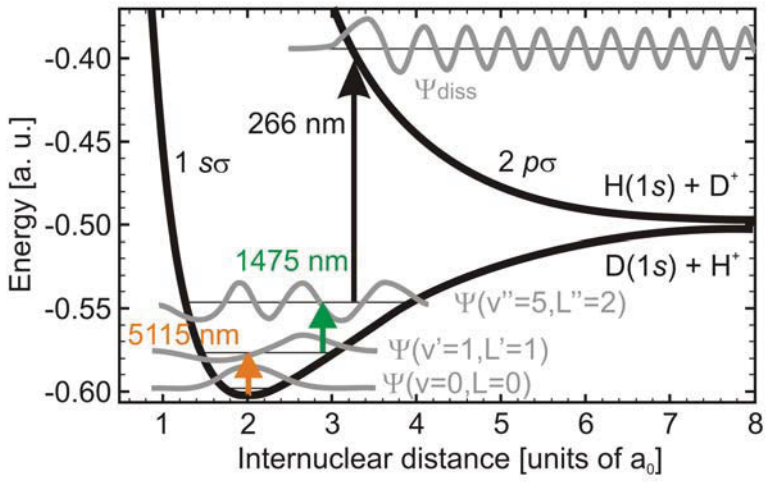

Figure 5.3 Illustration of the (1+1'+1'') REMPD spectroscopy of HD^+ ions.

5.2 Data acquisition and analysis

In a single spectroscopic measurement run, the fractional population of HD^+ is detected by probing the number of molecules in the trap before and after the state-selective photodissociation. According to equations (5.1) and (5.2) the difference between the Be^+ fluorescence rates (secular excitation on / off) scales with $\Delta\Gamma \sim N$. Therefore the determination of $\Delta\Gamma$ gives information on the fraction that is addressed by the 5.1 µm spectrometer laser, of the population initially present in the $(\upsilon = 0, L = 0)$ state:

$$S_J = \frac{\langle \Delta\Gamma_1 \rangle - \langle \Delta\Gamma_2 \rangle}{\langle \Delta\Gamma_1 \rangle} = 1 - \frac{N_2}{N_1}. \qquad \textbf{(5.3)}$$

Here, the brackets express the change of fluorescence over the time of secular excitation t_s, whereas the indices 1 and 2 describe the situation before and after the REMPD process. In addition, it has to be taken into consideration that S_J also includes all ions lost out of the trap without being influenced by the REMPD. Hence, the background loss rate S_B has to be determined (simply by blocking all REMPD lasers) and subtracted from S_J, giving the background corrected detection signal:

$$\langle S_{Jb} \rangle = \langle S_J \rangle - \langle S_b \rangle. \qquad \textbf{(5.4)}$$

Figure 5.4 shows the recorded signals of an actual spectroscopic measurement run, producing a single data point in the spectrum displayed in chapter 6.2, Figure 6.2.

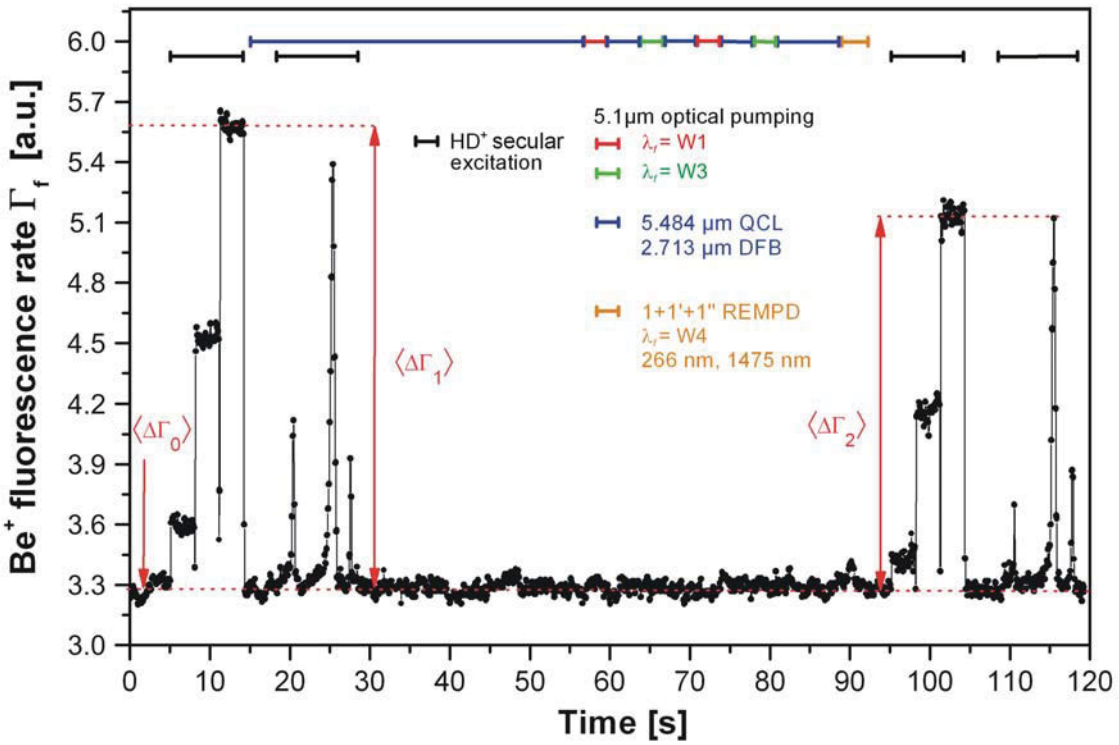

Figure 5.4 Illustration of a typical REMPD spectroscopic measurement run. For the purpose of illustration, the time-resolved irradiation of the laser sources for rotational cooling, the laser used for quantum state preparation (frequencies W1, W3), followed by the spectroscopy at W4 and the REMPD process, has been included on top of the detected signals.

The typical procedure of a spectroscopic measurement run starts with the loading of the trap with Beryllium, the cleaning process and the injection of HD gas, leading to a Be^+/HD^+ crystal, described in chapter 5.1. This procedure takes ca. 1 - 2 min and the loading of HD^+ ions has to be repeated before each spectroscopic measurement run, due to the destructive REMPD process, which decreases the number of ions too strongly for a repetition of measurement runs.

The spectroscopy run itself begins with the determination of the number of HD^+ ions before the spectroscopy $\langle\Gamma_1\rangle$ as well as the background level $\langle\Gamma_0\rangle$, by a continuous HD^+ secular excitation (10 s). This is followed by a discrete secular excitation sequence (10 s), for plausibility tests, which can reveal technical problems and discrepancies. Following the continuous secular excitation sequence, the rotational cooling by the $\lambda_p = 5484$ nm quantum cascade laser, driving the dipole allowed $(0,2) \rightarrow (1,1)$ transition (40 s), is switched on and the $\lambda_p' = 2713$ nm diode laser is used to drive the $(0,1) \rightarrow (0,2)$ transition (40 s).
Following the spectroscopy with the $\lambda_f = 5115$ nm laser (see chapter 6) tuned to the W4 line for 3 s, the (1+1'+1'') REMPD sequence (3 s) is initialized.

Finally, the number of HD^+ ions after the REMPD sequence $\langle \Gamma_2 \rangle$ is determined by a continuous HD^+ secular excitation (10 s), followed by a discrete secular excitation sequence (10 s).

The total time to record a single data point including the (regular) reloading of HD^+ into the Be^+ crystal, presented above, is about 4 - 5 min. A whole spectrum like the one presented in (Figure 6.1) typically consists of 10 – 15 data points per frequency (exceeding 25 for some measurements) due to statistical reasons, requiring in total one measurement day per single hyperfine transition.

6 Hyperfine state preparation

6.1 Quantum state preparation

As shown in chapter 2.2, the HD^+ molecular ion possesses 4 (singlet) hyperfine states in zero magnetic field in the $L=0$ state. For $L=1$ the number of hyperfine states increases to 10 (4 multiplets), see Figure 2.2. The approach used in this work is based on one-photon laser excitation of the fundamental vibrational transition $(\upsilon=0, L=0)\rightarrow(\upsilon'=1, L'=1)$ at $\lambda_f = 5115$ nm. Diatomic molecules posses in general low transition frequencies $(\lambda_f > 2.5\ \mu\text{m})$. The low kinetic energy $k_B T_{\text{sec}}$ achievable via sympathetic cooling, yields a Doppler broadening $\Delta\nu_D$ of the transitions which is smaller than many line spacings (see Figure 2.5) enabling selective addressing of some hyperfine states. In the case of HD^+, the typical values are: $\lambda_f = 5115$ nm, $T_{\text{sec}} \simeq 10$ mK, $\Delta\nu_D \simeq 3$ MHz. Due to the excitation of weak transitions, which violate the approximate selection rules $(\Delta F = 0,\ \Delta S = 0)$, it is possible to selectively address all hyperfine states, as the frequency spacing is larger for these transitions.

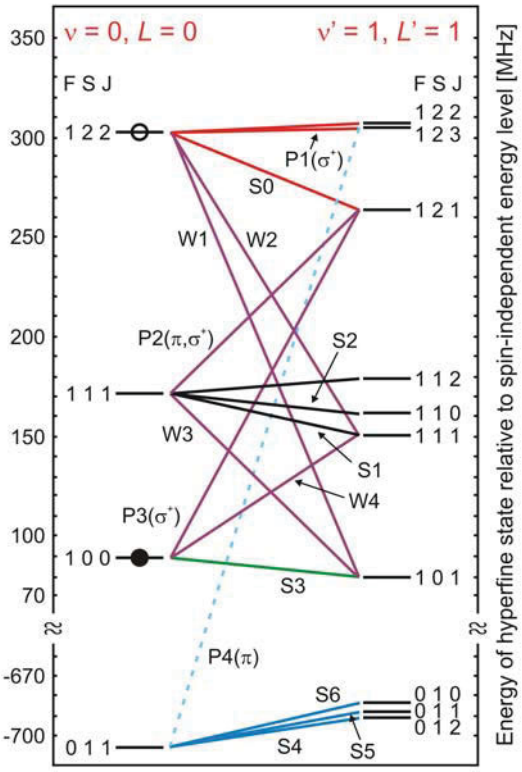

Figure 6.1 Energy diagram of the hyperfine states of the HD^+ molecular ion and the main electric dipole transitions in zero magnetic field. Transitions not changing the quantum numbers F, S are relatively strong and marked in red, black, green and blue. Transitions changing one or both quantum numbers are indicated in purple [46]. Very weak transitions are neglected, except for P4 (dashed). S0, S1, S2, S3, S4, S5, S6, W1, W2, W4, P2 ("S": strong, "W": weak, "P": pump) are the transitions investigated in this work. All were observed, except for S4. W1 and W3 are transitions used for population transfer from the hyperfine states $(\upsilon = 0, L = 0, F = 1, S = 2, J = 2, J_z)$ (empty circle) and $(0,0,1,1,1,J_z')$ into the hyperfine state $(0,0,1,0,0,J_z'')$ (filled circle).

In a typical spectroscopy run, the $\lambda_f = 5115$ nm laser spectrometer (referenced to an atomic frequency standard, see chapter 4) is precisely tuned to an individual transition.
To prove this selective excitation, we detect (without hyperfine selectivity) the population of the goal vibrational level $(\upsilon' = 1, L' = 1)$ via a (1+1') resonance-enhanced-multi-photon-dissociation (REMPD) process [52]. Together with the spectroscopy source, this represents a (1+1'+1'') REMPD, described in more detail together with the experimental procedure in chapter 5.2. The observed reduction of the HD^+ number by the REMPD process represents the spectroscopic signal.

6.2 Demonstration of hyperfine state manipulation

We could demonstrate the manipulation of individual hyperfine states of the molecule by selective optical pumping of populations into a goal state. The chosen goal state $(\upsilon = 0, L = 0, F = 1, S = 0, J = 0, J_z = 0)$ (marked with a filled circle in Figure 6.1) is non-degenerate $(J = 0)$ (with angular projection $(J_z = 0)$) and therefore represents a single quantum state.

The measurement sequence starts with simultaneous rotational cooling at $\lambda_p = 5484$ nm and $\lambda_p' = 2713$ nm. The sequence of *optical pumping* is then performed twice: The $\lambda_f = 5115$ nm spectrometer laser is precisely tuned to the W1 line for 3 s, followed by a re-pumping at λ_p, λ_p' for 5 s, and λ_f tuned to the line W3 for 3 s. A subsequent final 10 s rotational re-pumping at λ_p, λ_p' is performed before the spectroscopic excitation at λ_f tuned to the W4 line for 3 s. Both W1 and W3 transitions with the initial states $(0,0,1,2,2,J_z)$ and $(0,0,1,1,1,J_z')$ (without J_z selectivity) address the same hyperfine state $(1,1,1,0,1,J_z'')$. This state has a dominant spontaneous decay to the goal state $(0,0,1,0,0,J_z = 0)$, represented by line S3 (Figure 6.1).

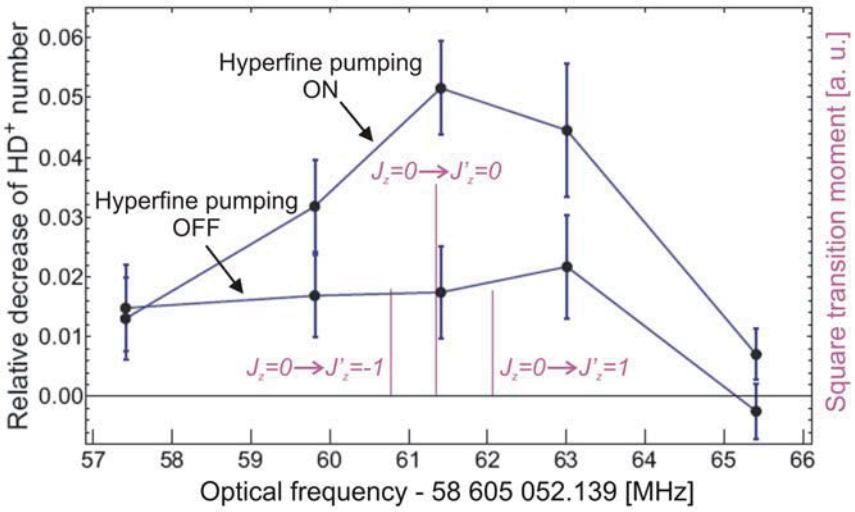

Figure 6.2 Experimental data for transition W4 taken by optical pumping between hyperfine states of the ground ro-vibrational level $(\upsilon = 0, L = 0)$. Transition W4 represents an excitation from a single quantum state $(\upsilon = 0, L = 0, F = 1, S = 0, J = 0, J_z = 0)$. The presented data points were taken alternating between the case with preceding optical pumping (upper line) and without (lower line). The zero level represents a blocked 5.115 nm spectroscopy laser source. In addition, the presented stick spectrum represents the theoretical transition frequencies and strengths in a 0.6 G magnetic field with radiation polarized at 45 degrees to the magnetic field. Here, the central stick shows the $J_z = 0 \rightarrow J_z' = 0$ Zeeman component, and the left and right sticks the $J_z = 0 \rightarrow J_z' = -1, +1$ components, respectively. The central component is shifted -0.05 MHz at 0.8 G relative to the zero-field frequency due to the quadratic Zeeman shift.

The line W4 presented in Figure 6.2 could only be observed in our experiment after the optical pumping process by excitation of lines W1 and W3, since the population in the lower hyperfine state is too low, giving clear evidence that the hyperfine state preparation took place.

It should be emphasized, that this presented technique could form a basis for full quantum state preparation of diatomic molecular ions (single or ensembles) and might be applied to many other diatomic atoms.

7 Results

7.1 Hyperfine resolved spectrum

In order to expand the operational range, the spectroscopy source must be customized to the individual transition to be investigated. Examples are power variation of the 5.1 µm spectrometer laser to prevent saturation, and adjustment of the necessary r. f. modulation frequency of the intensity modulator, described in chapter 4.6, to reach the necessary translation frequency. In addition, the measurement procedure itself was improved over the many measurement days, leading to transition-adapted procedures.
The achieved hyperfine resolved spectrum, which to our knowledge represents the highest-resolution optical spectrum of any molecular ion so far [89], is illustrated in Figure 7.1 and discussed in the following.

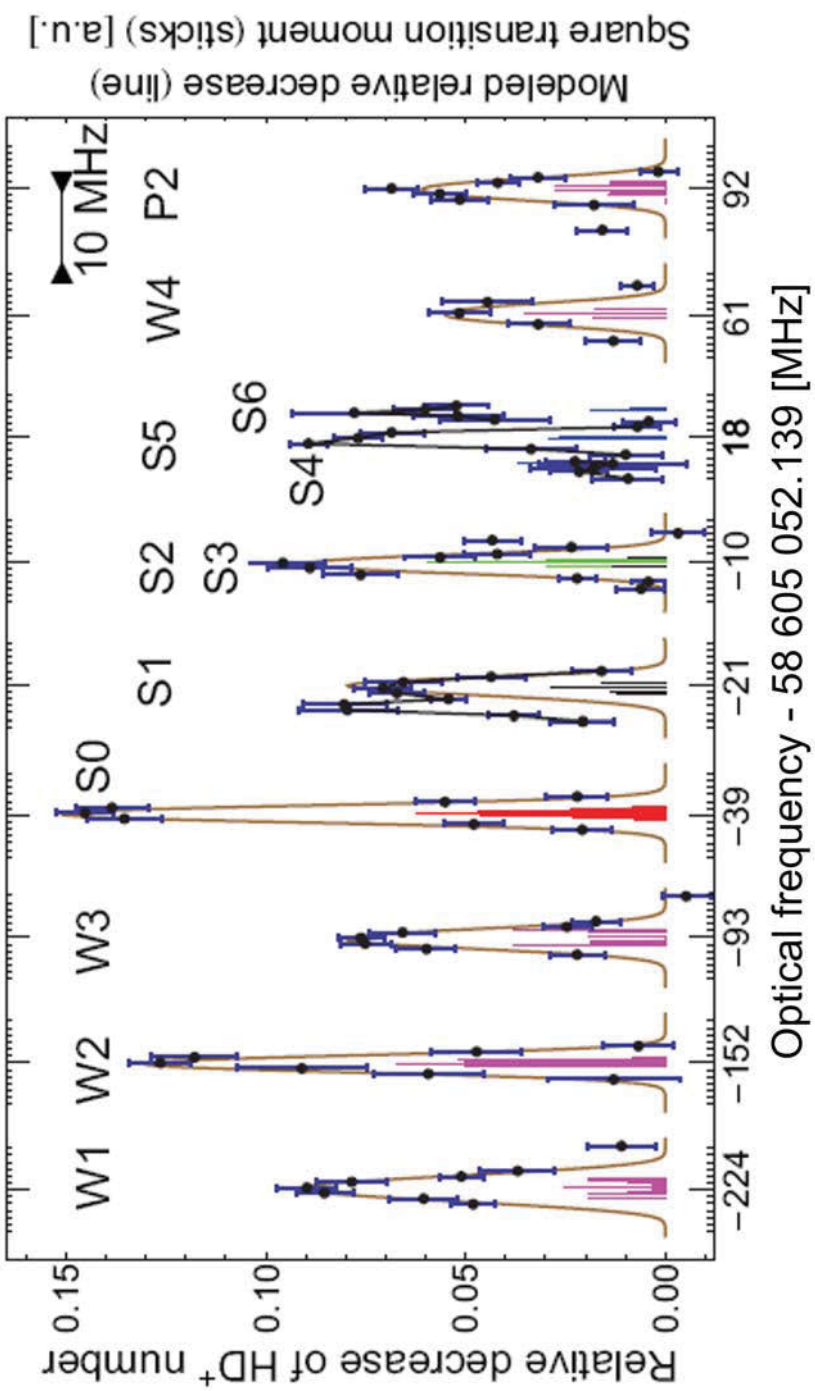

Figure 7.1 Measured hyperfine transitions of the $(\upsilon = 0, L = 0) \rightarrow (\upsilon' = 1, L' = 1)$ fundamental transition in cold trapped HD^+ ions. The abscissa for the data points is the detuning of the optical frequency of the $\lambda_f = 5115$ nm spectroscopy source relative to the reference frequency ("spin-independent" transition frequency $f_0 = 58\ 605\ 052.139$ MHz). The stick spectrum refers to the theoretically computed transition frequency, minor abscissa tick spacing is 1 MHz. The product of the effective intensity times the irradiation duration of the 5.1 µm radiation varied from line to line and had to be adjusted to avoid saturation. The black lines (S1, S4-6) connect the data points. Brown lines are the fitted lineshapes for a temperature of 9.5 mK, and an averaged magnetic field of 0.8 G, assuming exciting radiation polarized 45 degrees to the magnetic field. The scaling differs by factors for illustration reasons. The notation and colour code of the transitions corresponds to Figure 6.1 (page 84).

With a spectroscopy source linewidth of 0.7 MHz (chapter 4.5.2), the frequency steps were typically set to 0.8 MHz when scanning through the lines. Due to the above-mentioned 3 minute data recording time per data point, only a limited number of data points could be recorded within one day of measurements, easily exceeding 150-200 measurements for one hyperfine transmission line presented above. Alignment of the 5.1 µm laser with the ion crystal changed from day to day (e.g. due to laboratory room temperature fluctuations) and had to be re-aligned before each measurement run as well as adjusted in its power coupled into the ion trap.

The relative decay rate recorded as the spectroscopy signal at a given frequency possesses a typical standard deviation (of the data, not of the mean) of 0.02. It is mainly due to the low number of HD^+ ions in the ion crystal (a few hundred) and the relatively-low population in a particular hyperfine state. According to the effective rotational cooling at $\lambda_p = 5484$ nm (see chapter 3.4), the population of a hyperfine state is proportional to $(0.6-0.75)\,p_J$, where $p_j = (2J+1)/12$ in a particular hyperfine state J, for L=0. This population is further reduced during the REMPD sequence $(\lambda_p, \lambda_p'$ lasers turned off$)$ due to the competing black-body-radiation-driven excitation $(\upsilon = 0, L = 0) \rightarrow (0,1)$. Due to the overall small ion number and therefore the small number of ions prepared into a defined hyperfine state, a fraction of which are excited and dissociated, significant statistical fluctuations of the recorded number of ions are present. The maximum observed dissociated fractions (using high intensity on resonance) do not exceed p_J, consistent with the above assumption. Probing the S0 transition, for example, revealed ion number reductions of (19.4 ± 1.4%) and (16.4 ± 2.8%) for the lines S2 and S3 respectively.

The minimum observed linewidth is ca. 3 MHz (Figure 7.2). If one considers this broadening to be due entirely to the Doppler broadening, the linewidth yields an upper value of 15 mK for the secular temperature, consistent with the molecular dynamics (MD) simulations in [78].

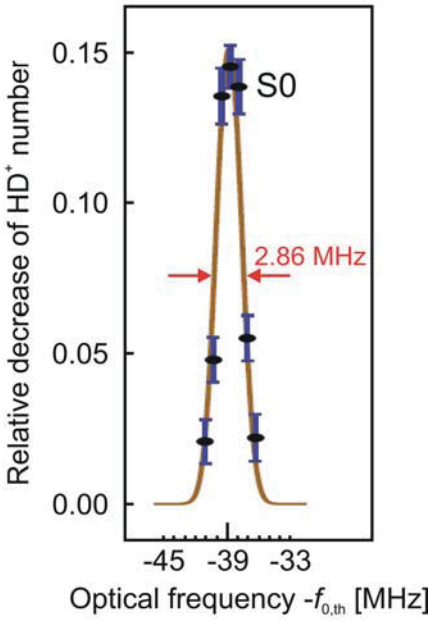

Figure 7.2 Determination of the S0 transition linewidth (FWHM).

7.2 Discussion

7.2.1 Analysis I

As a result of the high resolution of the hyperfine-resolved spectrum, an accurate comparison of the experimental frequencies with the ab-initio theory becomes possible.

The measured transition frequency combinations $f(S1)-f(W2)$, $f(W3)-f(W1)$, $f(P2)-f(S0)$ and $f(W4)-f(S1)$, $f(P3)-f(P2)$ provide two hyperfine state separations in the ground state, $\Delta f_{0,0,a}=\left(E(0,0,1,2,2)-E(0,0,1,1,1)\right)/h$ and $\Delta f_{0,0,b}=\left(E(0,0,1,1,1)-E(0,0,1,0,0)\right)/h$. These two separations are shown as light green double arrows in Figure 7.3.
In addition, two excited state splittings $\Delta f_{1,1,c}=\left(E(1,1,1,2,1)-E(1,1,1,1,1)\right)/h$ (yellow) and $\Delta f_{1,1,d}=\left(E(1,1,1,1,1)-E(1,1,1,0,1)\right)/h$ (yellow) can be obtained with the corresponding transition frequency combinations.

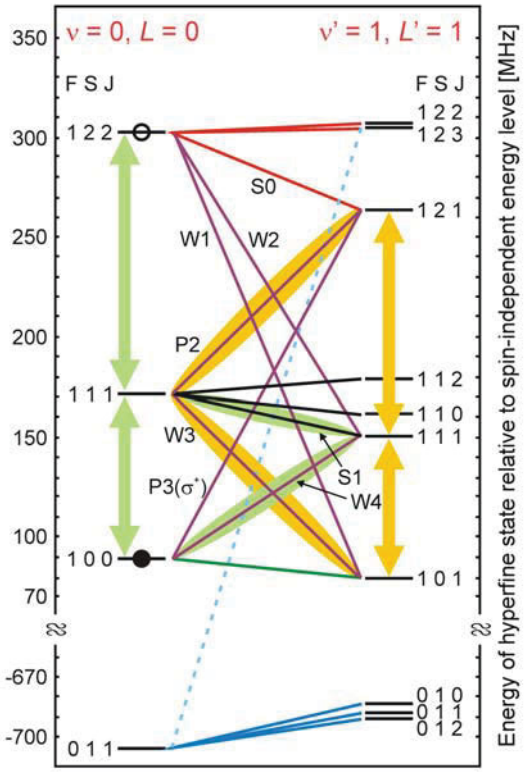

Figure 7.3 Illustration of the measured transition frequency combinations. The two hyperfine state separations of the ground state are shown as light green double arrows, the two excited hyperfine state splittings are shown as yellow double arrows.

Fitting these hyperfine state separations (and the experimentally determined spin-independent frequency) to the data gives

$\Delta f_{0,0,a} =$	$\Delta f_{0,0,b} =$	$\Delta f_{1,1,c} =$	$\Delta f_{1,1,d} =$
(130.60(1) MHz,	82.83(1) MHz,	113.32(1) MHz,	71.68(1)) MHz.

The corresponding deviations (exp. – theory) are [90]

(-0.22(0.13) MHz,	0.29(0.38) MHz,	-0.12(0.15) MHz,	0.28(0.18)) MHz.

Thus, there is very good agreement between experiment and theory.
Moreover, the measured values of the two hyperfine separations of the ground state also enable determination of the two hyperfine constants $E_4(0,0)$ and $E_5(0,0)$ given in table II of [42] which fully describe the hyperfine structure of the ground state [46].
The result of our fit is:

$$E_4(0,0) = 906(17)\ \text{MHz}, \qquad E_5(0,0) = 142.33(25)\ \text{MHz},$$

whereas the theoretical values according to [90] are

$$E_4(0,0) = 925.38(1)\ \text{MHz}, \qquad E_5(0,0) = 142.29(1)\ \text{MHz}.$$

These theoretical values differ (slightly) from to the ones presented in table II of [42] due to recent and more precise calculations by *V. I. Korobov*, not yet published.

7.2.2 Analysis II

Due to the agreement of the hyperfine theory [42] with experimental hyperfine splitting results, demonstrated in the past by *Carrington et al.* for large-υ-levels [30], the hyperfine energies given by the theoretical values can be used as reliable reference.
We can therefore fit an overall frequency correction to the spectra W1, W2, W3, S0, S1, S2+S3, W4, P2, obtaining the spin independent frequency

$$f_{0,\text{exp}} = 58\ 605\ 051.00\ \text{MHz},$$

with the combined statistical and systematic error of 0.064 MHz (see below). Compared to the theoretical value of $f_0 = 58\ 605\ 052.139$ MHz, the difference amounts to -2.0 times the combined error.
The relative experimental uncertainty is 1.1 x 10^{-9} and represents the most accurate test of molecular theory to date. Notably, our measurement is the first molecular measurement with sufficient accuracy to be explicitly sensitive to the QED contributions of order α^5. Their contribution to the transition frequency has been calculated as 0.109(21) MHz for the ro-vibrational transition studied here (Table 2.2).

7.2.3 Systematic errors

Measurements of the experiments' systematics are not possible due to the systems' complexity and the slow data rate of the spectroscopic measurement runs. Nevertheless, the upper limits of the various systematic errors can be estimated, trusting theoretical results of the well-developed theory of the HD^+ molecular ion.

Two-photon transition probabilities and light shifts

In the following, the influence of an applied laser field on the ground state energy levels in the HD^+ molecule is discussed. Because of the imbalance between the mass of the nuclei in the molecular ion (chapter 2.1), its electric dipole can be expressed according to [91] as:

$$\boldsymbol{d} = q a_0 \left(\lambda \boldsymbol{R} + \left(1+\varepsilon\right) \boldsymbol{r}_e \right), \tag{7.1}$$

where q is the electric charge, a_0 is the Bohr radius, $\lambda = \left(m_d - m_p\right) \big/ 2\left(m_e + m_p + m_d\right)$ and $\varepsilon = 1 \big/ \left(1 + \left(m_p + m_d\right) \big/ m_e\right)$. The application of a DC electric field or a linear laser field $\boldsymbol{F}$ leads to a perturbation of the Hamiltonian by the energy $-d_z F$, where d_z is the component of $\boldsymbol{d}$ along the direction of the field $\boldsymbol{F}$, chosen as quantization axis. The odd d_z operator is a linear combination of the components of $\boldsymbol{r}$ and $\boldsymbol{R}$ along the quantization axis, with the selection rules $\Delta J = \pm 1$ and $\Delta M = 0$, coupling the S^e states to the P^o states corresponding to $J = 1, M = 0$ and $\Pi = -1$. According to the notation given in [91], for two given S^e states of HD^+ $\left|\psi_\upsilon\right\rangle$, $\left|\psi_{\upsilon'}\right\rangle$ with energies E_υ and $E_{\upsilon'}$ and an energy $\{E\}$, the following matrix element can be introduced:

$$Q_{\upsilon\upsilon'}\left(E\right) = \frac{1}{4\pi\varepsilon_0 a_0^3} \left\langle \psi_\upsilon \middle| d_z \frac{1}{E-H} d_z \middle| \psi_{\upsilon'} \right\rangle. \tag{7.2}$$

Using second order perturbation theory, the correction to the energy of a level $|\psi_\upsilon\rangle$ due to an oscillating electric field $\boldsymbol{F}$ of frequency ω is given by:

$$\Delta E = -\alpha_\upsilon(\omega)\frac{1}{2}\varepsilon_0 F^2. \tag{7.3}$$

Here, the *dynamical polarizability* of the level $|\psi_\upsilon\rangle$ is given by:

$$\alpha_\upsilon(\omega) = -4\pi a_0^3\left(Q_{\upsilon\upsilon}(E_\upsilon+\hbar\omega)+Q_{\upsilon\upsilon}(E_\upsilon-\hbar\omega)\right). \tag{7.4}$$

The limit as $\omega\to 0$ of the dynamical polarizability of an eigenstate $|\psi_\upsilon\rangle$ is the *static polarizability*:

$$\alpha_\upsilon(\omega) = \alpha_\upsilon(0) = -8\pi a_0^3 Q_{\upsilon\upsilon}(E_\upsilon). \tag{7.5}$$

Considering two eigenstates $|\psi_\upsilon\rangle$ and $|\psi_{\upsilon'}\rangle$ with energies $E_\upsilon < E_{\upsilon'}$, which are not connected by a one-photon transition, using second-order perturbation theory, the two-photon transition probability for photons of frequency ω is related to $Q_{\upsilon\upsilon'}$ by [92]:

$$\Gamma_{\upsilon\upsilon'} = \left(\frac{4\pi a_0^3}{\hbar c}\right)^2 I^2 \frac{\Gamma_f}{\left(\omega_\upsilon+\delta\omega_\upsilon-(\omega_{\upsilon'}+\delta\omega_{\upsilon'})-2\omega\right)^2+\Gamma_f^2/4}\left|Q_{\upsilon\upsilon'}\left(\frac{E_\upsilon+E_{\upsilon'}}{2}\right)\right|^2. \tag{7.6}$$

Γ_f represents the width of the excited level and $I=\varepsilon_0 c F^2$ is the energy flux of the laser beam. Following the *dynamic Stark shift* caused by the applied laser field, the energy levels E_υ and $E_{\upsilon'}$ are slightly shifted by the so called *light shifts* $\hbar\delta\omega_\upsilon$ and $\hbar\delta\omega_{\upsilon'}$, appearing in equation (7.6).

The light shift of the state $|\psi_\upsilon\rangle$ by a laser of frequency ω follows from equations (7.3) and (7.4):

$$\hbar\delta\omega_\upsilon = \frac{4\pi a_0^3}{c}\frac{1}{2}I\left(Q_{\upsilon\upsilon}(E_\upsilon+\hbar\omega)\right)+\left(Q_{\upsilon\upsilon}(E_\upsilon-\hbar\omega)\right). \tag{7.7}$$

The calculation of the corresponding matrix elements $Q_{\upsilon\upsilon'}(E)$ can be found in [91].

Static stark shift

Next, the influence on the hyperfine spectra of HD^+ of the *static Stark effect* as a result of slowly varying electric fields in confining traps is discussed.
Following the notation used in the non-relativistic approximation introduced in chapter 2.2, the energy $E^{\upsilon LnJ}$ of the hyperfine state $(\upsilon LnJJ_z)$ (which is in absence of external fields independent of J_z) is the sum of the Coulomb energy and the hyperfine splitting

$$E^{\upsilon LnJ} = E^{(NR)\upsilon L} + \Delta E^{(hfs)\upsilon LnJ}. \tag{7.8}$$

In the lowest order of perturbation theory, the total angular momentum is conserved. Regarding the selection rules (see equation (2.19))

$$\boldsymbol{F} = \boldsymbol{I}_p + \boldsymbol{S}_e, \qquad \boldsymbol{S} = \boldsymbol{F} + \boldsymbol{I}_d, \qquad \boldsymbol{J} = \boldsymbol{L} + \boldsymbol{S}, \tag{7.9}$$

with electron spin $\boldsymbol{S}_e$ and nuclear spins $\boldsymbol{I}_d, \boldsymbol{I}_p$, the state vector $|\upsilon LnJ_z\rangle$ is a linear combination of the vectors $|\upsilon LFSJJ_z\rangle$ with definite values of L and angular momenta [46]:

$$|\upsilon LFSJJ_z\rangle = \sum_{FS} \beta_{FS}^{\upsilon LnJ} |\upsilon LFSJJ_z\rangle. \tag{7.10}$$

The amplitudes $\beta_{FS}^{\upsilon LnJ}$ and the hyperfine energies $\Delta E^{(hfs)\upsilon LnJ}$ follow as eigenvectors and eigenvalues of the spin interaction Hamiltonian. It has to be emphasized, that although $\boldsymbol{F}^2$ and $\boldsymbol{S}^2$ are not strictly conserved, the quantum numbers F and S are approximately good, so the label n will be identified with the pair (F,S) in the following.
The interaction of HD^+ with the electric field $\boldsymbol{E}$ in the dipole approximation is given by $V = -\boldsymbol{E}\cdot\boldsymbol{d}$.
The degeneracy of $E^{\upsilon LFSJ}$ with respect to $|J_z|$ is removed due to the interaction with the electric field. The hyperfine energy level $E^{\upsilon LnJ}$ is shifted by the quantity [96]

$$\Delta E^{\upsilon LFSJJ_z} = \sum_{q=0,\pm1} \left|E^q\right|^2 \sum_{\upsilon' L'} \sum_{F'S'J'J'_z} \frac{\left|\langle \upsilon' L'F'S'J'J'_z | d_q | \upsilon LFSJJ_z\rangle\right|^2}{E^{(NR)\upsilon L} - E^{(NR)\upsilon' L'}}, \tag{7.11}$$

where the contribution of the electronic states has been neglected.

The matrix elements of the cyclic components $d_q, q = 0,\pm1$ of the vector $\boldsymbol{d}$ are given by:

$$\begin{aligned}&\langle \upsilon' L'F'S'J'J'_z | d_q | \upsilon LFSJJ_z\rangle = \\ &d_{\upsilon' L',\upsilon L} \sum_{F_1 S_1} (-1)^{J'+L'+S_1} \sqrt{2J+1}\, C^{J'J'_z}_{JJ_z,1q} \begin{Bmatrix} J' & 1 & J \\ L & S_1 & L' \end{Bmatrix} \beta_{F_1 S_1}^{\upsilon' L'F'S'J'} \beta_{F_1 S_1}^{\upsilon LFSJ}.\end{aligned} \tag{7.12}$$

Here $d_{\upsilon' L',\upsilon L}$ express the reduced matrix elements of the dipole moment in the non-relativistic approximation.

Focusing on the laser spectroscopy of HD^+, the Stark shift of the laser-stimulated $(\upsilon LFSJJ_z) \rightarrow (\upsilon' L' F' S' J' J'_z)$ transition frequency can be evaluated as the difference of the Stark shifts of the final and initial state energy levels, given in equation (7.11).
Numerical calculations by Bakalov et al. [96] have recently been performed to give the numerical values of the reduced matrix elements $d_{\upsilon' L', \upsilon L} \equiv \langle \upsilon' L' \| \boldsymbol{d} \| \upsilon L \rangle$ in atomic units for the lowest ro-vibrational states of HD^+.

Together with the values of the amplitudes of β from [42], the Stark shifts of these states were estimated to $\delta\omega \approx 15$ Hz.

In summary, as shown above, the upper limit to the combined systematic error, attributed to the light shift, the black-body shift [91], the electric quadrupole shift [94] and the Stark shift [95], has been estimated to be less than 10 kHz.

The only significant contribution is the Zeeman effect, discussed in chapter 2.3. The sticks presented in Figure 7.1 express the expected splitting of the lines for the typical magnetic field value in our trap [46]. As previously mentioned, individual hyperfine lines can be resolved, but not the Zeeman subcomponents. The unresolved splittings can lead to a shift of the center of the lines. Estimates show that the weighted mean frequency of the magnetic components of a line shifts weakly with the magnetic field, e.g. ca. 10 kHz for line S0 at 1 G. Although determined by independent measurements to be < 1.5 G, the magnetic field is nevertheless only imprecisely known. Therefore, its influence on the fitted spin-independent frequency had to be modeled and an error of 13 kHz from this effect is estimated.
The spin-independent frequency obtained from our measurements is evaluated using the theoretical prediction of the hyperfine energies. We assume the contribution of the theoretical errors to the fitted spin-independent frequency to be ca. 15 kHz. The optical frequency measurements possess an error of less than 10 kHz. The fit of the hyperfine splittings are subject to similar considerations.

8 Summary and outlook

This work presents various new results and applications in the field of cold trapped molecular ions. The development of a novel, and in its way unique, continuous-wave 5 µm spectrometer laser source, and its application to high-resolution spectroscopy of the ro-vibrational fundamental transitions in the molecular hydrogen ion HD^+ are the focus of this thesis. This chapter briefly recapitulates the development and features of the spectrometer source and summarizes the techniques and procedures in its application to the high-resolution spectroscopy of HD^+. An overview of the results achieved is followed by a brief outlook for ongoing work.

Summary

The 5.1 µm spectrometer laser source

In order to address the $(\upsilon = 0, L = 0) \rightarrow (\upsilon' = 1, L' = 1)$ fundamental transition in cold trapped HD^+ ions, a 5.115 µm spectrometer source had to be developed [97].
It is based on difference-frequency generation (DFG) using two mid-IR laser sources at 1064 nm and 1344 nm respectively, in a periodically poled lithium niobate crystal (MgO:PPLN). Although absorption of the 5 µm radiation in the crystal was significant, a maximum output power of 105 µW was achieved. The longest generated wavelength was 5.48 µm, substantially longer than the previous limit of 4.57 µm achieved elsewhere.
The main rationale for using the DFG approach is the possibility of frequency measurement using a GPS-referenced femtosecond Ti:sapphire frequency comb. Both laser frequencies are simultaneously measured with the frequency comb and the difference frequency at 5.115 µm is calculated with a computer. Today's quantum cascade lasers (QCLs) also offer the 5 µm frequency range, but suitable frequency combs in this range are not yet available.
The 1344 nm laser source is a home-built quantum dot external cavity diode laser (QD-ECDL) in Littrow configuration with a free-running line width of 5 MHz. The laser is tunable in the range of 1316-1345 nm by turning the diffraction grating. It is frequency stabilized to a GPS-referenced femtosecond Ti:sapphire frequency comb, whereas the high power 1064 nm Nd:YAG laser is stabilized to a Doppler-free resonance in molecular iodine. The 5.1 µm radiation has a narrow linewidth of about 720 kHz. Being much smaller than the Doppler width of about 3 MHz of a typical fundamental transition in cold HD^+, the source is well-suited for high-resolution spectroscopy.
Thanks to the implementation of a sideband-producing intensity modulator, the spectrometer is frequency-tunable to any desired frequency within a range of 460 MHz around a set centre frequency. It is possible to precisely change the laser frequency at 5.1 µm with a rate of about 35 MHz/s. Such a rate was not achievable by instead tuning the frequency comb. This ability was crucial for the successful demonstration of the hyperfine pumping into a goal state.

High resolution spectroscopy of the fundamental transition in HD^+

After the development of the 5.115 μm spectrometer laser it was applied to high-resolution spectroscopy of cold, trapped molecular ions.
With a linewidth of 0.7 MHz, the frequency steps were set to 0.8 MHz to scan through the lines. The minimum observed linewidth (FWHM) was ca. 3 MHz and was consistent with the expected Doppler broadening at 15 mK.
Due to the spectrometer's ability to relatively-rapidly frequency tune to any desired frequency around a set centre frequency, e. g. the unperturbed transition frequency of the fundamental transition $(\upsilon = 0, L = 0) \rightarrow (1,1)$, it was possible to demonstrate for the first time the addressing of single quantum levels (still with magnetic sub states degeneracy). Moreover, even single quantum states (using nondegenerate states) could be addressed.

Furthermore, we demonstrated applications of this newly achieved quantum state "resolution": We resolved, for the first time, the hyperfine structure of two of the lowest states in HD^+. Precise measurements of the level spacings, as well as the absolute frequency of the vibrational transitions were demonstrated, both never measured before. The achieved frequency resolution is, to our knowledge, better than any previous measurement on any molecular ion.
With this new technique, it was shown, that the approach of sympathetically cooled molecular ions can lead to a higher resolution in spectroscopy than established techniques, e. g. the elegant ion beam method [27].
On the molecular physics side, the determination of the spin independent frequency $f_{0,\mathrm{exp}} = 58\ 605\ 051.00$ MHz, with a relative experimental uncertainty of 1.1 x 10^{-9} represents the main result of this work. It is, to our knowledge, the most precise test of *ab initio* theory of any molecule so far. We improved on our previous measurement in 2007 [34].

Outlook

Proposal for quantum state preparation ("hyperfine cooling")

Under typical conditions, performing rotational cooling by a single laser (λ_p), or two lasers (λ_p, λ_p'), leads to a relative statistical occupation of any individual quantum state in $(\upsilon = 0, L = 0)$ of only $\simeq (1/12)\cdot(60\% - 75\%) \simeq 5\% - 6\%$. Based on the technique described above, a sophisticated procedure for efficient population transfer could be of strong interest. The spectroscopy source is able to prepare population in a single quantum state [98]. Therefore, an optical pumping procedure for preparing most of the population in a single quantum state $(\upsilon LFSJJ_z)$, i.e. with a well-defined projection of the total angular momentum, appears to be realistic.

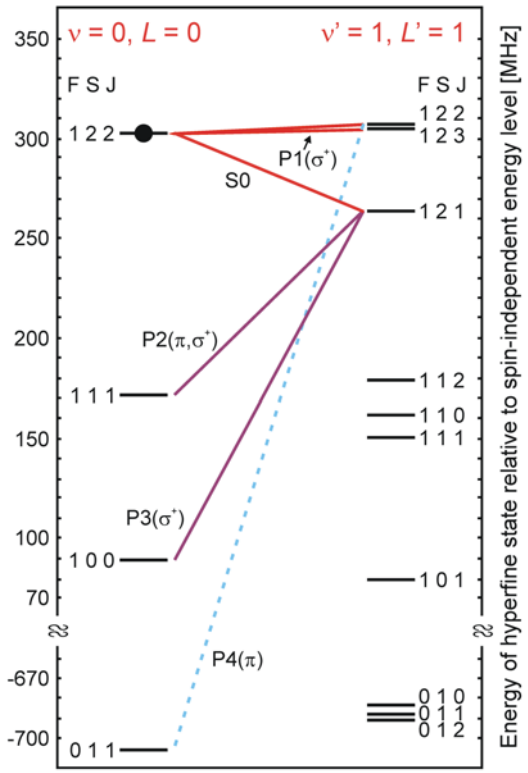

Figure 8.1 Energy diagram of the hyperfine states of two ro-vibrational levels of the HD^+ molecular ion and the main electric dipole transitions in a weak magnetic field. The indicated transitions play a role in the preparation of the single quantum state $(0,0,1,2,2,J_z=+2)$. Transitions not changing the quantum numbers F,S are relatively strong and are marked in red. Transitions changing one or both quantum numbers are indicated in purple and blue. The population from the hyperfine states should be transferred to the $(0,0,1,2,2,J_z=+2)$ (filled circle).

By sequentially exciting the four transitions P4 $\left[(0,0,0,1,1)\rightarrow(1,1,1,2,2)\right]$, P3 $\left[(0,0,1,0,0)\rightarrow(1,1,1,2,1)\right]$, P2$\left[(0,0,1,1,1)\rightarrow(1,1,1,2,1)\right]$ and P1$\left[(0,0,1,2,2)\rightarrow(1,1,1,2,3)\right]$ in a weak magnetic field and with the polarizations indicated in Figure 8.1, a transfer of the population of all Zeeman quantum states of $(0,0)$ to the single Zeeman quantum state $(0,0,1,2,2,J_z=+2)$, via spontaneous emission processes from $(0,0,1,2,2,J'=1,2,J_z)$, which dominantly occur on strong transitions (red lines), will be effected.

The transitions should overlap with rotational cooling lasers (λ_p,λ_p'), which also serve as repumpers, following the spontaneous decay into $(\upsilon''=0,L''=2)$ (see Figure 3.12, page 50). It should be emphasized that this re-pumping acts predominantly on the strong, non-spin-state changing transitions. P2 is a weak transition and P3, P4 are very weak transitions. The transition dipole moments of P3 and P4 are so small that a suitable quantum cascade laser (typical output power level ~10 mW) could be used in order to obtain a sufficiently large rate. Stabilizing it to the spectrometer presented in this work by beating the two waves could provide the necessary frequency stability for the spectroscopy. The optical pumping procedure should take several tens of seconds, leading to 60%-70% fractional population in the goal state.

An even higher fractional population could be reached, if additional cooling by depletion of the $(\upsilon = 0, L = 3)$ level, exciting from the $(1,2)$ or $(2,2)$ level, were to be applied. Other Zeeman states of the ground vibrational level could be populated to a high fraction in a similar way. It is recognized, that variations of the above scheme would achieve similar population fractions in individual states of the $(\upsilon = 0, L = 1)$ level.

Planned improvements and objectives

The results achieved so far provide strong encouragement to extend the spectroscopy measurements to additional applications and to further improve the systems used.

With the obtained accuracy and reproducibility in relatively fast frequency tuning, the 5.1 µm spectrometer offers the ability to even support additional spectroscopy schemes for other different sources. In the case of our 1.3 THz-spectroscopy source this could mean for example the population transfer to a designated state by the 5.1 µm source in order to increase the initial population in the state addressed by the THz-source.
In addition the improvement of our (1+1'+1'')-REMPD-scheme, described in chapter 5, is of interest. Here, the employed 1.4 µm laser could be tuned to a transition that addresses only one hyperfine state instead addressing all states at the same time. This would reduce the background signal level.

With a linewidth much smaller than the Doppler width of about 3 MHz of a typical fundamental transition in cold HD^+, the 5.1 µm source is well-suited for high-resolution spectroscopy. If needed, the improvement of its stability and further reduction of its linewidth is possible by stabilization of the Nd:YAG laser with the frequency comb. As shown in chapter 4, the Nd:YAG source, although stabilized on molecular iodine and possessing a linewidth of (only) $\Gamma_{1064} \approx 150$ kHz, offers the possibility of being directly stabilized to the frequency comb. Because of its construction as a master/slave laser system, careful changes have to be made, including the laser's internal beam pass so as not to endanger its availability for measurements and most of all, its critical alignment with respect to the pump beam of the difference frequency generation in the 5.1 µm spectrometer.

Regarding the 1344 nm source of the spectrometer, its stability and linewidth could be improved by phase-locking to the frequency comb, as opposed to the current frequency lock. This requires investing additional work in improving the electronics.

9 Bibliography

[1] J. K. Chin, D. E. Miller, Y. Liu, C. Stan, W. Setiawan, C. Sanner, K. Xu and W. Ketterle, Evidence for superfluidity of ultracold fermions in an optical lattice, Nature **443**, 961 (2006)

[2] W. H. Oskay, S. A. Diddams, E. A. Donley, T. M. Fortier. T. P. Heavner, L. Hollberg, W. M. Itano, S. R. Jefferts, M. J. Delaney, K. Kim, F. Levi, T. E. Parker and J. C. Bergquist, Single-Atom Optical Clock with High Accuracy, Phys. Rev. Lett. **97**, 020801 (2006)

[3] C. Schwob, L. Jozefowski, B. de Beauvoir, L. Hilico, F. Nez, L. Julien and F. Biraben, O. Acef and A. Clairon, Optical Frequency Measurement of the 2*S*-12*D* Transitions in Hydrogen and Deuterium: Rydberg Constant and Lamb Shift Determinations, Phys. Rev. Lett. **82**, 4960-4963 (1999)

[4] D. Hanneke, S. Fogwell and G. Gabrielse, New Measurement of the Electron Magnetic Moment and the Fine Structure Constant, Phys. Rev. Lett. **100**, 120801-1-4 (2008)

[5] P. J. Mohr, B. N. Taylor, and D. B. Newell (2011), "The 2010 CODATA Recommended Values of the Fundamental Physical Constants" This database was developed by J. Baker, M. Douma, and S. Kotochigova. Available: http://physics.nist.gov/constants. National Institute of Standards and Technology, Gaithersburg, USA

[6] B. Roth, J. C. J. Koelemeij, S. Schiller, L. Hilico, J.-P. Karr, V. Korobov and D. Bakalov, Precision Spectroscopy of Molecular Hydrogen Ions: Towards Frequency Metrology of Particle Masses, in “Precision Physics of Simple Atomic Systems”, Lecture Notes in Physics **745**, 205 (Springer, 2008)

[7] J. C. J. Koelemeij, B. Roth and S. Schiller, Blackbody thermometry with cold molecular ions and application to ion-based frequency standards, Phys. Rev. A **76**, 023413-1-6 (2007)

[8] J. D. Barrow. Constants and variations: From alpha to omega. Astrophys. Space Sci., **283**, 645-660 (2003)

[9] J. P. Uzan, The Fundamental Constants and Their Variation: Observational Status and Theoretical Motivations, Rev. Mod. Phys. **75**, 403-455 (2003)

[10] F. Yasunori, Oklo Constraint on the Time-Variability of the Fine-Structure Constant, Astrophysics, Clocks and Fundamental Constants, Lecture Notes in Physics **648**, 167-185 (Springer, 2004)

[11] J. K. Webb, J. A. King, M.T. Murphy, V.V. Flambaum, R. F. Carswell and M. B. Bainbridge, Indications of a spatial variation of the fine structure constant, Phys. Rev. Lett. **107**, 191101 1-5 (2011)

[12] A.-M Jeffery, R. E. Elmquist,; L.H. Lee, J.Q. Shields, R. F. Dziuba, NIST comparison of the quantized Hall resistance and the realization of the SI OHM through the calculable capacitor, IEEE Trans. Instrum. Meas. **46**, 264-268 (1997)

[13] E. Krüger, W. Nistler and W. Weirauch, Determination of the fine-structure constant by a precise measurement of h/m_n: the final result, Metrologia **35**, 203-209 (1998)

[14] J. Verdú, S. Djekić, S. Stahl, T. Valenzuela, M. Vogel and G. Werth, Electronic g Factor of Hydrogenlike Oxygen $^{16}O^{7+}$, Phys. Rev. Lett. **92**, 093002 (2004)

[15] G. Werth, J. Alonso, T. Beier, K. Blauma, S. Djekic, H. Häffner, N. Herrmanspahn, W. Quint, S. Stahl, J. Verdú, T.Valenzuela, M. Vogel, Highly charged ions, quantum–electrodynamics, and the electron mass, Int. J. Mass Spectr. **251**, 152 (2006)

[16] A. Wicht, J. M. Hensley, E. Sarajlic and St. Chu, A Preliminary Measurement of the Fine Structure Constant Based on Atom Interferometry, Physica Scripta. **T102**, 82-88 (2002)

[17] P. Cladé, E. de Mirandes, M. Cadoret, S. Guellati-Khélifa, C. Schwob, F. Nez, L. Julien and F. Biraben, Precise measurement of h/m_{Rb} using Bloch oscillators in a vertical optical lattice: Determination of the fine-structure constant, Phys. Rev. A **74**, 052109-1-18 (2006)

[18] M. P. Bradley, J. V. Porto, S. Rainville, J. K. Thompson and D. E. Pritchard, Penning trap measurements of the masses of Cs-133, Rb-87, Rb-85, and Na-23 with uncertainties ≤ 0.2 ppb, Phys. Rev. Lett. **83**, 4510-4513 (1999)

[19] R. T. Pack, Adiabatic theory of symmetry breaking and dipole moments of isotopic molecules. Correct dissociation of their electronic and muonic ions, Phys. Rev. A **32**, 2022-2029 (1985)

[20] P. Gill, Ed., Proceedings of the 6th Symposium on Frequency Standards and Metrology (World Scientific, Singapore 2002)

[21] R. E. Moss, Calculations for the vibration-rotation levels of H_2^+ in its ground and first excited electronic states, Molecular Physics **80**, 1541 (1993)

[22] R. E. Moss, Calculations for vibration-rotation levels in HD^+, in particular for high N, Molecular Physics **78**, 371 (1993)

[23] M. M. Cassar and G. W. F. Drake, High precision variational calculations for H_2^+, J. Phys. B **37**, 2485 (2004)

[24] H. Li, J. Wu, B.-L. Zhou, J.-M. Zhu and Z.-C. Yan, Calculations of energies of the hydrogen molecular ion, Phys. Rev. A **75**, 012504 (2007)

[25] V. I. Korobov, L. Hilico and J.-Ph. Karr, Relativistic corrections of $m\alpha^6(m/M)$ order to the hyperfine structure of the H_2^+ molecular ion, Phys. Rev. A **79**, 012501-1-10 (2009)

[26] K. B. Jefferts, Hyperfine structure in the molecular ion H_2^+, Phys. Rev. Lett. **23**, 1476-1478 (1969)

[27] W. H. Wing, G. A. Ruff, W. E. Lamb, J. J. Spezeski, Observation of the Infrared Spectrum of the Hydrogen Molecular Ion HD^+, Phys. Rev. Lett. **36**, 1488-1491 (1976)

[28] A. Carrington, I. McNab and C. Montgomerie. Spectroscopy of the hydrogen molecular ion, J. Phys. B **22**, 3551-3586 (1989)

[29] A. Carrington, C. A. Leach, A. J. Marr, R. E. Moss, C. H. Pyne and T. C. Steimle, Microwave spectra of the D_2^+ and HD^+ ions near their dissociation limits, J. Chem. Phys. **98**, 5290-5301 (1993)

[30] A. Carrington, I. McNab and C. Montgomerie, R. A. Kennedy, Vibration-rotation spectroscopy of the HD^+ ion near the dissociation limit, Mol. Phys. **72**, 735-762 (1991)

[31] A. Carrington, Microwave Spectroscopy at the Dissociation Limit, Science **274**, 1327-1331 (1996)

[32] D. J. Critchley, A. N. Hughes and I. R. McNab, Direct Measurement of a Pure Rotation Transition in H_2^+, Phys. Rev. Lett. **86**, 1725-1728 (2001)

[33] Y. P. Zhang, C. H. Cheng, J. T. Kim, J. Stanojevic and E. E. Eyler, Dissociation Energies of Molecular Hydrogen and the Hydrogen Molecular Ion, Phys. Rev. Lett. **92**, 203003 (2004)

[34] J. C. J. Koelemeij, B. Roth, A. Wicht, I .Ernsting and S. Schiller, Vibrational Spectroscopy of HD^+ with 2-ppb Accuracy, Phys. Rev. Lett. **98**, 173022-1-4 (2007)

[35] B. Roth and S. Schiller, Sympathetically cooled molecular ions: from principles to first applications, in „Cold molecules“, R. Krems, B. Friedrich and W. Stwalley, eds., Taylor and Francis (2009)

[36] S. Schiller, Precision spectroscopy of cold molecular hydrogen ions: Addressing and manipulation of individual hyperfine states and HD^+ frequency metrology, conference talk at IOTA-COST Workshop on cold molecular ions, Sandbjerg, Denmark (2011)

[37] C. A. Leach and R. E. Moss, Spectroscopy and quantum mechanics of the hydrogen molecular cation: A test of molecular quantum mechanics, Annu. Rev. Phys. Chem. **46**, 55-82 (1995)

[38] V. I. Korobov, Coulomb three-body bound-state problem: Variational calculations of nonrelativistic energies, Phys. Rev. A **61,** 064503-1-3 (2000)

[39] S. Schiller, V. Korobov, Tests of time independence of the electron and nuclear masses with ultracold molecules, Phys. Rev. A **71,** 032505-1-7 (2005)

[40] V. I. Korobov, Leading-order relativistic and radiative corrections to the vibrational spectrum of H_2^+ and HD^+ molecular ions, Phys. Rev. A **74**, 040502-1-4 (2006)

[41] V. I. Korobov, Bethe logarithm for the hydrogen molecular ion HD^+, Phys. Rev. A **70,** 012505-1-4 (2004)

[42] D. Bakalov, V. Korobov, S. Schiller, High-Precision Calculation of the Hyperfine Structure of the HD^+ Ion, Phys. Rev. Lett. **97**, 243001-1-4 (2006)

[43] H. Araki, Quantum-electrodynamical corrections to the energy levels of helium Prog. Theor. Phys. **17**, 619-642 (1957),

J. Sucher, Energy Levels of the Two-Electron Atom to Order α^3 ry; Ionization Energy of Helium*, Phys. Rev. **109**, 1010-1011 (1958)

[44] R. D. Ray and P. R. Certain, Hyperfine Structure in the Infrared Spectrum of HD^+, Phys. Rev. Lett. **38**, 824-826 (1977)

[45] V. I. Korobov, Relativistic corrections of $m\alpha^6$ order to the rovibrational spectrum of H_2^+ and HD^+ molecular ions, Phys. Rev. A **77**, 022509-1-3 (2008)

[46] D. Bakalov, V. I. Korobov and S. Schiller, Magnetic field effects in the transitions of the HD^+ molecular ion and precision spectroscopy, J. Phys. B: At. Mol. Opt. Phys. **44**, 025003-1-11 (2011)

[47] I. S. Vogelius, L. B. Madsen and M. Drewsen, Rotational cooling of heteronuclear molecular ions with $^1\Sigma$, $^2\Sigma$, $^3\Sigma$, and $^2\Pi$ electronic ground states, Phys. Rev. A **70**, 053412-1-14 (2004)

[48] R. C. Hilborn, Einstein coefficients, cross sections, f values, dipole moments, and all that, Am. J. Phys. **50**, 982-986 (1982)

[49] E. A. Colbourn and P. R. Bunker, Accurate Theoretical Vibration-Rotation Energies and Transition Moments for HD^+, HT^+, and DT^+, J. of Mol. Spec. **63**, 155-163 (1976)

[50] I. S. Vogelius, L. B. Madsen and M. Drewsen, Blackbody-Radiation-Assisted Laser Cooling of Molecular Ions, Phys. Rev. Lett. **89**, 173003-1-4 (2002)

[51] T. Schneider, B. Roth, H. Duncker, I. Ernsting and S. Schiller, All-optical preparation of molecular ions in the rovibrational ground state, Nature Phys. **6**, 275-278 (2010)

[52] B. Roth, J. Koelemeij, H. Daerr and S. Schiller, Rovibrational spectroscopy of trapped molecular hydrogen ions at millikelvin temperatures, Phys. Rev. A **74**, 040501-1-4 (2006)

[53] A. Ostendorf. Sympathetische Kühlung von Molekülionen durch lasergekühlte Bariumionen in einer linearen Paulfalle. PhD thesis, Heinrich-Heine-Universität Düsseldorf (2005)

[54] A. Yu. Nevsky, U. Bressel, Ch. Eisele, M. Okhapkin and S. Schiller, A. Gubenko, D. Livshits, S. Mikhrin, I. Krestnikov and A. Kovsh. A narrow-line-width external cavity quantum dot laser for high-resolution spectroscopy in the near-infrared and yellow spectral ranges. Appl. Phys. B **92**, 501-507 (2008)

[55] E. Black. An Introduction to Pound-Drever-Hall laser frequency stabilization, LIGO Project. California Institute of Technology, 37 (1999)

[56] E. V. Kovalchuk, T. Schuldt and A. Peters. Combination of a continuous-wave optical parametric oscillator and a femtosecond frequency comb for optical frequency metrology, Opt. Lett. **30**, 3141-3143 (2005)

[57] D. Mazzotti, P. Cancio, G. Giusfredi and P. De Natale. Frequency-comb-based absolute frequency measurements in the mid-infrared with a difference-frequency spectrometer, Opt. Lett. **30**, 997-999 (2004)

[58] P. Malara, P. Maddaloni, G. Gagliardi and P. De Natale. Absolute frequency measurement of molecular transitions by a direct link to a comb generated around 3-μm, Opt. Exp. **16**, 8242-8249 (2008)

[59] I. Galli, S. Bartalini, P. Cancio, G. Giusfredi, D. Mazzotti and P. De Natale. Ultra-stable, widely tunable and absolutely linked mid-IR coherent source", Opt. Exp. **17**, 9582-9587 (2009)

[60] I. Galli, S. Bartalini, S. Borri, P. Cancio, G. Giusfredi, D. Mazzotti and P. De Natale. Ti:sapphire laser intracavity difference-frequency generation of 30 mW cw radiation around 4.5 μm, Opt. Lett. **35**, 3616-3618 (2010)

[61] R. Boyd. Nonlinear Optics, Academic Press (2003)

[62] A. Yariv, P. Yeh. Optical Waves in Crystals, John Wiley & Sons, Inc., (1984)

[63] D. A. Kleinman, Theory of Optical Parametric Noise, Phys. Rev. **174**, 1027-1041 (1969)

[64] L. Myers, R. Eckhardt, M. Fejer, R. Byer, W. Bosenberg, J. Pierce. Quasi-phase-matched optical parametric oscillators in bulk periodically poled $LiNbO_3$. J. Opt. Soc. Am B/Vol. **12**, No.11, 2102–2116 (1995)

[65] http://www.crylight.com

[66] D. Faye, E. Lallier, A. Grisard, B. Gerard and E. Gil-Lafon, presented at Materials Research Society Fall Meeting, December 1.5, 2003, Boston, Mass. Symposium Z.2.2.

[67] I. Ernsting. Entwicklung und Anwendung eines Frequenzkamm-basierten Lasersystems für die Präzisions-Spektroskopie an ultrakalten Molekülen und Atomen, Dissertation, Heinrich-Heine-Universität Düsseldorf (2009)

[68] F. Quinlan, T. M. Fortier, M. S. Kirchner, J. A. Taylor, J. C. Bergquist, T. Rosenband, N. Lemke, A. Ludlow, Y. Jiang, C. W. Oates, S. A Diddams. Noise Limitations in Microwave Generation from Optical References, in CLEO/Europe and EQEC 2011 Conference Digest, OSA Technical Digest (CD), Optical Society of America, 2011, paper EE2_5.

[69] S. Earnshaw. On the nature of the molecular forces which regulate the constitution of the luminiferous ether. Trans. Camb. Phil. Soc., **7**, 97-112 (1842)

[70] P. K. Gosh, Ions traps. Oxford Univ. Press, New York (1995)

[71] W. Paul, H. P. Reinhard and U. von Zahn, Das elektrische Massenfilter als Massenspektrometer und Isotopentrenner. Z. Phys., **152**, 143-182 (1958)

[72] D. Offenberg. Studies of trapped, cooled ion ensembles. Dissertation, Heinrich-Heine-Universität Düsseldorf (2009)

[73] L. Hornekær. Single- and multi-species Coulomb ion crystals: Structures, dynamics and sympathetic cooling. PhD thesis, University of Århus (2000)

[74] B. Roth. Production, Manipulation and Spectroscopy of Cold Trapped Molecular Ions, Habilitationsschrift, Heinrich-Heine-Universität Düsseldorf (2007)

[75] M. Drewsen and A. Brøner. Harmonic linear Paul trap: Stability diagram and effective potentials. Phys. Rev. A **62**, 045401-1-4 (2000)

[76] B. Roth, P. Blythe and S. Schiller. Motional resonance coupling in cold multispecies Coulomb crystals. Phys. Rev. A, **75**, 023402-1-8 (2007)

[77] W. Schnitzler. Development of an experiment for trapping, cooling and spectroscopy of molecular hydrogen ions. PhD thesis, Universität Konstanz (2001)

[78] C. B. Zhang, D. Offenberg, B. Roth, M. A. Wilson and S. Schiller. Molecular dynamics simulations of cold single-species and multispecies ion ensembles in a linear Paul trap. Phys. Rev. A, **76**, 012719-1-13 (2007)

[79] M. Drewsen, C. Brodersen, L. Hornekær, J. S. Hangst and J.P. Schiffer. Large Ion Crystals in a Linear Paul Trap. Phys. Rev. Lett. **81**, 2878-2881 (1998)

[80] T. W. Hänsch and A. L. Schawlow. Cooling of gases by laser radiation, Opt. Commun. **13**, 68-69 (1975)

[81] D. J. Wineland and H. Dehmelt. Proposed 10^{14} $\delta\nu<\nu$ laser fluorescence spectroscopy on Tl^{+} mono-ion oscillator III. Bull. Am. Phys. Soc. **20**, 637 (1975)

[82] C. B. Zhang, Production and sympathetic cooling of complex molecular ions. PhD thesis, Heinrich-Heine-Universität Düsseldorf (2008)

[83] S. Stenholm. The semiclassical theory of laser cooling. Rev. Mod. Phys. **58**, 699-739 (1986)

[84] C. Cohen-Tannoudji. Atomic motion in laser light. Fundamental Systems in Quantum Optics (Elsevier Science Publishers, 1991)

[85] H. J. Metcalf and P. van der Straten. Laser Cooling and Trapping, Springer-Verlag, New York, Berlin, Heidelberg (1999)

[86] C. Monroe, D. M. Meekhof, B. E. King, S. R. Jefferts, W. M. Itano, D. J. Wineland. Resolved-Sideband Raman Cooling of a Bound Atom to the 3D Zero-Point Energy, Phys. Rev. Letters **75**, 4011-4014 (1995)

[87] D. H. E. Dubin and T. M. O'Neil. Trapped nonneutral plasmas, liquids and crystals (the thermal equilibrium states). Rev. Mod. Phys. **71**, 87-172 (1999)

[88] W. L. Slattery, G. D. Doolen and H. E. DeWitt, Improved equation of state for the classical one-component plasma, Phys. Rev. A **21**, 2087-2095 (1980)

[89] H. C. Miller, M. Al-Za'al, J. W. Farley, Measurement of hyperfine structure in the infrared rotation-vibration spectrum of NH^-, Phys. Rev. Lett. **58**, 2031-2034 (1987)

[90] V. I. Korobov, private communication (2010)

[91] J.-Ph. Karr, S. Kilic and L. Hilico, Energy levels and two-photon transition probabilities in the HD^+ ion, J. Phys. B **38**, 853-866 (2005)

[92] B. Cagnac, G. Grynberg et F. Biraben, Spectroscopie d'absorption multiphotonique sans effet Doppler, J. Phys. France **34**, 845-858 (1973)

[93] Z. Amitay, D. Zajfman and P. Forck, Rotational and Vibrational Lifetime of Isotopically Asymmetrized Homonuclear Diatomic Molecular Ions, Phys. Rev. A **50**, 2304-2308 (1994)

[94] A. K. Bhatia and R. J. Drachman, Static properties and the Stark effect of the ground state of the HD molecular ion, Phys. Rev. A **61**, 032503-1-7 (2000)

[95] R. E. Moss and L. Valenzano, The dipole polarizability of the hydrogen molecular cation HD^+ and other isotopomers, Mol. Phys. **100**, 1527-1535 (2002)

[96] D. Bakalov and S. Schiller, Static Stark effects in the spectroscopy of HD^+, to be published.

[97] U. Bressel, I. Ernsting and S. Schiller, 5 μm laser source for frequency metrology based on difference frequency generation, Opt. Lett. **37**, 918-920 (2012)

[98] U. Bressel, A. Borodin, J. Shen, M. Hansen, I. Ernsting, S. Schiller, Addressing and manipulation of individual hyperfine states in cold trapped molecular ions and application to HD^+ frequency metrology (submitted 2011)

10 Appendix

10.1 Laboratory room temperature stabilization

The performance of high-resolution spectroscopy experiments depends on the experiments' environment. Figure 10.1 indicates the position of the main laser sources and of the vacuum chamber in the laboratory. Due to the dimensions of the laser sources, distances up to several meters between them and the experiment have to be overcome. Despite taking great effort to provide stable and well-designed alignments, these relatively-long optical beam paths represent a weak point in terms of room-temperature sensitivity, leading to undesirable misalignments over time.
In order to obtain a reproducible experiment and to reduce the amount of work spent on realignments, measures had to be implemented to improve the temperature stability. The laboratory contains three (passive) circulatory air coolers, mounted beneath the ceiling and connected to the cold water conduit provided by the university. These coolers provide the main cooling of the laboratory but are not actively controllable to a sufficient degree, resulting in variation of the laboratory temperature by several °C over a day. These fluctuations lead to a strong variation of the output power of some of the laser sources, as well as to unpredictable alignment changes, causing additional work and reducing the reproducibility of the experiment.

To overcome these difficulties, a total of eight additional mobile air conditioners (AC) (Midea/Coolix) were installed (Figure 10.1), providing additional cooling power to the laboratory and which, being based on air exchange, are independent from the cold water conduit of the university. I developed a LabView-based program that continuously actively controls the air conditioners with a computer.
For this purpose, a USB-based A/D converter (ME-RedLab USB-Temp, Meilhaus electronics) offering up to 8 analog inputs and 8 digital in-/output channels, is used. In combination with four precision Pt-100 thermal sensors (TC-Direct) and the modification of the remote controls of the mobile ACs, the surveillance and active control of the room temperature was achieved. As presented in Figure 10.2, an instability of the room temperature of < 0.5 °C could be achieved with this procedure, strongly improving the experimental conditions. According to our experience, the best performance of the different laser sources and the experimental procedures is achieved when the set temperatures of the two controlled areas of the laboratory differ slightly. In the area used for the experiment a set temperature of 21.5 °C was chosen, whereas the other part of the room, containing the Nd:YAG laser used for the 5.1 μm source, required a set temperature of 21 °C.
Further improvement might be realized by increasing the number of sensors used for temperature acquisition and by steering of individual ACs. In principle, this might enable an individual temperature stabilization of each laser source/experiment, but would require a more complex and expensive system.

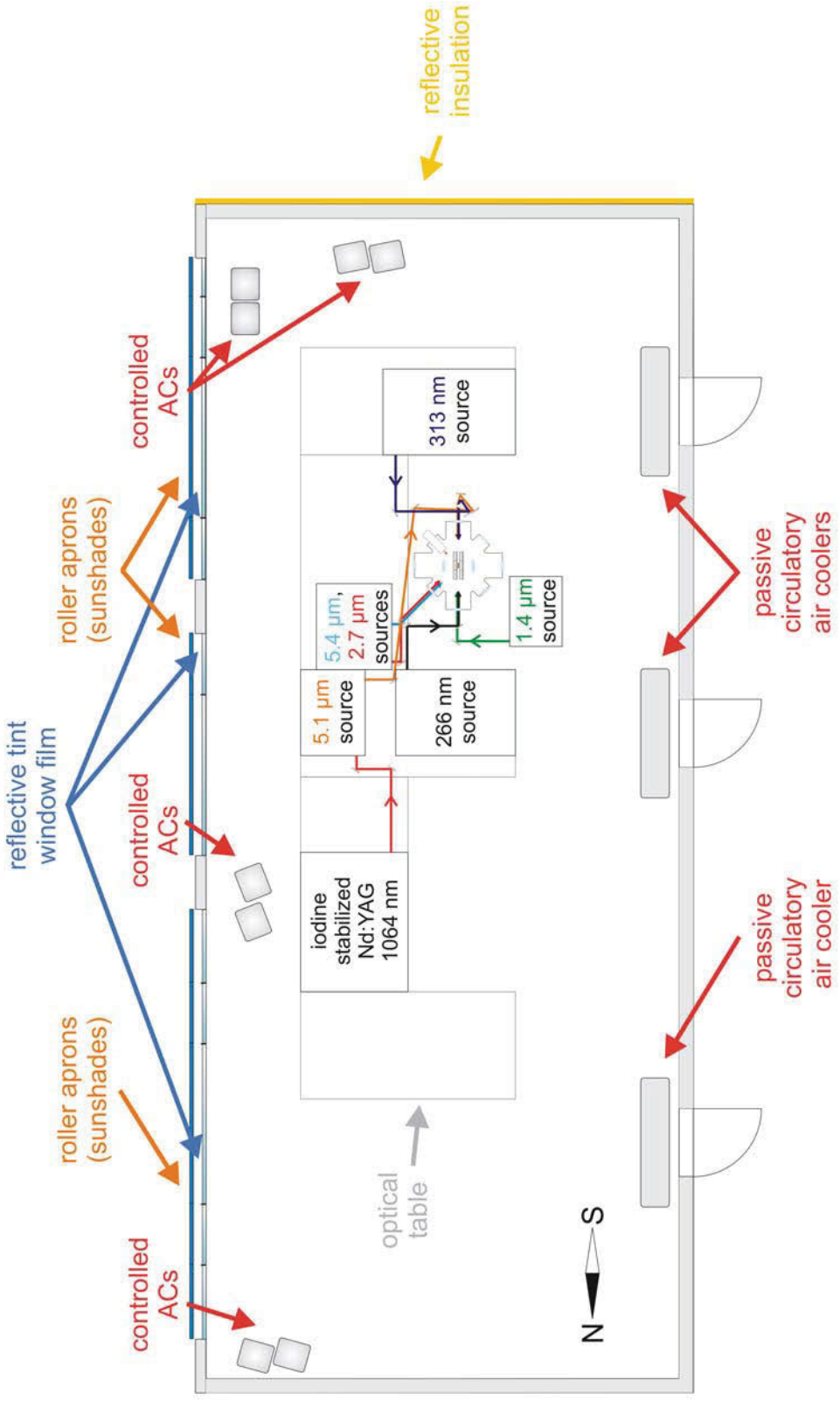

Figure 10.1 Schematic illustration of the laboratory and the measures implemented to stabilize its temperature. The position of the optical tables with the particular laser sources and the vacuum chamber including the quadrupole trap are indicated. The positions and proportions of the setups are to scale. The trap axis, as well as the whole laboratory, are arranged in a north/south direction, as displayed. Therefore, the reflective window film and the insulation reduce the solar radiation, especially in summer time.

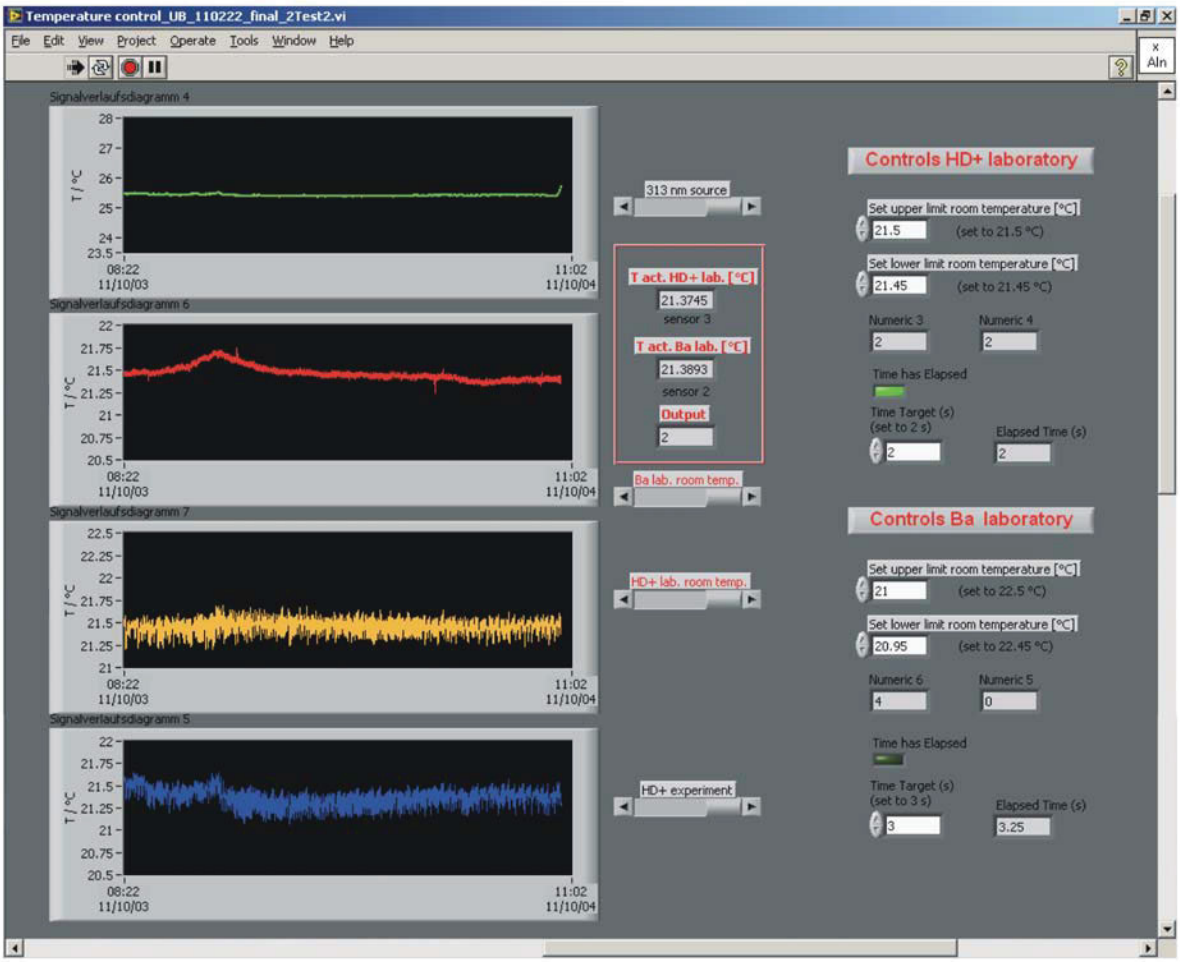

Figure 10.2 Screenshot of the LabView program used for the active room temperature stabilization. The diagrams present the typical time traces of the four Pt-100 temperature sensors, distributed throughout the laboratory. The displayed time interval is more than 26 hours. The program acquires data from one sensor (yellow graph) and controls the corresponding air conditioners used for the area around the experiment ("HD+ laboratory") and from a second sensor (red) for the control of air conditioners in a second part of the room ("Ba laboratory"). The green graph shows the temperature inside the 313 nm source, the blue graph the air temperature close to the vacuum chamber.

To further support the measures for a effective room temperature stabilization, the influence of the solar radiation on the laboratory was reduced. As can bee seen in Figure 10.1, the laboratory is oriented in a south/north direction. Due to the windows on the east side of the room, the sun heats the laboratory in the morning. Although covered from the outside with roller aprons, the heating effect is not negligible. For reduction of the solar radiation, the windows were covered with a reflective tint window film (SOLDERA SOL220 / SOL20X, BOS Wärmedesign). This special film transmits 13 %, reflects 67 % and absorbs 20 % of the radiation (manufacturer data). Consistency measurements with our sensors showed comparable values for selected wavelengths in the visible and IR ranges.

Another measure to further reduce the heating by the sun, especially in the summer time, was covering of the outside of the laboratory wall with a reflector-coated insulation material, see Figure 10.4. This material, available in every hardware store, is made from a Styropor®-like material and is normally used as a reflector behind radiators inside the room. Easy to use and cheap, this material represented a simple alternative to expensive and time-consuming building measures.

Figure 10.3 Photographs of the reflective tint window film covered windows (left) and the roller aprons (right) used for reduction of the sun irradiation.

Figure 10.4 Photograph of the reflector coated insulation material covering the south side wall of the laboratory.

10.2 Publications

A. Yu. Nevsky, U. Bressel, Ch. Eisele, M. Okhapkin and S. Schiller, A. Gubenko, D. Livshits, S. Mikhrin, I. Krestnikov and A. Kovsh. A narrow-line-width external cavity quantum dot laser for high-resolution spectroscopy in the near-infrared and yellow spectral ranges. Appl. Phys. B **92**, 501-507 (2008)

U. Bressel, I. Ernsting and S. Schiller, 5 μm laser source for frequency metrology based on difference frequency generation, Opt. Lett. **37**, 918-920 (2012)

U. Bressel, A. Borodin, J. Shen, M. Hansen, I. Ernsting, S. Schiller, Addressing and manipulation of individual hyperfine states in cold trapped molecular ions and application to HD^+ frequency metrology (submitted 2011)

Appl Phys B
DOI 10.1007/s00340-008-3113-4

Applied Physics B
Lasers and Optics

A narrow-line-width external cavity quantum dot laser for high-resolution spectroscopy in the near-infrared and yellow spectral ranges

A.Yu. Nevsky · U. Bressel · I. Ernsting · Ch. Eisele · M. Okhapkin · S. Schiller · A. Gubenko · D. Livshits · S. Mikhrin · I. Krestnikov · A. Kovsh

Received: 19 May 2008

Abstract We demonstrate a diode laser system which is suitable for high-resolution spectroscopy in the 1.2 μm and yellow spectral ranges. It is based on a two-facet quantum dot chip in a Littrow-type external cavity configuration. The laser is tunable in the range 1125–1280 nm, with an output power of more than 200 mW, and exhibits a free-running line width of 200 kHz. Amplitude and frequency noise were characterized, including the dependence of the frequency noise on the cavity length. Frequency stabilization to a high-finesse reference cavity is demonstrated, whereby the line width was reduced to approx. 30 kHz. Using a femtosecond frequency comb, the residual frequency instability was determined and found to be below 300 Hz on the time scales 1–300 s. Yellow light (>3 mW) at 578 nm was generated by frequency doubling in an enhancement cavity containing a PPLN crystal. The source has potential application for precision spectroscopy of ultra-cold Yb atoms and cold molecular hydrogen ions.

PACS 06.30.Ft · 42.55.Px · 42.62.Fi

A.Yu. Nevsky (✉) · U. Bressel · I. Ernsting · Ch. Eisele · M. Okhapkin · S. Schiller
Institut für Experimentalphysik, Heinrich-Heine Universität Düsseldorf, Universitätsstr. 1/Geb. 25.42.O1, 40225 Düsseldorf, Germany
e-mail: alexander.nevsky@uni-duesseldorf.de

A. Gubenko · D. Livshits · S. Mikhrin · I. Krestnikov · A. Kovsh
Innolume GmbH, Konrad-Adenauer-Allee 11, 44263 Dortmund, Germany

1 Introduction

Single-mode external cavity grating stabilized diode lasers (ECDLs) are well established for a wide variety of applications thanks to their compact size, relatively low cost, large wavelength tuning range (of the order of 100 nm for laser diodes with antireflection (AR) coating), high output power and reliable operation. Depending on the materials and technology used, quantum well (QW) lasers can be manufactured for different wavelength ranges extending from the blue to the mid infrared parts of the spectrum (Fig. 1).

However, some spectral ranges are impossible or difficult to reach because of material limitations. For example, the occurrence of strain-induced dislocations in InGaAs QW lasers limits the longest lasing wavelength to approx. 1.1 μm. Low electron barriers, strong Auger recombination and insufficient refractive-index contrast do not allow creation of high-performance InGaAsP lasers with wavelengths shorter than approx. 1.3 μm. InGaAs quantum dot (QD) lasers, invented in the early 1990s [1], are filling the gap between 1100 nm and 1300 nm, opening new perspectives for a variety of applications. In particular, the wavelength range covered by their second-harmonic radiation lies in the yellow. While in this range tunable, narrow-line-width radiation is available from dye lasers, continuous-wave optical parametric oscillators [2] or sum-frequency generation [3], clearly a frequency-doubled diode laser would represent a strong improvement in terms of cost, complexity and occupied volume. Compared to the well-developed external cavity QW lasers, where already sub-Hz laser line widths by active stabilization to reference resonators have been demonstrated [4–6], the current state-of-the-art of QD lasers is at a very early stage. Recently, the coherence properties of QD lasers under external feedback conditions were investigated [7], and line widths of the order of several GHz were

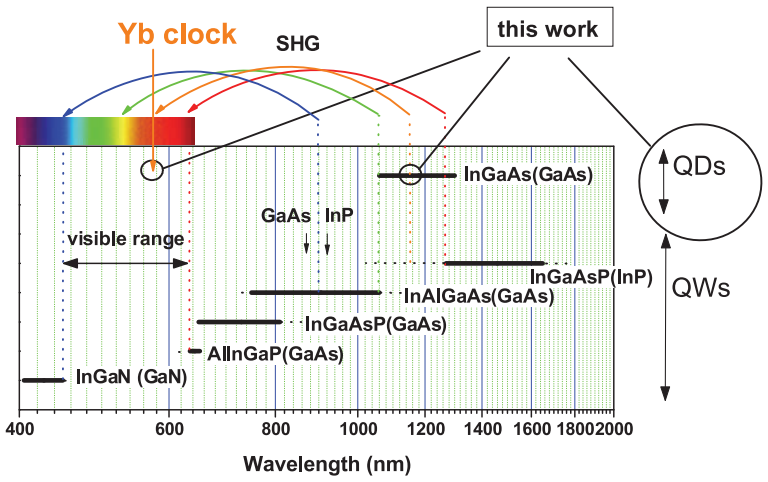

Fig. 1 Wavelength coverage of laser diodes of different types and materials. QD: quantum dot lasers, QW: quantum well lasers

demonstrated. Here we present a detailed study of a QD laser in the external cavity Littrow configuration and demonstrate for the first time that these lasers are in principle suitable for high-resolution experiments, with line width well below the 100-kHz level. We focus on the particular wavelength of 1156 nm, since the second harmonic of this radiation at 578 nm matches the clock transition in the neutral ytterbium atom, a candidate for an optical frequency standard with less than 10^{-16} inaccuracy [8].

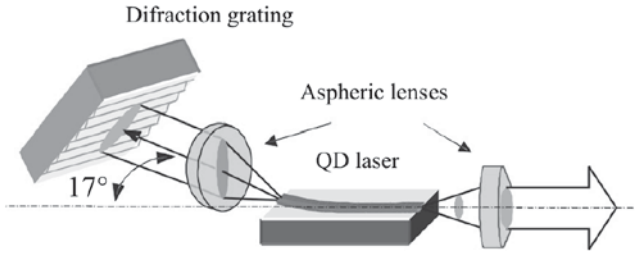

Fig. 2 Schematic of the external cavity quantum dot laser

2 Quantum dot laser chip

The semiconductor structure for the gain chip was grown by molecular-beam epitaxy. A 0.5-μm-thick GaAs waveguide is confined by 1.5-μm-thick $Al_{0.35}Ga_{0.65}As$ claddings doped with Si and C for n- and p-type conductivity, respectively. Quantum dots were formed by deposition of 0.8-nm-thick InAs insertion covered with an $In_{0.15}Ga_{0.85}As$ cap of variable thickness and a 33-nm-thick GaAs spacer. A gain region consists of 10 non-identical QD planes designed for continuous tuning between ground state and excited state optical transitions [9]. A similar QD gain region has recently been used to demonstrate a lasing spectrum as broad as 75 nm [10]. A 5-μm-wide bent ridge with a normal output facet and 5°-tilted rear facet was fabricated using a standard photolithography process, reactive ion etching and cleavage. The facets were antireflection coated with a residual reflectivity of ∼0.5%. The gain chips are mounted p-side up on the AlN carriers.

3 General properties of the QD-ECDL

The schematic of the QD-ECDL is shown in Fig. 2. The radiation emitted from the tilted facet (angle of 17° with respect to the normal to the waveguide) is collimated with an AR-coated aspheric lens.

A diffraction grating reflects the first diffraction order back to the laser chip, forming a Littrow-like configuration. Coarse wavelength tuning of the laser is obtained by changing the incidence angle of the grating. For fine tuning of the laser frequency a piezo transducer (PZT) that displaces the grating is used, allowing a mode-hop-free tuning range of about 3 GHz. The output radiation of the laser is also collimated by an aspheric lens and corrected by an AR-coated prism pair, forming an almost square cross-section beam of size approx. 6 mm × 6 mm. The whole construction including the laser chip, objectives and the grating is mounted on a copper plate, the temperature of which is stabilized with Peltier elements to better than 1 mK. The laser is driven by a custom-made ultra-low-noise current source (max. output current 750 mA) with a residual RMS current noise on the order of 1 μA. The typical output power of the laser at the wavelength of 1156 nm as a function of the operating current is shown in Fig. 3.

In this setup (‘low-noise’ implementation) the laser wavelength could be changed in the range from approx. 1148 nm to 1250 nm just by tilting the grating. Under proper alignment of the reflection grating the side mode suppression was measured to be more than 35 dB within the whole emission range. Using operating currents above 750 mA, a tuning range exceeding 200 nm as well as an output power of more than 500 mW at a central wavelength of about 1180 nm has been achieved (see Fig. 4) still keeping single spatial

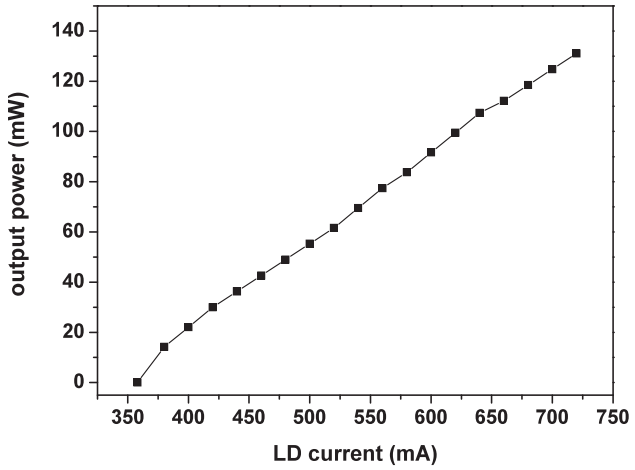

Fig. 3 Output power of the QD-ECDL at 1156 nm as a function of the operating current

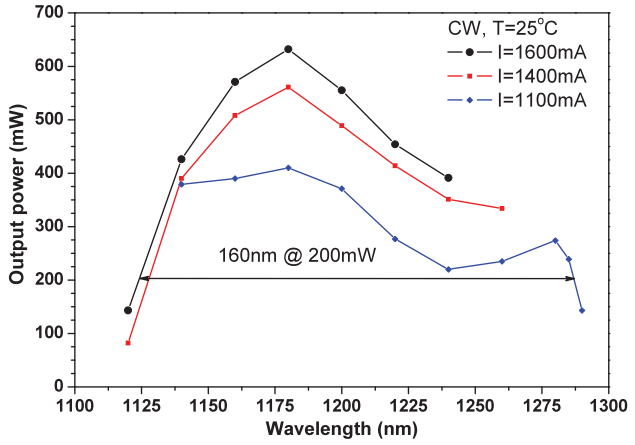

Fig. 4 Tunability and output power of the QD-ECDL under high operating currents

mode. While this range is comparable to that of the tunable InGaAs QD device reported earlier [11], our power is at least one order higher. The short-wavelength peak of the tuning curve (Fig. 4) corresponds to excited-state transitions in the quantum dots, which are favored at high pumping levels. At intermediate pump powers the quantum dot transitions from the ground state are excited (second peak of lowest line in Fig. 4), thus allowing us to obtain the wide tuning range. The two-peak structure persists despite special measures taken to enhance the power level between them.

4 Line width and frequency noise

The free-running line width of the QD-ECDL (Fig. 5) was measured by producing the heterodyne beat between two almost identical laser systems, tuned to 1165 nm. The beat was detected with a high-bandwidth photodetector and analysed with a spectrum analyser.

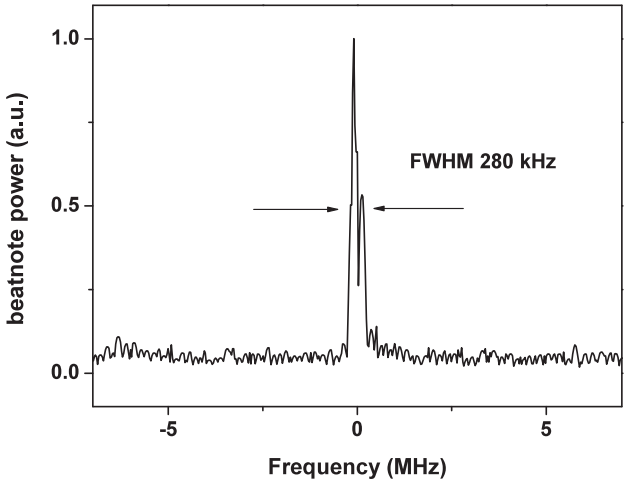

Fig. 5 Power spectrum of the beat note between two free-running QD-ECDLs (cavity lengths approx. 35 mm). The spectrum analyser resolution bandwidth is 30 kHz

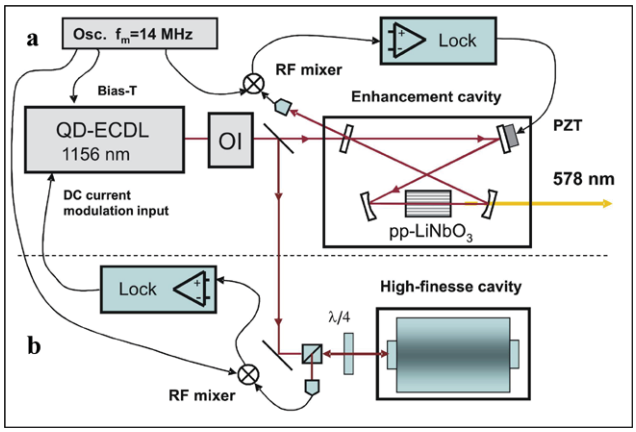

Fig. 6 Frequency-stabilization and frequency-doubling setup (OI—optical isolator, pp—periodically poled, Lock—electronic frequency stabilization system). (**a**) Setup for frequency noise characterization and for SHG in an enhancement cavity containing a pp-$LiNbO_3$ crystal. The cavity is locked to the laser. (**b**) Additional setup for frequency stabilization of the laser to the high-finesse cavity

The observed beat line width of 280 kHz (on a time scale of several 10 µs) implies a line width $\sqrt{2}$ smaller, i.e. 200 kHz for a single laser. More detailed analysis of the laser line width was not possible with this method due to a large frequency jitter of several MHz on a 1-s time scale, caused probably by current source noise and mechanical vibrations. In order to perform a detailed analysis of the laser frequency noise, in particular of the intrinsic line width, we used an external ring cavity as a frequency discriminator (Fig. 6a).

This cavity is the same as used later for resonant frequency doubling to the yellow spectral range (see Sect. 6). The resonator is formed by four mirrors, has a 750 MHz free spectral range and possesses a finesse of about 200 at

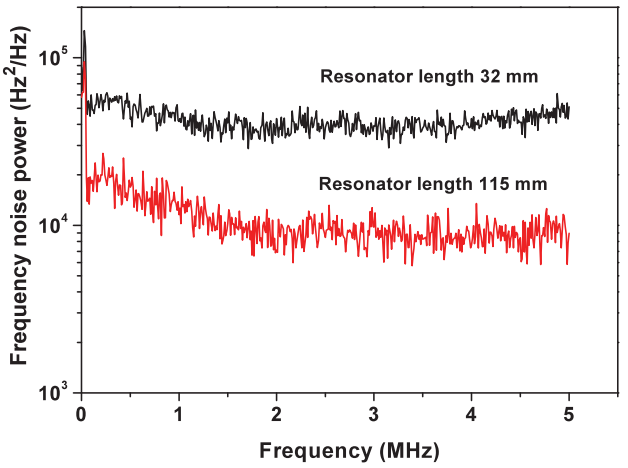

Fig. 7 Power spectral density of the QD-ECDL frequency fluctuations for two different lengths of the laser resonator (free-running regime). The spectrum is corrected for the effects of the enhancement cavity bandwidth (3 MHz FWHM)

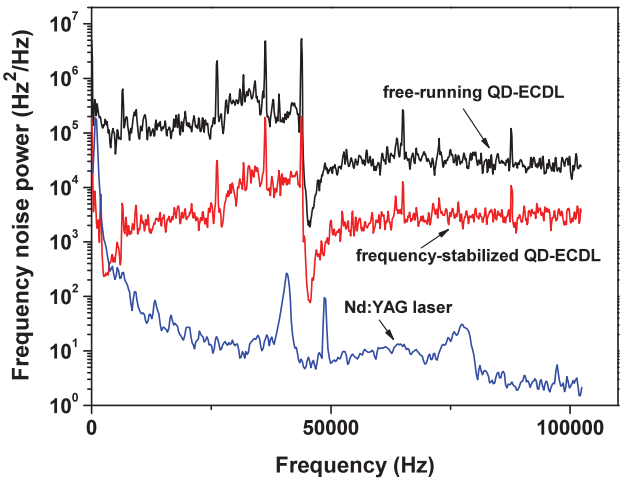

Fig. 8 Power spectral density of frequency fluctuations of the free-running and frequency-stabilized QD-ECDLs (resonator length 115 mm), obtained from the error signal of the enhancement cavity locked to the laser. The peaks at about 45 kHz are probably spurious signals. Note that the resonator lock bandwidth is about 10 kHz; thus, the frequency fluctuations in this range are not representative of the free-running laser properties. The *lower curve* is a PSD of the free-running Nd:YAG laser at 1064 nm

the wavelength of 1156 nm (including the nonlinear crystal). One of the cavity mirrors is mounted on a piezo actuator (PZT), allowing us to tune the cavity resonance frequency. The cavity is stabilized to the laser frequency using the Pound–Drever–Hall (PDH) technique. Modulation sidebands at 14 MHz were generated by modulation of the injection current of the laser, using a bias-T implemented in the current controller. In order to prevent feedback from the cavity on the QD-ECDL frequency, two optical isolators (OIs) in series were required. We used two available standard isolators optimized for 1064 nm, thus introducing high transmission losses at the wavelength of 1156 nm. The laser wave reflected from the cavity was detected by a fast photodetector and demodulated using a double-balanced RF mixer. The cavity was locked to the laser using the PZT of the cavity mirror. The servo bandwidth was several kHz, nevertheless providing a stable lock over several hours.

The frequency fluctuations of the laser were analysed from the closed loop error signal at the output of the frequency mixer. The bandwidth of this signal was about 7 MHz. For frequencies above the locking bandwidth (approx. 10 kHz), the fluctuations correspond to those of the unlocked (unstabilized) laser. The power spectral density (PSD) of the frequency fluctuations is shown in Fig. 7.

The frequency noise was characterized for two distinct QD-ECDL configurations, having resonator lengths of 32 mm and 115 mm, respectively, from the grating to the output AR facet of the laser chip. The larger resonator length showed a reduced sensitivity of the laser frequency to the operating current (30 MHz/mA in comparison to 100 MHz/mA for the 32-mm resonator). This also led to a factor 9 reduction of the frequency noise level (see Fig. 8). A simple explanation for this is the reduced influence of the optical path length fluctuations occurring in the laser chip when the total cavity length increases.

Fluctuations of the optical path in the laser diode chip can also be caused by the instability (noise) of the operating current. To estimate this effect, the laser was connected to a 12 V car battery simply by adding a resistor in series to the laser, thus forming a simple current source without any active elements. Johnson noise in the series resistor (about 20 Ω) leads to an RMS current noise of about 0.1 μA, about 10 times less than that of the laser diode driver. However, no difference in the laser frequency noise in comparison to the laser diode driver was found for either resonator length. Thus, the observed noise level is intrinsic to the lasing process.

Assuming white frequency noise, the 'fundamental' laser line width, $\Delta\nu_{\mathrm{L}}$, can be estimated using the expression [12]

$$\Delta\nu_{\mathrm{L}} = \frac{\pi(\delta\nu_{\mathrm{rms}})^2}{B} = \pi S_\nu, \tag{1}$$

where $\delta\nu_{\mathrm{rms}}$ is the RMS frequency noise of the laser, B is the bandwidth and S_ν is the power spectral density of the frequency noise in $\mathrm{Hz}^2/\mathrm{Hz}$. Using the frequency noise level from the high-frequency part of Fig. 7, (1) yields a laser line width of about 180 kHz and 60 kHz for the short and long resonators, respectively. This simple analysis does not take into account the low-frequency instability of the laser frequency, caused by mechanical instability of the laser resonator, mains pick-up and other similar parasitic effects which result in a larger line width.

5 Frequency stabilization to a high-finesse reference cavity

In order to reduce the laser line width and frequency drift, frequency stabilization to a reference cavity was implemented (see Fig. 2b). After the optical isolators, a part of the beams is split off with a beam splitter and coupled to the high-finesse reference cavity. As a reference cavity we used a SiO_2 Fabry–Perot resonator that has previously been used for relativity experiments at 1064 nm [13]. The resonator consists of a 30-mm-long SiO_2 cylinder with a diameter of 25 mm and two high-finesse mirrors, optically contacted to its end faces. At the wavelength of 1156 nm the finesse of the cavity is about 10 000. The cavity is placed inside a vacuum chamber and temperature stabilized with a Peltier element to better than 1 mK. The temperature sensitivity of the cavity was measured to be about 100 MHz/K (thermal expansion coefficient 3.8×10^{-7}/K).

The laser radiation reflected from the cavity is detected with a low-noise photodetector. The PDH signal is obtained in the standard way. The PID-type servo system controls the laser diode current. A stable lock of the laser to the high-finesse cavity was obtained. The bandwidth of the lock is about 500 kHz with a $1/f$ roll-off at low frequencies. To characterize the locking quality and residual frequency fluctuations, the enhancement cavity was again used as a discriminator. The cavity was also locked to the laser and the error signal of this lock was measured with a low-frequency FFT spectrum analyser. The frequency noise spectrum both in free-running and cavity-stabilized operation are shown in Fig. 8. Note that the frequencies below several kHz cannot be taken for an analysis since they are suppressed by the locking system of the enhancement cavity. For comparison, the frequency fluctuations of a free-running diode-pumped Nd:YAG laser at 1064 nm with intracavity doubling to 532 nm [14] are also shown. For this laser, the measurements were performed in the same way as with the QD-ECDL, i.e. the enhancement cavity was locked to the 1064-nm laser. At frequencies above several tens of kHz, the free-running frequency noise of the Nd:YAG laser is a factor of 100 smaller than that of the long-cavity QD-ECDL. From Fig. 8, and using again (1), the residual QD-ECDL line width can be estimated to be on the level of several tens of kHz. Due to the relatively small modulation index, the higher frequencies, not influenced by the locking system, contribute only to the phase noise of the laser. They should be removable by transmitting the radiation through another narrow-line width cavity. A more broadband lock of the QD-ECDL as well as a better discriminator slope are necessary in order to further reduce the laser line width.

6 Absolute frequency measurement

The frequency instability of the QD-ECDL, locked to the SiO_2 cavity, was measured using a femtosecond frequency comb (MenloSystems, FC 8004), which was stabilized to an active hydrogen maser (Vremya-Ch) and GPS. The frequency comb is based on the Ti–Sa femtosecond laser (Femtosource Scientific 200) with a repetition rate of 200 MHz. The spectrum of the laser is broadened in the photonic crystal fibre (Crystal Fibre, Femtowhite 800) to 1.5 octave, covering the range from 500 nm to 1500 nm.

The heterodyne beat note between the femtosecond comb and the laser was detected with the low-noise photodetector and measured by means of a dead time free frequency counter. The frequency measurement indicated a relatively large linear drift (30 Hz/s) of the laser frequency, which is probably due to the residual temperature instability of the SiO_2 resonator. The Allan deviation of the laser frequency is presented in Fig. 9. An Allan deviation below 200 Hz is reached for integration times between 2 and 20 s.

7 Second-harmonic generation

Second-harmonic generation (SHG) is performed in an external enhancement cavity containing a periodically poled $LiNbO_3$ crystal (PPLN) (Fig. 6a). The fundamental wave of the QD-ECDL is resonantly enhanced in the ring cavity employed and described above. The finesse of the cavity is about 200. The PPLN crystal is 25-mm long, 0.5-mm thick and possesses a grating period of 8.33 µm. The crystal end faces are coated at the fundamental and harmonic wavelengths. To prevent optical damage or photorefractive

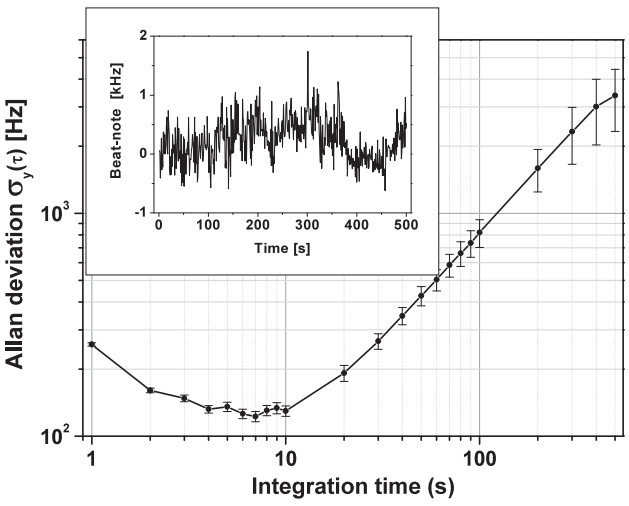

Fig. 9 Allan deviation of the frequency of the QD-ECDL stabilized to the SiO_2 cavity. The linear drift of about 30 Hz/s is removed before calculating the deviation. *Inset*: typical beat signal scatter after subtracting the linear drift, acquisition time 1 s

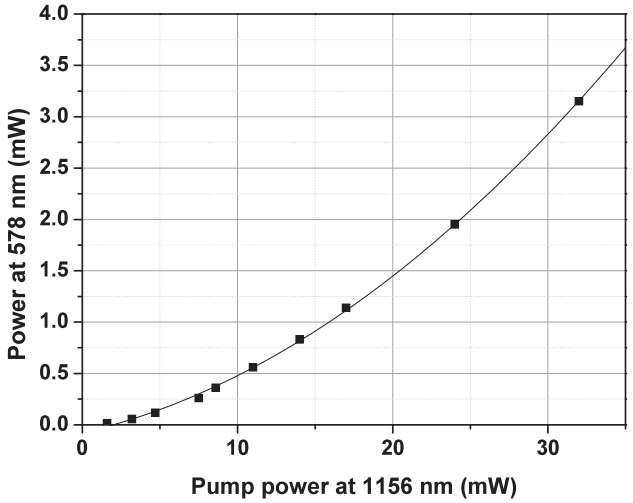

Fig. 10 Second-harmonic power (578 nm) emitted from the doubling cavity as a function of the fundamental power at the input of the cavity. *Smooth line* is quadratic fit to the data

effects, the PPLN crystal is operated in a small oven. At a temperature of about 190°C phase matching for doubling of 1156-nm radiation occurs. The thermal tuning coefficient of the phase-matched fundamental wavelength is 1.15 nm/K. The laser radiation is mode matched to the cavity using a single focusing lens. A coupling efficiency of ∼50% is obtained, due to nonperfect laser beam shape and nonoptimized input coupler mirror. The two isolators transmitted only a fraction of the diode light, resulting in about 32 mW available before the enhancement cavity. Further attempts to increase the incident power by adjusting the optical isolators led to an increased feedback and, as a result, to an unstable lock of the cavity. The power of the generated second-harmonic wave as a function of the incident power is presented in Fig. 10. The dependence is nearly quadratic, indicating that fundamental wave depletion effects are not yet present at these power levels.

Note that these results were achieved with a nonoptimal input coupling mirror. We estimate that with an optimized input coupler transmission, the SHG power could be increased by a factor of 2. In addition, the use of better optics (optical isolators, etc.) will allow us to increase the incoupled laser power, so that a few tens of mW power in the yellow should be achievable.

8 Summary and outlook

We have shown that the quantum-dot external cavity diode laser has properties comparable to those of conventional external cavity diode lasers based on quantum wells. The free-running spectral properties make the laser suitable for standard absorption or fluorescence spectroscopy, including Doppler-free spectroscopy, with spectral resolution at the several MHz level. Since, as we demonstrated, frequency locking to a reference cavity and line-width reduction to several 10 kHz are possible, QD-ECDLs are also suitable for spectroscopy at much higher resolution. We demonstrated these features at 1156 nm, but the same properties are expected at the second harmonic and at other wavelengths within the tuning range 1150–1280 nm, thus making the QD-ECDL a versatile source for high-resolution experiments.

Two applications in the field of ultra-high-resolution spectroscopy are expected to be facilitated by this source. The first is an optical atomic clock in ytterbium [8] whose ultra-narrow clock transition lies at 578 nm. For this application, a power of ∼1 mW at 578 nm is sufficient. While the clock radiation can be implemented also using a source based on sum-frequency generation, a diode laser-based clock laser is of significant interest for cost reasons or once such a clock is made compact and possibly suitable for use on satellites. A second application are vibrational transitions in the molecular hydrogen ion HD^+, a molecule of interest for tests of quantum electrodynamics and for an alternative determination of the electron-to-proton mass ratio [15]. The $v = 0 \rightarrow v = 5$ vibrational overtone transition has a rotational substructure with 10 transitions in the range 1149–1201 nm [16], whose natural line widths are 11 Hz [17]. A power level of a few mW is sufficient for the spectroscopy. In both applications, a fraction of the near-infrared light (∼mW level) would be used for optical frequency measurement by a frequency comb.

Thus, laser line widths below the 1 and 10 Hz levels, respectively, are desirable for these applications. Such a level should be achievable with the present source. For example, the achieved stabilization to the finesse-10 000 cavity could be used as a prestabilization step, to be followed by further stabilization and line-width reduction by locking to an ultra-high-finesse ULE cavity. Finally, we point out that the use of a PPLN waveguide [3] instead of an enhancement cavity could further simplify the generation of yellow light.

Acknowledgements This work was performed within the project 'Space Optical Clocks' funded by the European Space Agency (ESA) and the Deutsches Zentrum für Luft- und Raumfahrt (DLR) (project 50 QT 0701). We thank A. Görlitz for helpful discussions and loan of equipment.

References

1. N. Kirstaedter, N.N. Ledentsov, M. Grundmann, D. Bimberg, V.M. Ustinov, S.S. Ruvimov, M.V. Maximov, P.S. Kop'ev, Zh.I. Alferov, Electron. Lett. **30**, 1416 (1994)
2. T. Petelski, R.S. Conroy, K. Bencheikh, J. Mlynek, S. Schiller, Opt. Lett. **26**, 1013 (2001)

3. C.W. Oates, Z.W. Barber, J.E. Stalnaker, C.W. Hoyt, T.M. Fortier, S.A. Diddams, L. Hollberg, in *Proc. Joint Meet. IEEE Int. Frequency Control Symp. EFTF Conf.* (2007), p. 1274
4. A.D. Ludlow, X. Huang, M. Notcutt, T. Zanon-Willette, S.M. Foreman, M.M. Boyd, S. Blatt, J. Ye, Opt. Lett. **32**, 641 (2007)
5. H. Stoehr, F. Mensing, J. Helmcke, U. Sterr, Opt. Lett. **31**, 736 (2006)
6. J. Alnis, A. Matveev, N. Kolachevsky, T. Wilken, Th. Udem, T.W. Haensch, arXiv:0801.4199v1 (2008)
7. A. Tierno, T. Ackemann, Appl. Phys. B **89**, 585 (2007)
8. C.W. Hoyt, Z.W. Barber, C.W. Oates, T.M. Fortier, S.A. Diddams, L. Hollberg, Phys. Rev. Lett. **95**, 083003 (2005)
9. A.E. Zhukov, A.R. Kovsh, V.M. Ustinov, A.Yu. Egorov, N.N. Ledentsov, A.F. Tsatsul'nikov, M.V. Maksimov, S.V. Zaitsev, Yu.M. Shernyakov, A.V. Lunev, P.S. Kop'ev, Zh.I. Alferov, D. Bimberg, Semiconductors **33**, 1013 (1999)
10. A. Kovsh, I. Krestnikov, D. Livshits, S. Mikhrin, J. Weimert, A. Zhukov, Opt. Lett. **32**, 793 (2007)
11. H. Li, G.T. Liu, P.M. Varangis, T.C. Newell, A. Stintz, B. Fuchs, K.J. Malloy, L.F. Lester, IEEE Photon. Technol. Lett. **12**, 759 (2000)
12. D.S. Elliott, R. Roy, S.J. Smith, Phys. Rev. A **26**, 12 (1982)
13. S. Hermann, A. Senger, E. Kovalchuk, H. Müller, A. Peters, Phys. Rev. Lett. **95**, 150401 (2005)
14. Institute of Laser Physics, Novosibirsk. www.laser.nsc.ru
15. J.C.J. Koelemeij, B. Roth, A. Wicht, I. Ernsting, S. Schiller, Phys. Rev. Lett. **98**, 173002 (2007)
16. E.A. Colbourn, P.R. Bunker, J. Mol. Spectrosc. **63**, 155 (1976)
17. J.M. Peek, A. Hashemi-Attar, C.L. Beckel, J. Chem. Phys. **71**, 5382 (1979)

5 μm laser source for frequency metrology based on difference frequency generation

Ulf Bressel,* Ingo Ernsting, and Stephan Schiller

Institut für Experimentalphysik, Heinrich-Heine-Universität Düsseldorf, 40225 Düsseldorf, Germany
**Corresponding author: Ulf.Bressel@uni-duesseldorf.de*

Received November 22, 2011; revised January 12, 2012; accepted January 18, 2012;
posted January 18, 2012 (Doc. ID 158611); published February 28, 2012

A narrow-linewidth cw 5 μm source based on difference frequency generation of a 1.3 μm quantum dot external cavity diode laser and a cw Nd:YAG laser in periodically poled MgO : $LiNbO_3$ has been developed and evaluated for spectroscopic applications. The source can be tuned to any frequency in the 5.09–5.13 μm range with an output power up to 0.1 mW, and in the 5.42–5.48 μm range with sub-microwatt output. The output frequency is stabilized and its value determined by measuring the frequency of the two lasers with a remotely located frequency comb. A frequency instability of less than 4 kHz for long integration times and a linewidth smaller than 700 kHz were obtained.

OCIS codes: 190.2620, 190.4360, 190.4400, 300.6350.

The mid-IR spectral range offers a plethora of molecular vibrational transitions with very small transition linewidths, due to the long spontaneous lifetimes. These transitions are especially interesting when the molecules are cold, as is achievable with several methods [1]. While direct spectroscopy with a mid-IR comb [2,3] might be possible, often it will be more practical or necessary to use a sufficiently powerful single-frequency source for molecule excitation. It should be frequency-stable, exhibit narrow linewidth, and its frequency should be measurable with respect to a primary frequency standard.

In one approach, a quantum cascade laser is the spectroscopy source, and its radiation is upconverted into the near-IR for stabilization to and measurement by a conventional fiber frequency comb [4,5]. In Ref. [5], a quantum cascade laser (4.3 μm) was stabilized to a linewidth of 6.8 MHz. Another approach, capable of satisfying the requirements above, employs a parametric downconversion process of one or two lasers with relatively short wavelength. Suitable lasers with narrow free-running linewidth are available (e.g., external cavity diode lasers, solid-state lasers, fiber lasers), and their spectral range overlaps with current femtosecond frequency combs of the Ti:sapphire or Er:fiber type. The parametric downconversion can be a difference frequency generation (DFG) of two lasers or an optical parametric oscillation (OPO). The two implementations both have their advantages and disadvantages. In both cases, the (simultaneous) measurement of the frequencies of two waves must be carried out, that is, of the two input laser frequencies (DFG), or of the pump laser and signal wave frequencies (OPO), respectively. Examples of these approaches are given in Refs. [6–10], where the longest wavelength reached has been 4.57 μm [9]. This is due to the limiting effect of the intrinsic absorption of the typically used oxide crystals beyond 4.5 μm [10].

In this work, we have extended the upper wavelength limit of difference frequency generation into the strongly absorbing spectral range. By resonant enhancement of one of the two lasers we have nevertheless achieved a reasonable output power level for spectroscopy, up to 0.1 mW, even at 5.1 μm. One employed laser is a novel quantum dot external cavity diode laser (QD-ECDL) [11], the other is a monolithic cw Nd:YAG laser, frequency-stabilized to a hyperfine transition in molecular iodine. The DFG output wavelength is tunable from 5.09 to 5.13 μm by simultaneous tuning of the diode laser wavelength and of the MgO:PPLN crystal temperature. Absolute frequency measurement of the mid-IR radiation is done indirectly by a hydrogen-maser/global positioning system (GPS)-referenced Ti:sapphire frequency comb that measures simultaneously the 1.06 and 1.34 μm wave frequencies.

Figure 1 shows the experimental setup. A high power (12 W, 1064 nm) cw Nd:YAG master-oscillator/slave laser (Innolight/Laser Zentrum Hannover) is used as pump source. The laser is stabilized to a rovibrational transition of molecular iodine via Doppler-free saturation spectroscopy. The maximum power available in front of the nonlinear crystal is 5.7 W. The signal wave source is a home-built QD-ECDL (Innolume LD:GC-1320-CM-200) in Littrow configuration with a free-running linewidth of 5 MHz. The laser is tunable in the range of 1316–1345 nm with an output power of 45 mW at 1344 nm, leading to a usable power after the optical isolators (one bulk and one fiber-based, totaling –90 dB isolation) of about

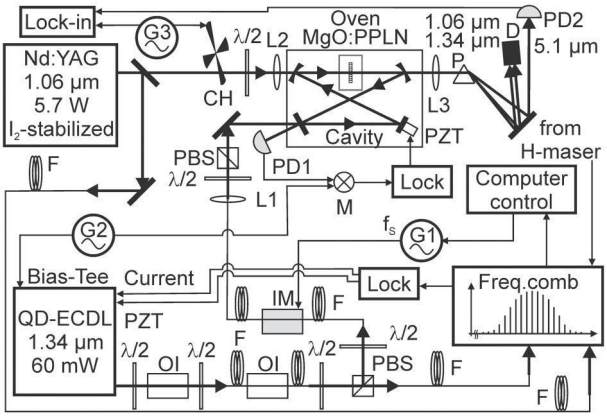

Fig. 1. Experimental setup: $\lambda/2$ retardation plates; OI, optical isolators; PBS, polarizing beam splitter cubes; F, single-mode optical fibers; IM, intensity modulator; CH, chopper wheel (for lock-in detection); PD, photodetector; P, prism; L, lenses; G, r.f. oscillator; PZT, mirror actuator; D, beam dump; M, mixer.

19 mW. To enhance the power of this laser source, a cavity, singly resonant for 1344 nm, is used. The cavity length is stabilized to the diode laser's frequency using the Pound-Drever-Hall method. With a finesse of 200, an enhancement factor of up to 60 was achieved, leading to a circulating power of 0.9 W at 1344 nm.

The MgO:PPLN crystal (HCP Photonics) is 7.4 mm long, 0.5 mm thick, 10 mm wide, and possesses six different poling periods in the range of 21–25.4 μm. Crystal faces are polished plane-parallel and antireflection (AR)-coated. The crystal's temperature is adjustable between 20–100°C, using a Peltier element driven oven. The attenuation coefficient α of the MgO:PPLN was independently measured to be $\alpha = 6.75\ \mathrm{cm}^{-1}$ at 5.485 μm and is a significant limiting factor on the achievable output power in the spectral range around 5 μm. Pump and signal beams are focused by lenses L1 (fiber collimator) and L2 (175 mm focal length) into the $\Lambda = 25.4$ μm poling period section of the crystal. In order to minimize the absorption of the generated 5 μm radiation, the foci of the two lasers, and therefore the region of largest DFG power generation, are close to the exit face of the crystal. The working point for best phase matching is 71°C, resulting in a DFG output power up to 105 μW at 5.115 μm. The mid-IR output is collimated and focused using an AR-coated CaF_2 lens (L3). The pump and signal beams are separated from the idler beam using a CaF_2 prism (P), which efficiently transmits the p-polarized idler wave. For detection, the 1064 nm wave is chop ped and the modulated 5.1 μm wave is sent on a pyroelectric detector (PYRO-LME 353) followed by lock-in detection.

In addition, the poling period $\Lambda = 24.2$ μm was tested for DFG with the diode laser tuned to 1320 nm, and both lasers in single-pass configuration (no cavity), obtaining tunable radiation in the range of 5.42–5.48 μm with 0.1 μW output level.

The frequency of the 1344 nm diode laser is stabilized to and measured by a frequency comb that is also used for frequency measurement of the iodine-stabilized 1064 nm Nd:YAG laser. The frequency comb is based on a Ti:Saphire laser and a Menlo Systems comb kit (FC 8004), modified in-house. The 1344 and 1064 nm waves are sent via two 70 m fibers to the frequency comb lab. Here, after coupling the waves out of the fibers, they are sent into two beat lines, in which the cw waves are overlapped with the comb radiation and their beats detected by fast photodetectors. Appropriate bandpass filters block the unnecessary comb modes before the overlap. The beat between the laser waves and the nearest comb modes are filtered and amplified with tracking oscillators. The frequency comb's repetition rate f_{rep} and carrier envelope frequency f_{CEO} are locked to a hydrogen maser controlled synthesizer, and the maser is itself steered to GPS on long time scales. Figure 2 shows the beat note of the 1344 nm diode laser which is frequency-stabilized to a fixed radio frequency (r.f.) with the aid of a frequency-phase detector [12]. The linewidth of the beat note is $\Gamma_{1344\text{–comb}} \approx 720$ kHz. The linewidth of the iodine-stabilized Nd:YAG laser is $\Gamma_{1064} \approx 150$ kHz, determined by beating with an independent narrow-linewidth Nd:YAG laser. The linewidth of the frequency comb modes is $\Gamma_{\mathrm{comb}} \approx 272$ kHz, also determined from

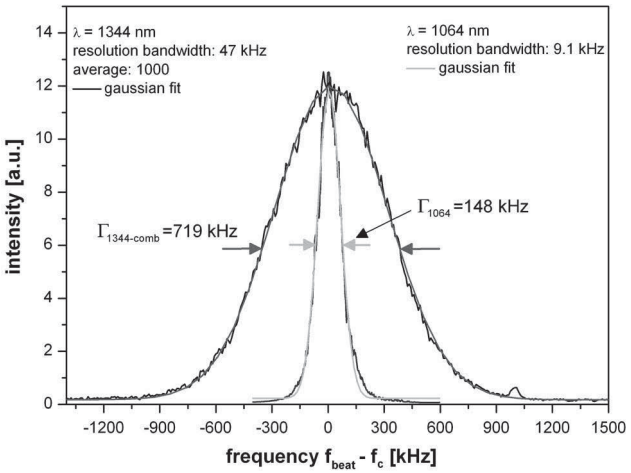

Fig. 2. Beat notes between the 1344 nm diode laser and the frequency comb and between the 1064 nm Nd:YAG laser and a narrow-linewidth (10 kHz) Nd:YAG laser (ILF100, Institute for Laser Physics, Novosibirsk).

a beat with the independent Nd:YAG laser. Therefore, the linewidth of the 5.1 μm radiation is approximately

$$\Gamma_f = (\Gamma_{1064}^2 + \Gamma_{1344\text{–comb}}^2 - \Gamma_{\mathrm{comb}}^2)^{1/2} \approx 0.68\ \mathrm{MHz}.$$

The beat notes are counted by a dead-time-free frequency counter and logged together with the frequency comb's repetition rate f_{rep} and the calculated DFG frequency. Figure 3 shows the time traces of the Nd:YAG and the diode laser frequencies, measured with the frequency comb and the calculated difference frequency at 5.1 μm. Its frequency instability is mostly due to that of the Nd:YAG laser, because of limitations of the iodine stabilization. The Allan deviation is shown in Fig. 4. The frequency instability is less than 25 kHz for short integration times and drops to 4 kHz for an integration time above 200 s.

Tuning of the generated difference frequency at 5.1 μm can be done by variation of the frequency comb's repetition rate f_{rep}, while all systems remain in lock. Typically,

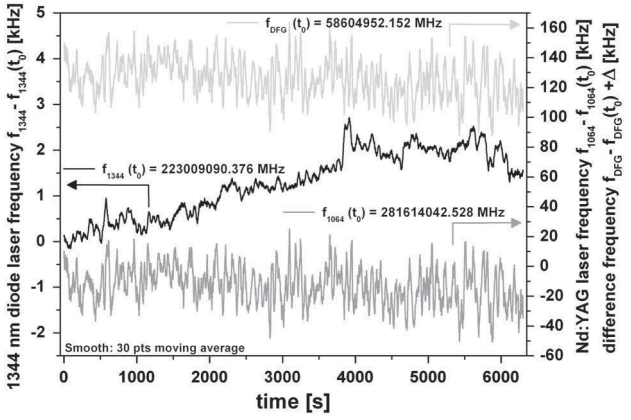

Fig. 3. Frequency traces of the Nd:YAG laser and of the diode laser, measured by the frequency comb over more than 1 h and the corresponding frequency trace of the generated difference frequency at 5.1 μm. The DFG frequency trace has a frequency offset of $\Delta = +140$ kHz for illustration purpose. Note the different vertical scales.

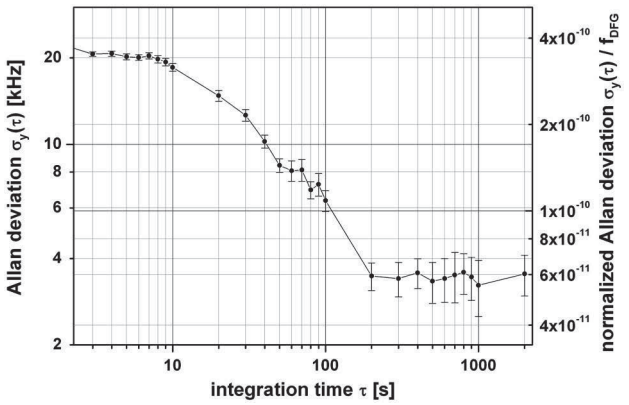

Fig. 4. Allan deviation of the difference frequency values at 5.1 μm.

a frequency sweep of (only) 10 MHz/ min, depending on the comb's working point, could be achieved.

A second approach for tuning the QD-ECDL's frequency while in lock, and thus the frequency of the 5.1 μm radiation, has been implemented using a waveguide intensity modulator (Photline Technologies, MX1300-LN-10). The $LiNbO_3$-based, low-insertion-loss intensity modulator is driven by a signal generator at a r.f. f_s and generates two symmetric sidebands ($f_{1344} \pm f_s$) with respect to the carrier frequency f_{1344}, which is kept fixed (stabilized to the comb). For sufficiently high r.f. drive strength, the carrier is suppressed and its power (nearly) completely transferred to the sidebands. The enhancement cavity is locked onto one sideband, e.g., $f_{1344} - f_s$, via the Pound-Drever-Hall technique. The generated 5.1 μm radiation $f_{1064} - (f_{1344} - f_s)$ then has a frequency offset $+f_s$ with respect to the frequency f_{1064}–f_{1344} measured by the comb. The r.f. f_s can be swept in time and the cavity lock system follows the sweep, yielding a frequency sweep in the generated 5.1 μm radiation. Figure 5 shows a typical frequency sweep. The maximum sweep range for f_s is 15 to 475 MHz, with an output power of about 2.2 μW at 5.1 μm. It is possible to manually change to a lock on the opposite sideband, thereby doubling the sweep range. To determine whether the cavity is locked to the positive or negative sideband (and therefore knowing the actual frequency at 5.1 μm), the voltage applied to the cavity mirror piezo actuator is constantly monitored. When the lock is to the negative sideband "$-f_s$", the corresponding piezo voltage decreases upon increasing the modulation frequency, while the opposite is the case for a lock to the positive sideband "$+f_s$". The maximum frequency tuning rate was 35 MHz/s.

This 5.1 μm source was successfully used in an experiment that observed and measured the frequency of the most fundamental electric dipole-allowed molecular vibrational transition, the $v = 0 \rightarrow v = 1$ transition in the molecule HD^+ (observed linewidth: 3 MHz) [13].

In conclusion, we have developed a cw narrowband mid-IR source with 105 μW maximum output power based on DFG between a Nd:YAG laser and a 1.3 μm QD-ECDL. The source was tunable to any frequency in the 5.09–5.13 μm range and is relatively rapidly tunable over a range of 460 MHz, using a sideband generator, with an output power of 2.2 μW. Stabilized in part and measured

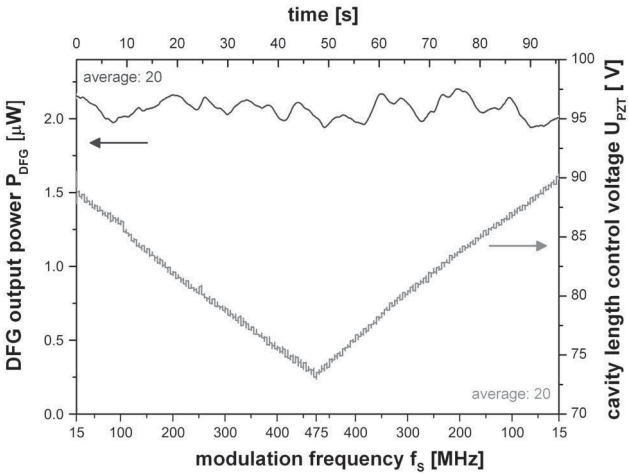

Fig. 5. DFG output power and the cavity length control voltage during a typical frequency sweep using the intensity modulator tuned to the negative sideband "$-f_s$".

by a hydrogen-maser/GPS-referenced Ti:sapphire frequency comb, the generated 5.1 μm radiation possessed a frequency instability of 8 kHz or less for integration times larger than 10 min and a spectral linewidth smaller than 700 kHz, making it well suitable for precision spectroscopic applications.

This work was performed in the framework of project Schi 431/11-1 of the German Science Foundation. We are grateful to P. Hering for an important loan of equipment, to P. Dutkiewicz for electronic support, and to A. Yu. Nevsky, T. Schneider, and S. Vasilyev for helpful discussions and support during the initial phase of the project.

References

1. R. Krems, W. Stwalley, and B. Friedrich, eds., *Cold Molecules: Theory, Experiment, Application* (CRC, 2009).
2. F. Keilmann, C. Gohle, and R. Holzwarth, Opt. Lett. **29**, 1542 (2004).
3. K. L. Vodopyanov, E. Sorokin, I. T. Sorokina, and P. G. Schunemann, Opt. Lett. **36**, 2275 (2011).
4. S. Borri, S. Bartalini, P. Cancio, I. Galli, G. Giusfredi, D. Mazzotti, and P. De Natale, Opt. Eng. **49**, 111122 (2010).
5. D. Gatti, A. Gambetta, A. Castrillo, G. Galzerano, P. Laporta, L. Gianfrani, and M. Marangoni, Opt. Express **19**, 17520 (2011).
6. E. V. Kovalchuk, T. Schuldt, and A. Peters, Opt. Lett. **30**, 3141 (2005).
7. D. Mazzotti, P. Cancio, G. Giusfredi, and P. De Natale, Opt. Lett. **30**, 997 (2005).
8. P. Malara, P. Maddaloni, G. Gagliardi, and P. De Natale, Opt. Express **16**, 8242 (2008).
9. I. Galli, S. Bartalini, P. Cancio, G. Giusfredi, D. Mazzotti, and P. De Natale, Opt. Express **17**, 9582 (2009).
10. I. Galli, S. Bartalini, S. Borri, P. Cancio, G. Giusfredi, D. Mazzotti, and P. De Natale, Opt. Lett. **35**, 3616 (2010).
11. Yu. Nevsky, U. Bressel, Ch. Eisele, M. Okhapkin, S. Schiller, A. Gubenko, D. Livshits, S. Mikhrin, I. Krestnikov, and A. Kovsh, Appl. Phys. B **92**, 501 (2008).
12. N. Strauss, I. Ernsting, S. Schiller, A. Wicht, P. Huke, and R.-H. Rinkleff, Appl. Phys. B **88**, 21 (2007).
13. U. Bressel, A. Borodin, J. Shen, M. Hansen, I. Ernsting, and S. Schiller, "Addressing and manipulation of individual hyperfine states in cold trapped molecular ions and application to HD^+ frequency metrology," Phys. Rev. Lett., submitted for publication.

Addressing and manipulation of individual hyperfine states in cold trapped molecular ions and application to HD^+ frequency metrology

U. Bressel, A. Borodin, J. Shen, M. Hansen, I. Ernsting, S. Schiller
Institut für Experimentalphysik, Heinrich-Heine-Universität Düsseldorf, Universitätsstr. 1, 40225 Düsseldorf, Germany

Advanced techniques for manipulation of internal states, standard in atomic physics, are demonstrated for a charged molecular species for the first time. We address individual hyperfine states of ro-vibrational levels of a diatomic ion by optical excitation of individual hyperfine transitions, and achieve controlled transfer of population into a selected hyperfine state. We use molecular hydrogen ions (HD^+) as a model system and employ a novel frequency-comb-based, continuous-wave 5 µm laser spectrometer. The achieved spectral resolution is the highest obtained so far in the optical domain on a molecular ion species. As a consequence, we are also able to perform the most precise test yet of the ab-initio theory of a molecule.

Cold trapped molecules [1, 2] currently represent an intense field of activity relying on sophisticated methods of molecule production, translational and internal cooling, spectroscopy and sensitive detection. Many applications, such as chemical reaction studies [3, 4], tests of molecular quantum theory [5], fundamental physics [6, 7] and quantum computing [8] would benefit strongly from the availability of advanced manipulation techniques, already standard in atomic physics. These are not straightforward for molecules, and for charged molecules have not been demonstrated yet. Production methods for molecular ions (usually by electron impact ionization) and, if heteronuclear, their interaction with the black-body radiation of the surrounding vacuum chamber, usually lead to significant population of a substantial number of internal states. A first, important step in the manipulation of internal states of molecular ions is population transfer between rotational states (heteronuclear molecules usually being cold vibrationally, i.e. are all in the $v = 0$ ground vibrational state). It has been demonstrated that a significant fraction (ca. 75%) of an ensemble of diatomic molecular ions can be pumped into the vibrational and rotational ground level ($v = 0$, $N = 0$) [9, 10], see Fig. 1.

For a general diatomic molecule, however, this pumping is usually not capable of preparing molecules in a single quantum state, because spin interactions generate a hyperfine structure with several states in each ro-vibrational level. For example, a diatomic molecule with one unpaired electron ($s_e = 1/2$), and nuclei with nuclear spins $I_1 = 1/2$, $I_2 = 1$ (such as HD^+) has 4 hyperfine states in zero magnetic field if the rotational angular momentum $N = 0$, but 10 if $N = 1$, and 12 if $N \geq 2$, see Fig. 2 a. The ability to address selectively molecules in one particular hyperfine state (or even in a single quantum state with a particular magnetic quantum number J_z) and to transfer molecules from one hyperfine state to another are clearly important tools of a molecular quantum toolbox that can be part of a full quantum state preparation procedure.

Complicating the addressing, the number of strong transitions between two given ro-vibrational levels (v, N), (v', N') is equal to the larger of the two numbers of hyperfine states, i.e. potentially high, and with only small differences in transition frequency. Fig. 2 b shows as an example the case of the fundamental vibrational transition ($v = 0$, $N = 0$) → ($v' = 1$, $N' = 1$) in HD^+, where 10 strong transitions occur over a range of about 60 MHz ([11, 12]). Addressing a single hyperfine state in a multi-spin molecule thus requires a spectroscopy that can resolve individual "hyperfine" lines in the spectrum.

In this work, our approach is based on one-photon laser excitation of the fundamental vibrational transition (0, 0) → (1, 1) at the wavelength λ_f, see Fig. 1. The relatively low transition frequency, $\lambda_f > 2.5\,\mu$m for diatomics, in combination with the low secular kinetic energy $k_B T_{sec}$ achievable by sympathetic cooling, yields a Doppler broadening $\Delta\nu_D$ of the transitions that is smaller than many line spacings. This provides the desired quantum state selectivity for addressing some of the hyperfine states, using strong transitions. For our test case HD^+, $\lambda_f = 5.1\,\mu$m, $T_{sec} \simeq 10\,$mK, $\Delta\nu_D \simeq 3\,$MHz. Additionally, excitation of weak transitions (which violate the approximate selection rules $\Delta F = 0$, $\Delta S = 0$, see Fig. 2 b), provides selectivity for all hyperfine states, since for these transitions the frequency spacings are larger. Compared to the use of a pure rotational excitation (0, 0) → (0, 1) or a microwave transition within a ro-vibrational level, the use of a vibrational transition has the advantage that the excitation may be followed by a much faster spontaneous decay, either back into the ground ro-vibrational level (rate approx. 6 s^{-1}, here) or into the (relatively long-lived) rotational level ($v'' = 0$, $N'' = 2$) (rate approx. 12 s^{-1}, here). This allows reasonably rapid pumping of the molecule (possibly after repeated absorption and spontaneous emission events) into another long-lived state, a necessary condition for efficient quantum state preparation, as shown below.

The experiment is performed on ensembles of HD^+ ions trapped in a linear quadrupole radio-frequency trap (14.2 MHz), sympathetically translationally cooled by co-trapped, laser-cooled Beryllium atomic ions [13] and rotationally cooled by lasers. Our laser system consists of four subsystems: the $\lambda_f = 5.1\,$µm laser spectrometer referenced to an atomic frequency standard [14] (see Supplementary materials), a reliable, frequency-stabilized fiber-laser-based

313 nm laser for cooling of Beryllium ions [15], a rotational cooling laser system (a $\lambda_p = 5.4\,\mu$m quantum cascade laser and, for part of the measurements, a $\lambda_p' = 2.7\,\mu$m diode laser), and a pair of lasers (λ, λ') for resonance-enhanced multi-photon dissociation (REMPD), see Fig. 1. Rotational cooling [9] is a crucial tool here, as it significantly increases the fractional population of molecules in the lower ro-vibrational level ($v = 0$, $N = 0$), from ca. 10% to 60 - 75%. The possibility provided by our laser system to measure the HD^+ fundamental vibrational transition frequency $f = c/\lambda_f$ also allows us to perform a precise comparison with the ab-initio theory of the molecular hydrogen ion.

Hyperfine-resolved ro-vibrational transitions are induced by the $\lambda_f = 5.1\,\mu$m laser tuned precisely to individual transitions. In order to show that this is actually achieved, we detect (without hyperfine state selectivity) the population of the goal vibrational level ($v' = 1$, $N' = 1$), by 1+1' resonance-enhanced multi-photon dissociation (REMPD)[16], see Fig. 1. Together, this represents a three-photon (1+1'+1") REMPD process. The reduction of the HD^+ number by the REMPD process is our spectroscopic signal [16].

Figure 3 shows the obtained hyperfine-state resolved spectrum. All theoretically predicted and addressed hyperfine transitions were observed; only the (nominally strong) transition S4 is barely detected, for unknown reason. Transition W4, which originates from a lower hyperfine state with only a small fractional population ($J = 0$, thus statistically containing only 5 - 6% of all molecules), could only be made clearly evident using a preceding hyperfine pumping

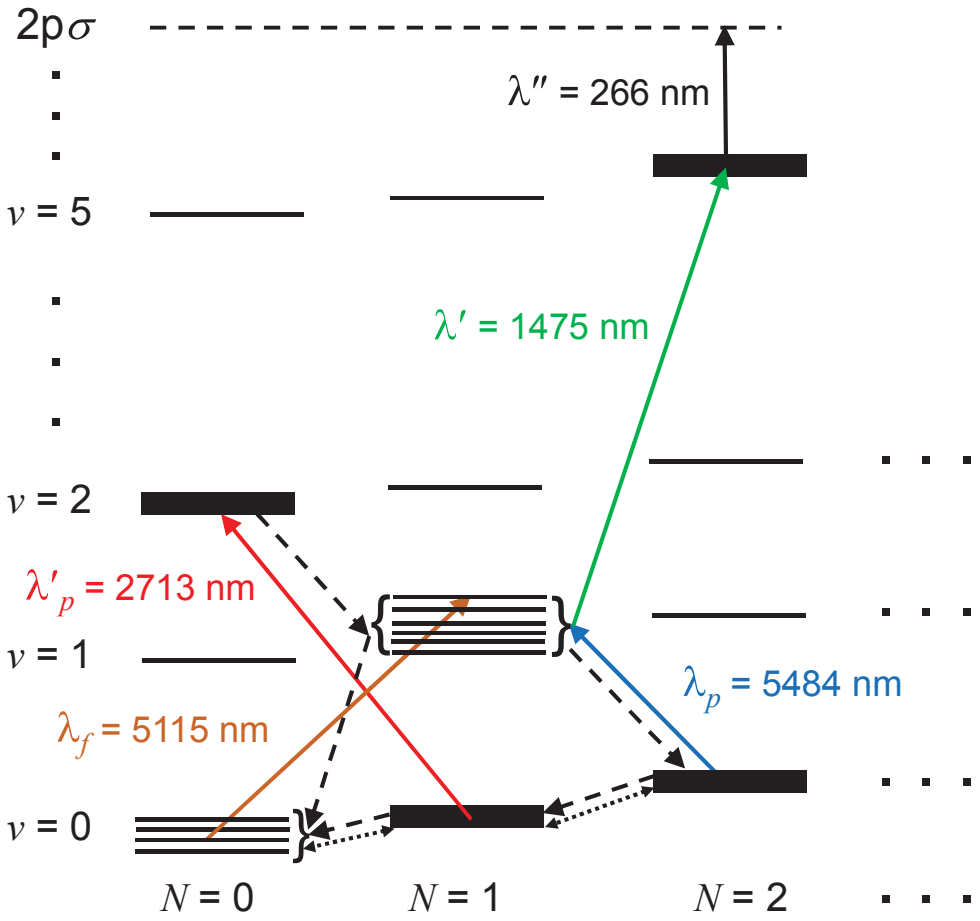

Figure 1: Schematic energy level scheme of HD^+ with transitions relevant to this work. Hyperfine structure is shown schematically only for the ($v = 0$, $N = 0$) and (1, 1) levels as lines, but is implied for all other levels as well (thick bars). Full lines: laser-induced transitions, dashed lines: some relevant spontaneous emission transitions; dotted lines: some black-body induced transitions. The spectrally narrow wave λ_f selectively excites molecules from a particular hyperfine state ($v = 0, N = 0, F, S, J$) to a single hyperfine state (1, 1, F', S', J'). Quantum state preparation is performed by irradiating alternatingly the appropriately tuned wave λ_f and λ_p , in conjunction with spontaneous emission from the level (1, 1). Resonant laser radiation at λ' and nonresonant radiaton at λ'' is used to detect that hyperfine-state-selective excitation to the (1,1) level has occurred, by transferring the excited molecules to the electronically excited molecular state 2pσ from which they dissociate. Initially, rotational cooling is performed by radiation at λ_p and λ_p' . The level energy differences are not to scale. The waves at λ', λ'', λ_p, λ_p' have large spectral linewidths and do not excite hyperfine state-selectively.

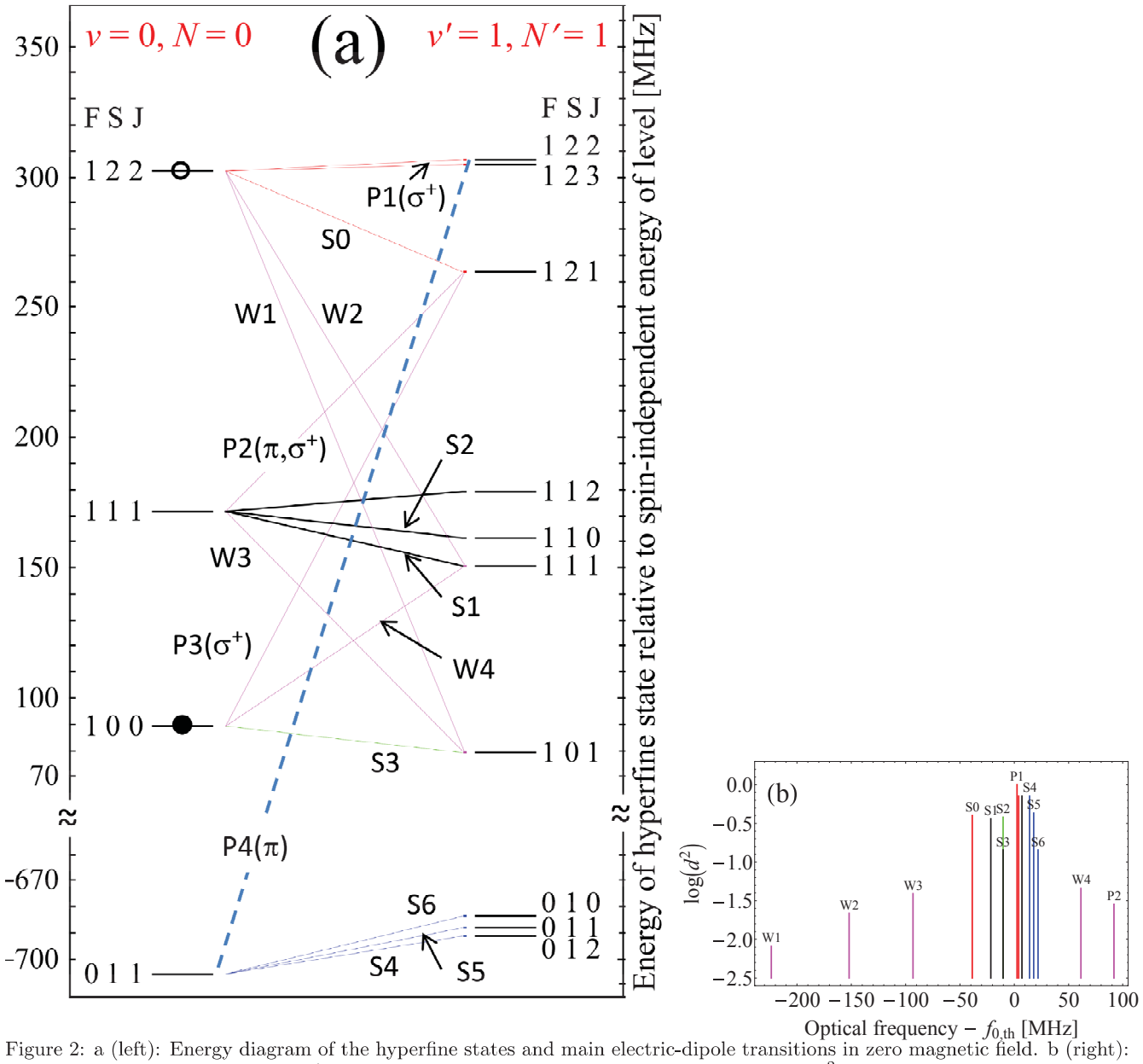

Figure 2: a (left): Energy diagram of the hyperfine states and main electric-dipole transitions in zero magnetic field. b (right): Stick spectrum of the transitions (in zero field; values of the squared transition moment d^2 are normalized to the strongest transition). The states are labeled by the quantum numbers (F, S, J). Weak transitions are shown in pink [12]. Very weak transitions are not shown, except for P4 (dashed). The "spin-independent" transition frequency $f_{0,th}$ is the value if nuclear and electron spin were zero. S0, S1, S2, S3, S4, S5, S6, W1, W2, W3, W4, P2 are transitions studied here ("W, S, P" mean "weak", "strong", "pumping", respectively). All were observed except S4. W1, W3 are the transitions used here to achieve population transfer from the hyperfine states (v = 0, N = 0, F = 1, S = 2, J = 2, J_z) (empty circle) and (0, 0, 1, 1, 1, J'_z) into the hyperfine state (0, 0, 1, 0, 0, J''_z) (filled circle). P1, P2, P3, P4 are proposed optical pumping transitions (with indicated polarizations) for preparation of the molecule in the single quantum state (0, 0, 1, 2, 2, $J_z = +2$) (one of the Zeeman states in the open circled hyperfine state).

step (see below). Each of the 4 hyperfine states of the lower level was selectively addressed, and 5 of the 12 upper level hyperfine states were selectively populated. We also observed the line at −10.2 MHz, which contains two nearly coinciding transitions S2, S3, but originating from different ground hyperfine states. The remaining strong transitions (including the line marked P1 in Fig. 2) were also observed, but their small spacing prevents complete resolution, and they are not reported in the Figure 3.

We demonstrate hyperfine state manipulation by optical pumping of individual hyperfine state populations into a

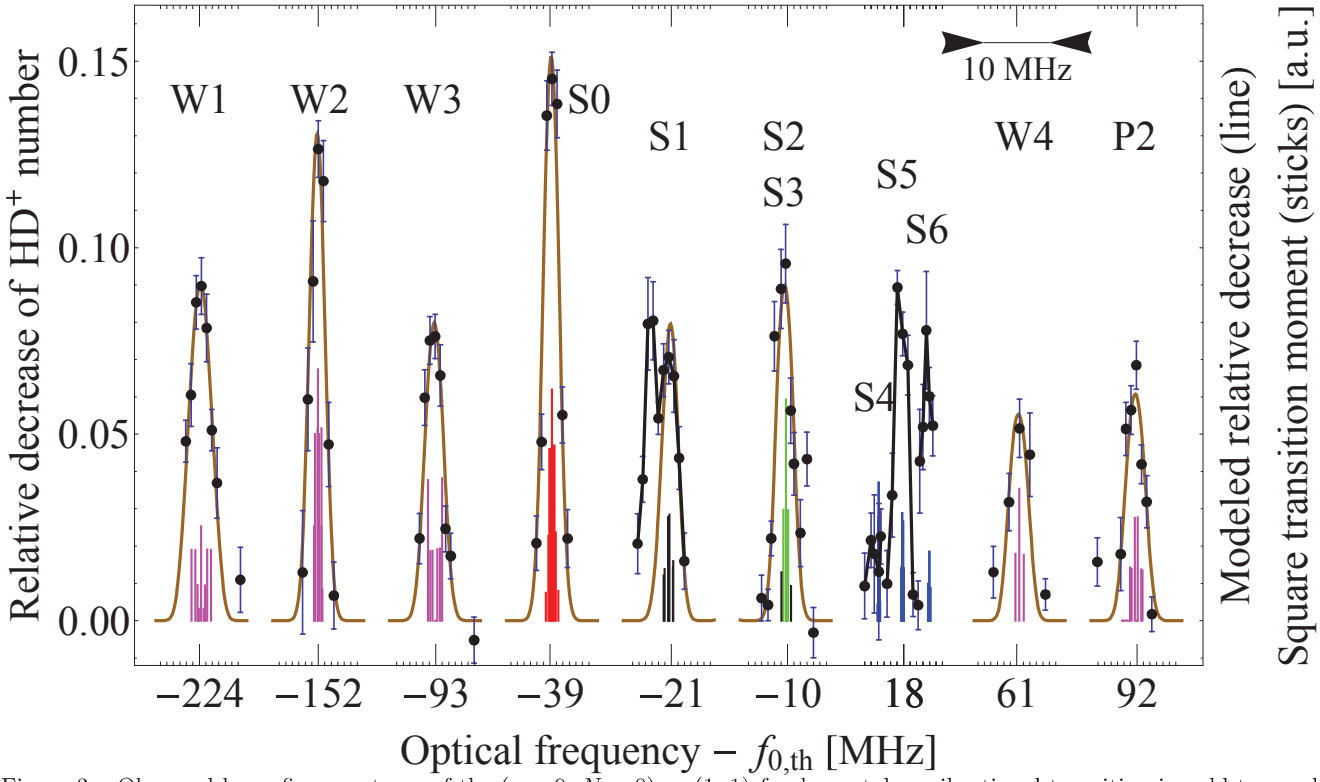

Figure 3: Observed hyperfine spectrum of the $(v = 0,\ N = 0) \rightarrow (1,\ 1)$ fundamental ro-vibrational transition in cold trapped HD^+ ions. The effective intensity times irradiation duration product of the 5.1 µm radiation varied from line to line, and was adapted to avoid saturation. Brown lines are the result of fitting $f_{0,exp}$ and the individual line amplitudes for 9.5 mK temperature, and an average magnetic field of 0.8 G. The sticks are for illustration purpose and show the theoretical squared transition dipole moments for the Zeeman components at 0.8 G, assuming exciting radiation polarized at 45 degrees to the magnetic field. They are scaled by different factors for presentation purpose. Color coding is as in Fig. 2. S4, S6 were taken at high intensity-irradiation time product, S5 at a lower value. The side peak of S1 is probably due to an ion micromotion sideband of S2/S3. The W4 line required hyperfine state optical pumping for its detection (see Fig. 4).

goal state (filled circle in Fig. 2). As a goal state we choose $(v = 0,\ N = 0,\ F = 1,\ S = 0,\ J = 0,\ J_z = 0)$ which is non-degenerate ($J = 0$) and thus a single quantum state. After rotational cooling, we apply the following sequence twice: W1 line (3 s), rotational re-pumping (λ_p and λ_p' simultaneously for 5 s), W3 line (3 s). A final 10 s of rotational re-pumping is performed before the spectroscopic excitation. The W1 and W3 transitions excite population from two initial hyperfine states $(0,\ 0,\ 1,\ 2\,,2,\ J_z)$, $(0,\ 0,\ 1,\ 1,\ 1,\ J_z')$ (without J_z selectivity) into the same hyperfine state $(1,\ 1,\ 1,\ 0,\ 1,\ J_z'')$. This state has dominant spontaneous decay to the goal state (green line S3 in Fig. 2). We find clear evidence that this hyperfine state preparation is taking place by observing the transition W4 starting from the goal state by REMPD, see Fig. 4. This transition is not observable in our experiment without the preparation procedure, since then the population in the lower hyperfine state is too low.

Our hyperfine-state resolved spectrum represents the highest-resolution optical spectrum of any molecular ion so far [5, 17, 18]. This enables an accurate comparison of experimental frequencies with ab-initio theory. We obtain two hyperfine state separations in the ground state, $\Delta f_{0,0,a} = (E(0,0,1,2,2) - E(0,0,1,1,1))/h$ and $\Delta f_{0,0,b} = (E(0,0,1,1,1) - E(0,0,1,0,0))/h$, from the measured transition frequency combinations $f(S1) - f(W2)$, $f(W3) - f(W1)$, $f(P2) - f(S0)$, and from $f(W4) - f(S1)$, $f(P3) - f(P2)$, respectively. In addition, two excited state splittings, $\Delta f_{1,1,c} = (E(1,1,1,2,1) - E(1,1,1,1,1))/h$ and $\Delta f_{1,1,d} = (E(1,1,1,1,1) - E(1,1,1,0,1))/h$ are similarly obtainable by suitable frequency combinations. A fit of these hyperfine state separations to the data (fitting also the spin-independent frequency) yields agreement with the ab-initio results $(\Delta f_{0,0,a},\ \Delta f_{0,0,b},\ \Delta f_{1,1,c},\ \Delta f_{1,1,d})_{th} =$ (130.60(1), 82.83(1), 113.33(1), 71.68(1)) MHz [11, 19], with deviations (*exp.* − *theory*) of (−0.22(0.13), 0.28(0.38), −0.13(0.15), 0.27(0.19)) MHz. The two measured hyperfine separations of the ground state also allow determining the two hyperfine constants $E_4(0,0)$, $E_5(0,0)$ [11] which fully describe the hyperfine structure of the ground state [12]. Our fit yields $(E_4(0,0),\ E_5(0,0)) =$ (906(17), 142.33(25)) MHz, whereas the theory values are (925.38(1), 142.29(1)) MHz

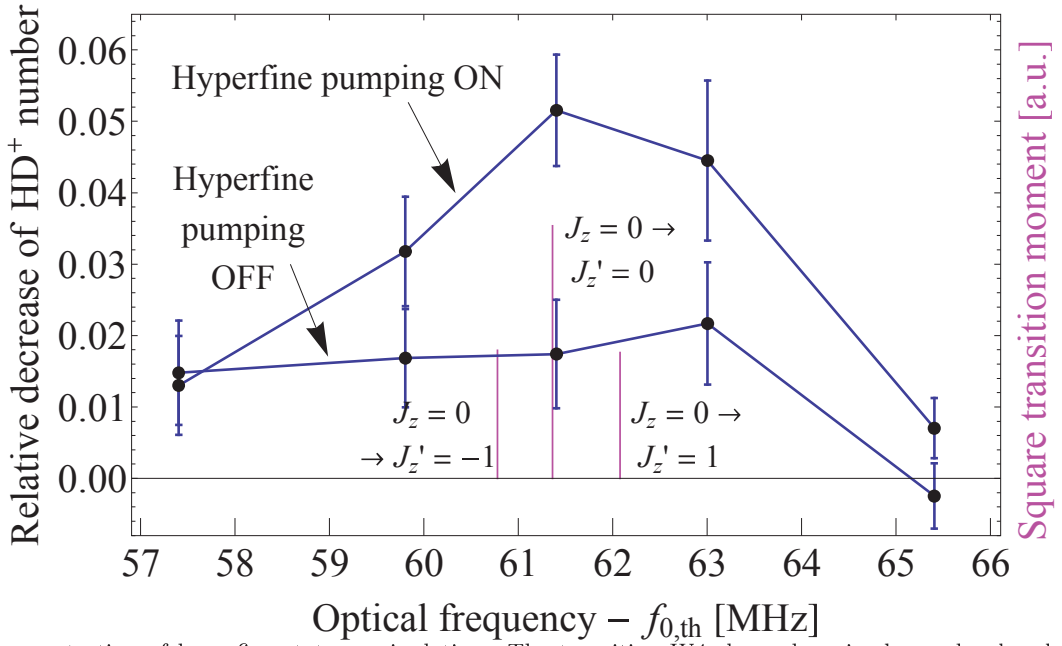

Figure 4: Demonstration of hyperfine state manipulation. The transition W4 shown here is observed only when hyperfine optical pumping is implemented. This transition represents the excitation from a single quantum state, (0, 0, 1, 0, 0, $J_z = 0$). Data shown was taken alternating measurements preceded by hyperfine optical pumping (upper data points joined by line) and not (lower data points). The intensity of the 5.1 µm laser was set to its maximum both during hyperfine pumping on the W1 and W3 transitions and subsequent detection of the W4 transition. Irradiation time on the W4 transition was 3 s. Rotational cooling by the 2.7 µm and 5.5 µm laser was used. The zero level corresponds to the relative decrease measured when the 5.1 µm spectroscopy laser was blocked. The three sticks show, for illustration purposes, the theoretical transition frequencies and strengths in a 0.8 G magnetic field and radiation polarized at 45 degree to the magnetic field. The shift of the central component is −0.05 MHz relative to the zero-field frequency.

[11, 19].

Assuming instead that the hyperfine energies are given by the theoretical values (this assumption being strenghtened by the agreement of hyperfine theory and experiment for large-v levels [11, 20]), we can fit an overall frequency correction to the spectra W1, W2, W3, S0, S1, S2+S3, W4, P2. We obtain the spin-independent frequency $f_{0,exp}$ = 58 605 052.00 MHz, with combined statistical and systematic error of 0.064 MHz (see Supplemental Materials). The theoretical value is $f_{0,th}$ = 58 605 052.139(11)(21) MHz, where the first error is due to the uncertainty of the fundamental constants and the second is the theoretical error in the evaluation of the QED contributions [19, 21, 22]. The difference between exprimental and theoretical resuls is −2.0 times the combined theoretical plus experimental error. The relative experimental uncertainty of 1.1×10^{-9} represents the most accurate test of molecular theory to date. In particular, our measurement is the first molecular measurement sufficiently accurate to be explicitly sensitive to the QED contributions of order α^5 (relative to the nonrelativistic contribution to the transition frequency), calculated as 0.109(21) MHz for the transition studied here.

Based on the technique demonstrated here, we can propose a realistic optical pumping procedure for preparing most of the population in a single quantum state (v, N, F, S, J, J_z), i.e. with well-defined projection of the total angular momentum. Under typical conditions, the relative statistical occupation of any individual quantum state in ($v = 0$, $N = 0$) is only $\simeq (1/12)\times(60\% - 75\%) \simeq 5\% - 6\%$ under rotational cooling by a single laser (λ_p) or two lasers (λ_p, λ_p'). Exciting sequentially the four transitions P4 [(0, 0, 0, 1, 1) → (1, 1, 1, 2, 2)], P3, P2, P1[(0, 0, 1, 2, 2) → (1, 1, 1, 2, 3)] in a weak magnetic field and with polarizations chosen as indicated in Fig. 2 a will cause transfer of the population of all Zeeman quantum states of (0, 0) to the single Zeeman quantum state (0, 0, 1, 2, 2, $J_z = +2$), via spontaneous emission processes from (1, 1, 1, 2, $J' = \{1, 2\}$, J_z'), which dominantly occur on strong transitions (red lines in Fig. 2 a). These excitations should be interleaved with rotational cooling (lasers λ_p, λ_p'), which also serves as repumper following spontaneous decay into ($v'' = 0$, $N'' = 2$). The optical pumping procedure should take a few ten seconds and lead to 60% - 70% fractional population in the goal state.

In summary, we have shown that it is possible to address and prepare individual hyperfine states in cold, trapped diatomic molecular ions even in presence of a complex spin structure. A mid-infrared laser spectrometer controlled by an atomic standard-referenced frequency comb, and sufficiently low ion kinetic energies were two important require-

ments. The observed, Doppler-limited, transition linewidths (3 MHz) are the lowest obtained to date on a molecular ion species in the optical domain (note that they scale as (molecule mass)$^{-1/2}$). We also observed, for the first time to our knowledge, weakly allowed hyperfine transitions using optical excitation. As one application, we were able to directly determine the population fraction of molecules in particular hyperfine states. The largest value we found was 19%, clearly indicating the effectiveness of our rotational cooling. We also demonstrated excitation of a transition from a single quantum state. Since our test molecule HD^+ is the simplest heteronuclear molecule and is excited from the ro-vibrational ground state, this study represents the first precision measurement of the most fundamental electric-dipole allowed ro-vibrational transition of any molecule [17]. A comparison of theory with experiment showed that (i) the hyperfine energies of small-v, N ro-vibrational levels agree within deviations of less than 0.3 MHz and (ii) the spin-independent energy agrees within 2 times the error of 1.1×10^{-9}.

ACKNOWLEDGEMENT. We are grateful to B. Roth, T. Schneider, A. Yu. Nevsky and S. Vasilyev for help and support, and to V. Korobov for important discussions. Funding was provided by DFG project Schi 431/11-1.

[1] R. Krems, B. Friedrich, W.C. Stwalley, eds., *Cold Molecules* (CRC Press, 2009)
[2] I.W.M. Smith, ed., *Low Temperatures and Cold Molecules* (World Scientific Publishing, 2008)
[3] B. Roth, *et al.* , Phys. Rev. A **73**, 042712 (2006);
[4] P. F. Staanum, *et al.* , Phys. Rev. Lett. **100**, 243003 (2008)
[5] J.C.J. Koelemeij, B. Roth, A. Wicht, I. Ernsting and S. Schiller, Phys. Rev. Lett. **98**, 173002 (2007)
[6] S. Schiller and V. Korobov, Phys. Rev. A **71**, 032505 (2005)
[7] H. Müller, *et al.* , Phys. Rev. A **70**, 076004 (2004)
[8] D. DeMille, Phys. Rev. Lett. **88**, 067901 (2002)
[9] T. Schneider, *et al.* , Nature Physics **6**, 275 (2010)
[10] P. Staanum, *et al.*, Nature Physics **6**, 271 (2010)
[11] D. Bakalov, *et al.*, Phys. Rev. Lett. **97**, 243001 (2006)
[12] D. Bakalov, *et al.*, J. Phys. B: At. Mol. Opt. Phys. **44**, 025003 (2011)
[13] P. Blythe, *et al.* , Phys. Rev. Lett. **95**, 183002 (2005)
[14] U. Bressel, I. Ernsting, and S. Schiller, Opt. Lett. **37**, 918 (2012).
[15] S. Vasilyev, *et al.* , Appl. Phys. B **103**, 27 (2011)
[16] B. Roth, *et al.*, Phys. Rev. A **74**, 040501-4 (2006)
[17] The (0, 1) $\leftrightarrow$ (1, 0) transition has been measured in an ion beam experiment, with a linewidth ≥ 7 MHz and a frequency uncertainy $\simeq 21$ MHz, W.H. Wing, *et al.* , Phys. Rev. Lett. **36**, 1488 (1976); J.J. Spezeski, Ph.D. dissertation, Yale University, 1977
[18] H. C. Miller, M. Al-Za'al, J. W. Farley, Phys. Rev. Lett. **58**, 2031 (1987)
[19] V. I. Korobov, private communication (2010)
[20] A. Carrington *et al.*, Mol. Phys. **72**, 735 (1991)
[21] V.I. Korobov, Phys. Rev. A **74**, 052506 (2006)
[22] V.I. Korobov, Phys. Rev. A **77,** 022509 (2008)

Supplemental Materials

1. General features of hyperfine structure

We consider a diatomic molecule with total electron spin s_e, nuclei with nuclear spins I_1, I_2, in a rotational level N. The spin degeneracy is lifted (only partially in zero magnetic field) into a number of hyperfine states by the electron spin - nuclear spin interaction ($\sim \mathbf{s}\cdot\mathbf{I_i}$) and/or the electron spin - rotation interaction ($\sim \mathbf{s}\cdot\mathbf{N}$). In HD^+, the (approximate) quantum numbers (F, S, J) correspond to the couplings $\mathbf{F}=\mathbf{s}+\mathbf{I_p}$, $\mathbf{S}=\mathbf{F}+\mathbf{I_d}$, $\mathbf{J}=\mathbf{S}+\mathbf{N}$. The electron spin - nuclear spin interactions determine the main splittings in a given ro-vibrational level, resulting in 4 singlets (if $N=0$) or in 4 multiplets (if $N\neq 0$). In the latter case, the electron-spin rotation interaction determines the splitting strength within the multiplets [11].

The line splittings in the transition spectrum, Fig. 2 b, arise because in the lower and upper levels (i) the strengths of the electron spin-nuclear spin interactions and of the electron spin - rotation interaction differ, and (ii) the rotational angular momenta N, N' differ. The density of lines in the spectrum is essentially independent of whether the transition is a fundamental vibrational transition, an overtone transition ($\Delta v = v' - v > 1$) (e.g. [16]), or a pure rotational transition ($\Delta v = 0$).

2. 5.1 µm laser spectrometer

The spectroscopy radiation was generated by frequency-mixing in a nonlinear optical crystal two near-infrared lasers which are individually referenced to a conventional frequency comb [14]. The generated wavelength, 5.1 µm, extends the coverge provided so far by sources with absolute frequency measurement capability [1, 2].

We use two continuous-wave lasers, a Nd:YAG laser (1064 nm, ca. 6 W) stabilized to a Doppler-free resonance in molecular iodine via its second-harmonic wave at 532 nm, and a 1344 nm home-built external cavity quantum-dot diode laser (QD-ECDL). The main part of the 1344 nm wave is resonantly enhanced in a ring resonator containing a periodically poled $MgO:LiNbO_3$ crystal with poling period 25.4 µm, appropriate for difference frequency generation of 5.1 µm radiation. The 1064 nm wave is focused and overlapped with the 1344 nm wave in the crystal, but not resonated. Although the crystal strongly absorbs the generated 5.1 µm radiation, an output power of up to 0.1 mW is generated. Small fractions of the 1064 and 1344 nm waves are sent via an unstabilized single-mode optical fiber to another laboratory containing the femtosecond Ti:sapphire frequency comb, where both frequencies are measured. The 1344 nm laser is actively frequency-stabilized to a mode of the frequency comb. The 1064 nm wave frequency is continuously measured by the comb. The comb itself is stabilized to a hydrogen maser or ultra-stable quartz oscillator, both referenced to GPS.

Tunable, frequency-stable 5.1 µm radiation is produced by amplitude modulating the diode laser output wave with an integrated-optic modulator at a variable radio-frequency Ω before sending the wave to the resonator. This generates two sidebands, and the resonator length is stabilized to resonate one of the two, generating a single frequency at 5.1 µm. By changing the modulation frequency Ω, the 5.1 µm radiation can be smoothly and precisely frequency-tuned over 460 MHz. We determined the spectral width of the 5.1 µm radiation as $\Gamma_f \simeq 0.68\,\mathrm{MHz}$. The frequency instability (Allan deviation) of this radiation is constant at ca. 23 kHz for integration times τ up to 10 s, dropping to 4 kHz at $\tau = 800\,\mathrm{s}$. Both linewidth and instability are significantly lower than the Doppler width of the HD^+ hyperfine transitions studied here. The absolute frequency uncertainty of the 5.1 µm radiation is less than 10 kHz when averaged over 1 h.

3. Procedures and analysis

Each data point in a spectrum measurement is acquired from one loading of HD^+ ions into a laser-cooled Be^+ ion cluster. Fig. 5 shows an example.

From molecular dynamics (MD) simulation of ion cluster fluorescence images [3] we deduce an upper limit for the secular temperature $T_{sec} \leq 15\,\mathrm{mK}$. After loading, the molecules are rotationally cooled by $\lambda_p \simeq 5.5\,\mu\mathrm{m}$ radiation (and, for some measurements, also $\lambda_p{}' = 2.7\,\mu\mathrm{m}$ radiation) for 30 s, transferring about 60% (75%) of the molecules into the ($v=0$, $N=0$) ro-vibrational ground level. This population is spread over the four hyperfine states. Then, the rotational pumping laser waves are blocked and the $5.1\,\mu\mathrm{m}$ spectroscopy radiation is applied along the trap axis for 3 - 30 s, simultaneously with a 1475 nm diode laser (ca. 1 mW) driving the $(v'=1,\ N'=1) \rightarrow (v''=5,\ N''=2)$ overtone transition, and a 266 nm laser (ca. 25 mW) that dissociates the molecules in the latter state.

The number of trapped HD^+ ions is measured by excitation of their secular motion before the rotational cooling and after the (partial) photodissociation. Excitation of the secular motion heats up all ions and therefore changes

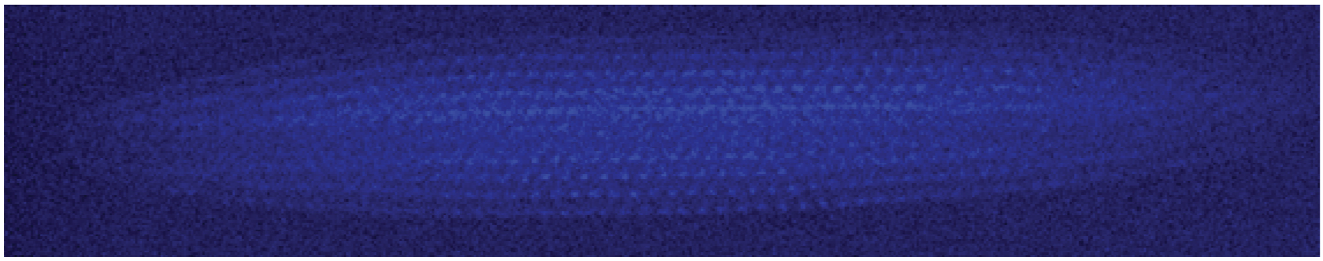

Figure 5: CCD image of a typical Beryllium ion Coulomb cluster with embedded HD^+ ions (darker region along the long axis), as used in the experiment.

the Be^+ fluorescence rate, which is detected by a photomultiplier. The relative decrease in the photomultiplier signal is the signal of interest, the excited molecule fraction. As the spectroscopy source linewidth is 0.7 MHz, we made frequency steps of typically 0.8 MHz when scanning through the lines. One data point could be recorded on average every 3 min. This limited the number of data points per frequency value that could be taken. We performed between 4 and 25 measurements per frequency point. Typically, one hyperfine transition required one day of measurement. Background level measurements were performed in the same way, with the 5.1 µm laser blocked. Alignment of the 5.1 µm laser with the ion cluster varied from day to day, which was compensated by adjusting the power.

The typical standard deviation of the relative decay data taken at a given optical frequency (not of the mean) is 0.02. This is due primarily to the low number of HD^+ ions loaded into the ion cluster (a few hundred) and the low relative population in a particular hyperfine state (only a fraction $\simeq (0.6 - 0.75)\, p_J$, where $p_J = (2J+1)/12$ in a particular hyperfine state J, for $N = 0$), which is further reduced during the REMPD phase (λ_p, $\lambda_p{}'$ lasers off) by the competing black-body-radiation driven excitation ($v = 0$, $N = 0$) $\rightarrow$ (0, 1). The overall small numbers lead to significant statistical fluctuations in the number of ions actually prepared into a particular initial hyperfine state after optical pumping, and in the fraction excited and dissociated. As a consistency check, we found that the maximum observed dissociated fractions (at high intensity and on resonance) did not exceed p_J. For example, for line S0, we observed (19.4±1.4)% ion number reduction, for lines S2+S3, (16.4±2.8)%. Note that the values shown in Fig. 3, are lower because there, lower intensities were used in order to avoid saturation broadening.

The smallest observed full-width-half-maximum linewidths are $\simeq$ 3.0 MHz. Assigning this to be due to Doppler broadening only, the value yields an upper limit of 15 mK for the secular temperature, consistent with the MD simulations.

The observable spectrum may be modeled, including the effects of finite secular temperature, finite laser linewidth, finite population in the lower level, the effect of unresolved Zeeman splittings by the non-zero magnetic field in the ions' region [12], and black-body-radiation induced excitation to (0, 1). In order to simplify the analysis, in the experiment we chose laser power and irradiation times such that significant saturation and concomitant broadening of the signals was avoided, i.e. the linear absorption regime was maintained. We furthermore take into account: (i) from independent measurements we have some knowledge about the magnetic field: an upper limit of ca. 1 G [4]; (ii) the laser linewidth does not contribute strongly to the total linewidth, and we may therefore use an effective Doppler temperature for modeling the lineshape; (iii) the overlap between the focused spectroscopy beam (ca. 0.5 mm waist) and the ion cloud was not constant over the time span covering all hyperfine line measurements; (iv) the effect of black-body-induced excitation (0, 0) $\rightarrow$ (0, 1) represents a reduction in maximum observable signal. Thus, we fit an effective product of intensity and irradiation time to each transition spectrum in order to reproduce the signal levels. We used a simplified model of the magnetic field inhomogeneity in the ions' volume. We find a good fit for an average magnetic field of 0.8 G and (9.5 ± 1) mK temperature. The statistical error for the spinless frequency $f_{0,th}$ is obtained from a Monte Carlo simulation as 60 kHz.

4. Systematic errors

Due to the slow data rate of this experiment, measurements of systematics were not possible. However, the well-developed theory of the HD^+ molecule allows relying on theoretical results to estimate upper limits for various systematic errors. Those due to light shift, black-body shift [6], electric quadrupole shift [7], and Stark shift [8, 9], are theoretically estimated to be less than 10 kHz. The only potential significant effect is the Zeeman effect. The sticks in Fig. 3, 4 show the splittings expected for the typical magnetic field value in our trap [12]. These unresolved splittings could lead to a shift of the centers of the lines but we find that the weighted mean frequency of the magnetic components of any line shifts weakly with magnetic field (e.g. less than ca. 10 kHz for line S0 at 1 G). We

modeled the influence of the imprecisely known magnetic field on the fitted spin-independent frequency and estimate an error of 13 kHz from this effect. In order to obtain the spin-independent frequency from our measurements, we use the theoretical prediction of the hyperfine energies. The influence of their theoretical errors onto the fitted spin-independent frequency is conservatively assumed to be 10 kHz. The error of the optical frequency measurements is less than 10 kHz. Similar considerations are applied to the fit of the hyperfine splittings.

5. Theoretical transition frequencies

The theoretical frequency of any particular hyperfine transition arises from three contributions. The main contribution is non-relativistic, 58 604 301.269 MHz, determined by the solution of the Schrödinger equation [21] and whose error (11 kHz) comes dominantly from the uncertainties of the electron-proton and proton-deuteron mass ratios m_e/m_p, and m_p/m_d [5]. A second contribution, 750.870 MHz, is from relativistic and QED effects [22], with estimated theoretical uncertainty of 21 kHz [19]. The sum of these two contributions is the spin-independent frequency $f_{0,th}$. The third is the hyperfine contribution [11], e.g. -38.685 MHz for transition S0. Improved values for the hyperfine constants and Bethe logarithm communicated recently by V. Korobov have been used here. The influence of these improved values as compared to the published ones on the results presented here is small in comparison with the experimental uncertainties. The theoretical uncertainty of the hyperfine contributions to the transition frequencies is less than 10 kHz [19].

6. Hyperfine state preparation

The re-pumping suggested acts predominantly on the strong, non-spin-state changing transitions. P2 is a weak transition, P3, P4 are very weak transitions. The transition dipole moments of the latter are so small [12] that a quantum cascade laser (typical output power level 10 mW) could be used for obtaining usefully large rates. Such a laser could be frequency-stabilized to a spectrometer of the type developed here, using the beat note with it as an error signal.

An additional rotational cooling laser that depletes the ($v = 0$, $L = 3$) level by exciting from it to the (1, 2) or (2, 2) level could enable an even higher population fraction in the goal hyperfine state.

In a similar way, any other Zeeman states of the ground vibrational level could in principle be populated to a high fraction.

It is recognized that variations of the above scheme can also be used to achieve similar population fractions in individual quantum states of the ($v = 0$, $N = 1$) level.

[1] Wavelengths shorter than 4.4 µm were obtained in: P. Cancio, S. Bartalini, S. Borri, I. Galli, G. Gagliardi, G. Giusfredi, P. Maddaloni, P. Malara, D. Mazzotti and P. De Natale, Appl. Phys. B **102**, 255 (2011)

[2] For wavelengths near 10.6 µm, see A. Amy-Klein, A. Goncharov, M. Guinet, C. Daussy, O. Lopez, A. Shelkovnikov, and C. Chardonnet, "Absolute frequency measurement of a SF_6 two-photon line by use of a femtosecond optical comb and sum-frequency generation", Opt. Lett. **30**, 3320 (2005)

[3] C. B. Zhang, D. Offenberg, B. Roth, M. A. Wilson, and S. Schiller, Phys. Rev. A **76**, 012719 (2007)

[4] J. Shen, A. Borodin, M. Hansen, and S. Schiller, subm. to Phys. Rev. A. (2011)

[5] P.J. Mohr, B.N. Taylor, and D.B. Newell (2011), "The 2010 CODATA Recommended Values of the Fundamental Physical Constants" (Web Version 6.0). This database was developed by J. Baker, M. Douma, and S. Kotochigova. Available: http://physics.nist.gov/constants. National Institute of Standards and Technology, Gaithersburg, MD 20899

[6] J.-Ph. Karr, S. Kilic, and L. Hilico, J. Phys. B **38**, 853 (2005);

[7] A. K. Bhatia and R. J. Drachman, Phys. Rev. A. **61**, 032503 (2000);

[8] R. E. Moss and L. Valenzano, Mol. Phys. **100**, 1527 (2002)

[9] D. Bakalov and S. Schiller, to appear in Hyperfine Interactions (2012)

11 Acknowledgement

This work and its successful completion would not have been possible without the contribution of our highly motivated team.

I hereby express my sincere thanks to

Prof. S. Schiller for giving me the possibility to research this very interesting and challenging topic with the opportunity for my colleagues and I to work independently, the scientific cooperation in achieving results and encouraging us for best performance, in what has been proved as a successful concept,

Prof. K. Schierbaum for his cooperativeness as reviewer,

my colleagues Andrii Borodin, Ingo Ernsting, Michael Hansen and Jian Wei Shen,
Ingo for his contributions in the stabilization of the laser diode and for all the time he has spent in working with the frequency comb, before and during our various measurements,
Michael for supporting us so much in taking data in our measurement runs,
Andrii, Jian Wei and Ingo for their participation in our long measurement nights,

A. Yu. Nevsky and our former institute members C. Eisele, J. Koelemeij, D. Offenberg, B. Roth, T. Schneider and S. Vasilyev for their constructive discussions during the initial phase of the project,

P. Dutkiewicz and R. Gusek for their electronic components, e. g. for locking the resonator,
D. Iwaschko and H. Hoffmann in producing various devices and parts,
U. Rosowski for his assistance in the room temperature stabilization measures,

Prof. W. Behmenburg for his friendship and continuous interest in our work

and Akobuije Chijioke for his willingness to proofread.

Erklärung

Die hier vorgelegte Dissertation habe ich eigenständig und ohne unerlaubte Hilfe erstellt. Die Dissertation wurde weder in der vorgelegten Version noch in ähnlicher Form bei einer anderen Institution eingereicht. Ich habe keine erfolglosen Promotionsversuche unternommen.

Düsseldorf, den 16.12.2011

(Ulf Bressel)